First photon detection in transillumination imaging: a theoretical evaluation

Setayesh Behin-Ain

This thesis is submitted as part of Doctor of Philosophy to the

Department of Physics and Mathematical Physics,
University of Adelaide

Supervisors:

Tim van Doorn and John R. Patterson

Adelaide, February, 2003

Contents

Abstract

This thesis is a theoretical evaluation of the (single) first photon detection (FPD) technique as a limiting case of time-resolved transillumination imaging (TI) for diagnostic purposes. It combines analytic and Monte Carlo (MC) simulation methods to derive the single photon statistics and to solve the radiative transfer equation (RTE) for a given source-medium-detector geometry.

Initially, a standard Monte Carlo (SMC) simulation algorithm for visible to infrared photon transport through a turbid (randomly scattering and absorbing) medium such as soft tissue is developed from first principles. This provides a time dependent solution of the RTE at longer time scales. In order to efficiently simulate very early arriving photons, an Indeterministic Monte Carlo (IMC) technique based on path integrals is devised and validated. The IMC utilises the SMC algorithm to propagate photon trajectories and extends controlled MC techniques to accelerate and enhance the probability of detecting shorter trajectories thereby improving the statistics.

The IMC technique provides a tool for the construction of a temporal point spread function (TPSF) of the emerging photons for the entire time scale. The computational procedure is validated by reproducing the published spatial resolution results associated with conventional time-gated systems over longer time scales of several hundred picoseconds. It is then used to predict the spatial resolution of these systems for shorter (sub-100 picosecond) time scales.

The calculation of the TPSF at short time scales for a pulse made incident onto the medium enables the mathematical derivation of the temporal probability density functions (p.d.f.) for the first arriving photon, $f_1(t)$. This facilitates the investigation of a *first* photon detection (FPD) system as applied to a diagnostic TI configuration.

A FPD system produces a signal representing $f_1(t)$ from which the mean transit time of the first arriving photon, $\bar{t_1}$, may then be estimated for a sequence of incident pulses at each scan position. By rectilinear scanning across the medium, a 2-D map of $\bar{t_1}$ can be created and displayed as a grey scale image.

The application of FPD to TI is evaluated assuming an ideal detector capable of detecting the first arriving photon with 100% efficiency (infinite extinction coefficient). However, a model for a FPD system corresponding to a non-ideal (single first photon) detector is also considered through the evaluation of the p.d.f. for the later (1^{st}, 2^{nd}, $\cdots$) arriving photons. This enables a detection time limit to be specified to eliminate the later arriving photons and thereby overcome distortions in the first photon p.d.f. which may be caused by any inefficiency in the response of the detector.

The FPD technique is then applied to obtain $f_1(t)$ for various laser pulse intensities. The FPD system is also examined for the case of spherical inhomogeneities (representing tumours) embedded in the centre of an otherwise homogeneous medium. The effect of the variations in the embedded inhomogeneity (size and optical density) and optical properties of the medium are also studied. A heterogeneous medium which resembles tissue more realistically is considered.

For a FPD system where the received signal does not change (one photon) per incident pulse, the signal contrast is redefined and is examined as a function of the incident laser power and medium absorption and scattering properties. The signal-noise-ratio is also evaluated for the FPD system as the error in the estimation of $\bar{t_1}$. Based on the analysis of the SNR, the number of incident pulses (per scan position), needed to achieve a required SNR, is also derived.

It is shown that the p.d.f. of the first arriving photon for a $\sim 3mm$ totally absorbing inhomogeneity located at the mid-plane of a $50mm$ thick tissue-like medium may be distinguished (95% confidence level) from the p.d.f. of a medium without the inhomogeneity. This theoretical study provides an introduction aimed at assisting further experimental research into the limits of transillumination imaging employing a first photon detection (FPD) system.

Declaration

This thesis does not contain work which has been accepted for any other award in any university. Nor does it contain work which has previously appeared elsewhere, except where referenced within the text. It is available to be photocopied and lent from the University Library.

Setayesh Behin-Ain

February, 2002

Acknowledgements

First and foremost, I acknowledge my supervisors, Tim van Doorn and John R. Patterson. Their guidance, support, encouragement and dedication have been remarkable. I would also like to specially thank them for their understanding of not only the academic, but also personal aspect of my path to this point.

Members of the Medical Physics department at the Royal Adelaide Hospital have been most supportive and helpful. Special thanks to Eva Bezak and Sergei Zavgorodni for their valuable suggestions and guidance. Christine Robinson has been most helpful and patient.

Many thanks go to Dr. Leighton Barnden of The Queen Elizabeth Hospital for his continued support and patience.

Members of the optics group, and in particular Shahraam, Shu Yen, Alex, Blair and Aidan are acknowledged. Peter, Jennifer, Fanel, Alina, Don, David, Loredana, Bob, Trevor, Irene, Carmel and Arlene of the Physics department are acknowledged for their support throughout. Dr. Rod Crewther is specially thanked for his support at various stages. The Centre for Subatomic Structure of Matter (CSSM) is acknowledged for the provision of computing resources.

I would also like to thank Mr. Nosrati of Adl High School, Esfahan, and Mr Rights of Chester Hill High School. They created two of the most enjoyable moments in my academic path to here.

Armin Ardekani is specially noted. His qualities as an outstanding friend have been most critical during my PhD. from both the academic and personal perspectives. Alireza Kazempour and his family have been most supportive, thank you for your care, encouragement and advice. Behyar Behin-Aien's support and encouragement is always remembered.

Kamran Behin-Aien's dedication and support for my family and myself has been phenomenal. Without him, this point may not have been reached. Zohreh, Abbas, Niloufar and Forough have also had their share.

List of abbreviations and symbols

TI	Transillumination imaging
FPD	First photon detection
TOF	Time of flight
NIR	Near infrared
CW	Continuous wave
RTE	Radiative transfer equation
MC	Monte Carlo
SMC	Standard Monte Carlo
IMC	Indeterministic Monte Carlo
CMC	Controlled Monte Carlo
TPSF	Temporal point spread function
FWHM	Full width half maximum
PSF	Point spread function
ERF	Edge response function
MTF	Modulation transfer function
LSF	Line spread function
RW	Random walk
FTL	Flight time limit
Δt	Gating time
Δx	Spatial resolution
W	Photon weight
I	Intensity
μ_a	Absorption coefficient
μ_s	Scattering coefficient
μ_t	Total attenuation coefficient
μ_s'	Transport (reduced) scattering coefficient
$\bar{\mu_s}$	mean (effective) scattering coefficient
λ	Wavelength
θ & ϕ	Zenith & azimuthal scattering angles
$f(\cos\theta)$	Scattering phase function
g	Mean cosine of scatter
l	Scattering mean free path
l'	Transport length
c	Velocity of light
E_g	Detector extinction coefficient
ε & κ	Transmission factors of the optical gate
t_1	First photon arrival time
$\bar{t_1}$	First photon mean arrival time
p.d.f.	probability density function
c.d.f.	cumulative (probability) distribution function
$f(t)$	temporal p.d.f.
$F(t)$	temporal c.d.f.
$f_1(t)$	First arriving photon temporal p.d.f.
$F_1(t)$	First arriving photon temporal c.d.f.

List of Figures

List of Tables

Author's publications and presentations related to the work of this:

Refereed journal publications:

- S. Behin-Ain, T. van Doorn, J. R. Patterson, "An Indeterministic Monte Carlo (IMC) technique for fast time of flight photon transport through optically thick turbid media," Med. Phys., **29,** 125-131 (2002).

- S. Behin-Ain, T. van Doorn, J. R. Patterson, "Spatial resolution in fast time-resolved transillumination imaging: an indeterministic Monte Carlo approach," Phys. Med. Biol., **47,** 2935-2945. (2002).

- S. Behin-Ain, T. van Doorn, J. R. Patterson, "First photon detection in time-resolved transillumination imaging: a theoretical evaluation," Appl. Opt., (Submitted for publication).

Published conference presentations:

- S. Behin-Ain, T. van Doorn, J. R. Patterson, "Evaluation of the limiting resolution in time resolved transillumination (TRTI) imaging", *ESTRO conference, Seville*, Radiotherapy and Oncology, **61,** 113 (2001).

Unpublished conference presentations:

- S. Behin-Ain, T. van Doorn, J. R. Patterson, "Single photon detection in time-gated diagnostic transillumination imaging,"*Engineering and Physical Sciences in Medicine (EPSM) conference proceedings* p 113, Rotorua, New Zealand, 2002.

- S. Behin-Ain, T. van Doorn, J. R. Patterson, "Spatial resolution limit in time-gated transillumination imaging (TGTI) in turbid media," *Engineering and Physical Sciences in Medicine (EPSM) conference proceedings* p 72, Fremantle, Australia, 2001.

- S. Behin-Ain, T. van Doorn, J. R. Patterson, "Early tumour detection: a transillumination, time-resolved technique," *Engineering and Physical Sciences in Medicine (EPSM) conference proceedings* p 131, Newcastle, Australia, 2000.

سەرپووڵ دڵییم

To my parents

Chapter 1

Introduction

1.1 History and motivation

Tissue transillumination was used in the mid 1800s by British physicians to detect lesions in tissue before Cutler [1] postulated the use of visible light as an imaging tool to locate breast lesions in 1929. This motivated further investigation into transillumination[1] imaging (TI) as a clinical technique based on the propagation of light through a turbid (randomly scattering and absorbing) medium such as soft tissue. The technique did not attract much attention initially as an imaging modality, due largely to the success of x-rays, as well as to the lack of suitable illuminating sources and efficient detectors.

The extension of optical monitoring of intact tissues from the visible to the near-infrared (NIR) wavelengths range (700-1300nm) was first reported in 1977 for the purpose of *in vivo* monitoring of cerebral and myocardial oxygen sufficiency [2]. In normally hydrated tissues, water absorbs all photons with wavelengths of above 1300nm, over a path-length of less than a few millimetres. In the visible part of the spectrum, below 700nm, the intense absorption bands of hemoglobin (Hb) and the increasing light scattering phenomena again prevent transmission over long path-lengths. However in the 700 to 1300nm range of the IR, a significant amount of radiation can be transmitted through biological tissue over long distances. It became evident [2] that

[1] Transillumination imaging is also referred to as diaphanography in the literature.

the much greater NIR translucency of skin and bone made it possible to reach brain and muscle tissue without surgical intervention.

Interest in NIR breast imaging has been driven by certain recognized shortcomings in x-ray mammography. While x-ray mammography can provide high spatial resolution ($\sim 100\mu m$) and has an 85-90% detection rate of breast cancer (high sensitivity), it has low positive predictive value resulting in a high percentage of negative biopsies (low specificity) [3]. While ultrasound has helped to reduce the biopsy rate by providing a diagnostic way of distinguishing cysts from solid tumours [4], there still is difficulty in determining tumour grade and metabolic state. Some tumours are indistinguishable from healthy tissue using x-rays as the differential absorption (and scatter) is low for x-ray photon energies. It has also been estimated that x-rays in mammography cause 0.2% of breast cancers [5]. On the other hand, TI is non-invasive and has the potential to detect and distinguish tumours based on haemoglobin concentration and oxygen saturation changes as well as changes in the scattering and absorption properties [6]. A high differential variation of absorption and scattering coefficients of light in the NIR region enables visualisation of diffused tumours which are otherwise transparent to x-rays. Concerns about the effects of ionizing radiations, the need for frequent screenings and increased reliability (sensitivity) of diagnosis have motivated scientists to pursue research in TI more seriously in recent years.

Screening demands a spatial resolution of a few millimetres in order that tumours can be distinguished from the surrounding healthy tissue while they are still small in size before metastasis occurs. A $1mm^3$ breast tumour contains $\sim 10^6$ cells with a doubling time of 120-150 days. It is therefore evident that, at this growth rate, early detection of cancerous lesions increases the probability of cure. Screening mammography has decreased the mortality rate from breast cancer by approximately 30% as a result of diagnosis at an early stage. Although, it may not be a realistic goal to achieve the high spatial resolution of x-ray mammography, millimetre spatial resolution, using TI, would help the early diagnosis of tumours of low x-ray contrast. It is therefore hoped that TI would complement current mammography and supplement it in terms of the range of patient ages eligible for screening programs.

1.2 Optical characterisation of human breast tissue

A mature female breast is composed of essentially four structures: lobules or mammary glands, milk ducts, fat and connective tissue. The lobules group together into larger units called lobes. On average there are 15-20 lobes in each breast and their distribution is not even. The glandular structure of the breast is only significant during late pregnancy and when a woman is nursing. At other times the glandular and duct system is undeveloped and the bulk of the breast mass is attributed to the deposition of fatty adipose tissue, with a water/lipid ratio of 21/74% [7].

The breast tissue includes chromophores; oxyhaemoglobin(HbO_2), deoxyhemoglobin (Hb), cytochromes and pigments. In the NIR spectra, absorption is principally caused by the chromophores, oxy- and deoxyhemoglobin, and water [8, 9] whereas scattering originates from fluctuations (inhomogeneities) in the refractive index of connective tissues (extracellular) and cell constituents (membranes, cell organelle and nucleus).

Within the photon energy range of visible to NIR (700-1300nm), absorption is ascribed either to electronic or vibrational excitations. NIR absorption bands are associated with transitions between molecular vibrational modes, in particular overtone and combination bands of hydrogenic stretching and bending vibrations in C-H, N-H and O-H bonds, with hydroxyl absorption bands of water predominating. The probability of absorption is greatly exceeded by scattering.

Human tissue is a highly complex structure composed of tightly packed groups of cells entrapped in a network of fibres through which water percolates. Viewed on a microscopic scale, the constituents of tissue have no clear boundaries. They appear to merge into a continuous structure distinguished optically only by spatial variations in the refractive index. To model such a complicated structure as a collection of particles, it is necessary to resort to a statistical approach. Hence, for modelling purposes soft tissue is treated as homogeneous with at most a clearly defined layer structure.

In the radiative transfer description of transillumination imaging, light propagation in turbid media may be characterised by the refractive index n, linear absorption, scattering and total attenuation coefficients μ_a, μ_s and $\mu_t(=\mu_a+\mu_s)$, and the function

$p(\theta) = f(\cos\theta)\sin\theta$ which describes the distribution of the scattering angle θ. $f(\cos\theta)$ is referred to as the scattering phase function. μ_a and μ_s describe the total probability per unit path length of a photon being absorbed or scattered, respectively. Other useful parameters are the anisotropy g, the mean cosine of the scattering angle determined by $f(\cos\theta)$, the *transport* (or *reduced*) scattering coefficient $\mu_s' = \mu_s(1-g)$ and scattering mean free paths, $l_s = 1/\mu_s$. A value of g close to 1, 0 or -1 represents strongly forward, isotropic and strongly backward scattering respectively. The *transport length* $l' = 1/\mu_s'$ is the distance over which the trajectory loses memory of its original directionality [10]. The effective attenuation coefficient $\mu_{eff} = \sqrt{3\mu_a(\mu_a + \mu_s')}$, in the first approximation, represents the rate of the exponential drop in the intensity, $(e^{-\mu_{eff}\, r})$, far away from the source. Finally, for simplicity in the nomenclature, the speed of light in the medium is denoted by c which is speed of light in vacuum divided by the refractive index.

Various forms for the phase function have been suggested [11, 12, 13]. However, according to the similarity principle [14], turbid media that have different phase functions but the same value of the anisotropy g and the single scattering albedo $\omega = \mu_s/\mu_t$, have approximately the same radiative characteristics. Therefore, for the purpose of this thesis, the widely accepted Henyey-Greenstein's phase function [12, 14] is used.

The optical response of tissue generally varies with the illuminating wavelength. Methods to determine the optical parameters of human tissue both *in vivo* and *in vitro* have been extensively reported[7,8,9,13,15-34]. A report by Wai-Fung *et al* [24] provides a summary of these methods. The optical properties are commonly evaluated by fitting a theoretical solution of a radiative transfer model to the shape of the characteristic function curves[2]. Therefore, the accuracy of the measurement depends on how well the solution of the theoretical model describes the experimental setup. For example, using the diffusion model and based on a curve fit to the temporal point spread (temporal characteristic) function (TPSF), Ntziachristosa [15] demonstrated that the error in measurement of μ_a and μ_s' varied depending on whether a fit to the whole or only the

[2]For an homogeneous sphere of radius r, Mie theory predicts the wavelength dependence of the scattering and the relation between scattering and sphere size [35]. However, since the exact composition of tissue is often unknown due to variations, the method of curve fitting to TPSF using diffusion theory is more convenient.

later part of the TPSF was used. More accurate results were obtained when only the later part of the TPSF was used. As will be discussed, this is due to the fact that the diffusion model does not provide an accurate description of the radiative transport in the early part of the TPSF.

A great variation in the values of the optical parameters of breast tissue has been observed. This may be attributed to a number of factors, for example blood glucose concentration [36], menstruation [7], measurement techniques (e.g., *in vitro* or *in vivo*) and variations between test subjects (e.g. age). Furthermore, measurements *in vivo* usually sample both adipose and glandular tissue making their interpretation complicated. *Ex vivo* measurements can be made on specific tissues but the optical properties may be different due to sample handling and blood loss. Table 1.1 includes some of the reported values for μ_a, μ_s' and g for various laser wavelengths. In a breast tumour the absorption generally increases which is often due to an increased concentration of oxy-haemoglobin. Lower μ_s' is expected for fluid-filled structures (i.e., fluid-filled cysts), and increased scattering should occur in the case of fibrotic tissue (i.e., fibroadenoma). The scattering coefficient is 1.3-1.4 times higher for pre- compared to post-menopausal subjects [8]. This is attributed to the fact that pre-menopausal, highly glandular tissue has substantial structural complexity whereas postmenopausal breast is dominated by low water content adipose. Studies [37] show that the reduced scattering coefficient μ_s', decreases with increasing wavelength[3]. The refractive index of human tissue has been reported to be between 1.33-1.55 [38] and for breast tissue it is expected to be close to 1.45 [39, 40].

1.3 Radiative transfer equation (RTE)

Maxwell's equations of electromagnetism describe analytically, the wave theory of energy transfer. However, seeking a solution based on Maxwell's equations for a medium

[3]Torricelli *et al* [37] have found a linear relation: $\ln(\mu_s') = a\ln(\lambda) + b$ between the scattering coefficient μ_s' and the wavelength λ with $a \sim -(0.4\text{-}1.0)$ and $b \sim 2.3\text{-}3.0$ depending on the subjects and tissue type (abdomen, arm and head). This also implies greater penetrability of NIR and hence its suitability in TI.

Tissue type	$\lambda(nm)$	$\mu_a(mm^{-1})$	$\mu_s'(mm^{-1})(g)$	Reference
Breast(normal)	674	0.003-0.004	0.78-1.1	[8]
	753	0.0046±0.0014	0.89±0.13	[7]
	811	0.003-0.004	0.70-0.95	[8]
	956	0.008-0.010	0.65-0.95	[8]
Glandular	700	0.047 ± 0.011	1.42 ± 0.30	[27]
	900	0.062 ± 0.005	0.99 ± 0.2	[27]
	1100	0.06 ± 0.03	$0.8 \pm 0.25(0.96 \pm 0.02)$	[27]
Adipose	700	0.07 ± 0.008	0.86 ± 0.13	[27]
	900	0.075 ± 0.008	0.79 ± 0.11	[27]
	1100	0.1 ± 0.03	$0.65 \pm 0.25(0.98 \pm 0.02)$	[27]
Fat	700	-	0.8-1.8	[9]
	700	0.004±0.001	0.53±0.11	[28]
Fibroglandular	700	-	0.7-1.7	[9]
	700	0.0045±0.0021	0.90±0.20	[28]
Breast(tumour-Fibrodenoma)	674	0.005-0.007	0.75-0.9	[8]
	811	0.005-0.007	0.70-0.8	[8]
	956	0.012-0.016	0.70-0.75	[8]
	700	0.052 ± 0.047	0.72 ± 0.17	[27]
	900	0.072 ± 0.053	0.53 ± 0.14	[27]
	1100	0.06 ± 0.03	$0.4 \pm 0.15(0.98 \pm 0.01)$	[27]
Breast(tumour-Fibrocystic)	700	0.022 ± 0.009	1.34 ± 0.19	[27]
	900	0.027 ± 0.011	0.95 ± 0.17	[27]
	1100	0.05 ± 0.03	$0.73 \pm 0.3(0.98 \pm 0.01)$	[27]
Breast(tumour-Carcinoma)	700	0.045 ± 0.012	1.18 ± 0.31	[27]
	700	-	1.8 ± 0.5	[9]
	1100	0.05 ± 0.02	$0.72 \pm 0.15(0.95 \pm 0.01)$	[27]
Dermis	633	0.033-0.241	2.73-3.21	[25, 20]
(Caucasian)	633	0.27	3.55(0.81)	[26]
	700	0.019-0.149	2.32-2.68	[20]
	900	0.013-0.045	1.63-1.18	[20]
	1000	0.018±0.001	1.1±0.1(0.85-0.95)	[20]
Muscle	633	0.121	0.89	[20]
	690-800	0.085 ± 0.01	-	[41]
	700	0.046	0.83	[20]
	900	0.032	0.59	[20]
Brain(white matter)	633	0.16	0.20(0.96)	[29]
Brain(grey matter)	633	0.26	0.7(0.88)	[29]
Brain(tumour-glioma)	630	0.5	0.70	[30]
Brain(tumour-melanoma)	630	-	0.80	[30]
Whole blood	665	0.130	0.611(0.995)	[31]
	685	0.265	1.413(0.99)	[42]
	960	0.284	0.384(0.92)	[31]

Table 1.1: Optical properties of human breast tissue. Optical properties of other soft tissues (muscle, brain and blood) have also been presented for comparison.

such as human tissue is a cumbersome task. This is due to the highly complex structures involved and a lack of knowledge of the dielectric properties of their components. Most theoretical models are therefore based on the particle interpretation of light. The magnitude of the photon density in a specified direction is then assumed to be proportional to the scalar field I, the energy radiance. This leads to the radiative transfer model in which the equations are much simpler [12, 43]. At visible and NIR energies, photon interactions can be considered elastic and where wave properties of the light can be neglected, radiative transfer theory provides an accurate description of most observable effects.

When the electromagnetic wave properties (e.g. polarization) and inelastic collisions (change in the photon frequency) are ignored, the time-dependent radiative transfer equation (RTE) is the most widely used transport equation in time-resolved TI. This equation describes the behaviour of the specific intensity $I(\mathbf{r}, t, \hat{s})$, i.e., the energy, moving in the direction $\hat{s}$, per unit solid angle, per unit time, and per unit area normal to the $\hat{s}$ direction, with units Wm^{-2}. The RTE can be obtained by considering the total space and time variation of the specific intensity along a direction $\hat{s}$ in an elementary volume and making this equal to the variation of specific intensity due to scattering and absorption inside the medium. The RTE is then given as [12, 44]:

$$\begin{aligned} \frac{1}{c}\frac{\partial I(\mathbf{r}, t, \hat{s})}{\partial t} &= \hat{s}.\nabla I(\mathbf{r}, t, \hat{s}) - \mu_t I(\mathbf{r}, t, \hat{s}) + \\ &\quad \mu_s \int_{4\pi} f(\hat{s}, \hat{s}') I(\mathbf{r}, t, \hat{s}) d^2\hat{s}' + q(\mathbf{r}, t, \hat{s}), \end{aligned} \tag{1.1}$$

The LHS of Eqn. 1.1 describes the variation in the intensity I w.r.t. time. The terms on the RHS relate the four contributions to the change in intensity: (1) change due to intensity gradients, (2) decrease due to absorption or scatter, (3) contribution from other scatterers and (4) presence of a source. The phase function $f(\hat{s}, \hat{s}')$ describes the distribution of the scattering angle in the direction of $\hat{s}'$ with respect to the propagation direction $\hat{s}$ as described before.

1.4 Solution of RTE

The RTE in its general time dependent and three dimensional form has not been solved either analytically or numerically. The dependence of the RTE on several variables (seven in general) and the existence of the integral term, suggest two pathways in solving this equation: (1) use of approximations in an effort to allow its application to the study of realistic problems and (2) the solving of a restricted form of the RTE directly by numerical or statistical techniques. Approximations may be:

Geometric:

- Isotropic, homogeneous media,
- Infinite or semi-infinite geometries,
- One-dimensional symmetry (plane, spherical or cylindrical),
- Periodic symmetry (Lattices).

Energy dependence[4]:

- One-speed approximations in which all photons are characterized by a single kinetic energy,
- Simple models of the energy dependent cross section.

Angular:

- Isotropic source,
- Isotropic scattering,
- Expansion of the collision kernel[5] in a finite set of Legendre polynomials in angle.

In the following sub-sections some of the theoretical techniques which are commonly employed to solve the RTE are introduced. The list is by no means comprehensive and a more extensive review has been given by Arridge and Hebden [45]. Because of the very short times of flight under investigation, these techniques generally suffer from one or more of the following drawbacks: (1) complexity of calculation (e.g. to obtain an exact 3-D analytical solution of RTE), (2) accuracy and/or limitations in

[4]Note that since the energy dependence was already eliminated in Eqn. 1.1 this listed only for completion here.

[5]The collision kernel is a generalised form of the phase function which is also a function of the photon velocity as well as the scattering angle.

temporal or spatial boundary condition when approximations are applied and (3) they are computationally intensive. However, the Monte Carlo simulation technique proved flexible and accurate when it was made less computationally intensive by introducing a new variance reduction technique.

1.4.1 Analytic Models

The RTE is a deterministic equation and simpler deterministic models can be derived from it. The principle of expanding the intensity, I, source, q, and phase function, $f(\cos\theta)$, in spherical harmonics and retaining only a limited number of terms is well established [46, 47]. A recent approach by Cai *et al* [48, 49] using a cumulant expansion provides an exact solution, to an arbitrary order for an infinite medium. Further work such as that of Arridge *et al* [50], Moon *et al* [51] and Joblin [52] is needed to explore the applications of this solution to a finite medium. One of the best summaries on the analytic solutions has been provided by Kaltenbach and Kaschke [53] who derive a hierarchy of equations, of which the simplest is the time-dependent diffusion equation.

Diffusion Approximation

By assuming that the radiation flux[6] has a weak angular dependence and also that the time variation in the current density[7] is much smaller than the collision frequency [12, 54], the integro-differential RTE is converted to a partial differential equation (PDE);

$$\frac{1}{c}\frac{\partial I(\mathbf{r},t)}{\partial t} = -D\nabla^2 I(\mathbf{r},t,\hat{s}) + q(\mathbf{r},t,\hat{s}), \tag{1.2}$$

where the diffusion coefficient D is defined as:

$$D = [3(\mu_a + \mu_s')]^{-1}. \tag{1.3}$$

The pulsed sources used in optical imaging are usually sufficiently close approximations to δ-functions to make the Green function an appropriate solution of the diffusion

[6]Flux is defined as the magnitude of the photon density perpendicular to an element of area.

[7]The photon density per unit cross sectional area is referred to as current density.

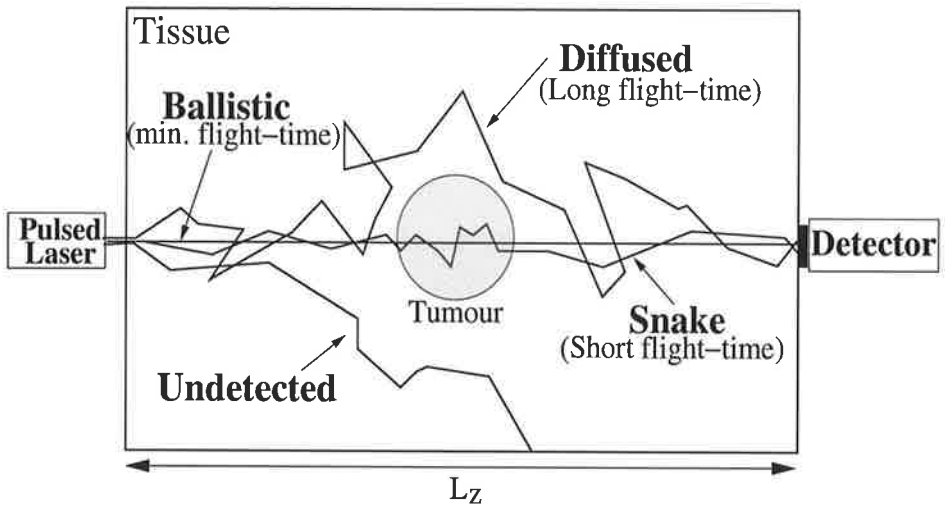

Figure 1.1: A schematic diagram of possible photon trajectories. Note that undetected trajectories also include both specular and diffused reflections from the front x-y incident surface.

equation (1.3). Green functions for various homogeneous geometries (slabs, cylinders and spheres) have been published, for both the temporal and frequency[8] domains [50, 55]. Eason *et al* [56] provide analytic forms with more complex source conditions including collimated and distributed sources. The analytic form for the Green function of a sphere embedded in an infinite scattering domain has also been derived [57, 58, 59].

The diffusion model presented by Eqn. 1.2, best describes the diffused portion of the transmitted pulse. However, it assumes the light photons are diffused with a constant diffusion coefficient [60]. This assumption is invalid in the case of snake photons (cf. Fig. 1.1 and section 1.5.2) that contribute to the early part of the transmitted pulse [48, 49]. To account for this, a common practice is to assume that all incident photons are initially scattered at a depth $z_0 = l'$ inside the medium which is called the centre-moved diffusion (CMD) model. But the CMD breaks the reciprocity principle[9] [14] and still fails to describe photon propagation for early times of flight [61, 62].

[8]The time dependent RTE may be converted to an equation in the frequency domain by means of Fourier transform.

[9]The reciprocity principle requires the invariance of the solution under interchanging the source and detector geometry.

Finite difference method

The finite-difference method (FDM) is a standard numerical technique for solving PDEs. A regular grid is established in the problem domain and differential operators are replaced by discrete differences. The problem then becomes one of sparse matrix algebra. The FDM can also solve the transport equation, provided that the angular integral over scattering directions is discretised. Hackbush [63] described a multigrid scheme for elliptic equations (frequency-domain diffusion equation) which has been applied to optical tomography [64]. An optimal alternative direction implicit scheme by Ames [65] was used by Natterer [?] to develop very efficient computation schemes. Joblin [52] used the FDM to derive the limiting spatial resolution as applied to time-resolved TI in the diffusion limit. Sun *et al* [67] have extended the FDM technique to simulate light scattering and absorption by non-spherical particles embedded in an absorbing dielectric media.

Finite element method

The finite-element method (FEM) is more versatile than the FDM, especially in regard to complex geometries and for modelling boundary effects [?]. By finding an approximate solution that lies in the vector space spanned by a finite number of basis functions, the forward problem is reduced to one of finite matrix algebra for which efficient techniques have been developed. A FEM for the transport equation is described by de Oliveira [69] with a discrete number of scattering directions (e.g. 12). Its application to the inverse problem was first introduced by Schweinger *et al* [70]. Fast methods for deriving measurement operators are described by Arridge [71].

1.4.2 Stochastic approach

Stochastic methods involve modelling individual photon interactions either explicitly (e.g. Monte Carlo), or implicitly by deriving the probability density functions for photon transitions (e.g. random walk or Markov random field).

Monte Carlo

In a standard Monte Carlo (SMC) simulation [54, 72, 73] the trajectories of individual photons are simulated as they undergo scattering and absorption events governed by local values of optical parameters. Photon paths are followed until they are absorbed (or they have negligible contribution) or until they escape through the surface, thus contributing to a measurement. Such a method offers great flexibility in modelling arbitrarily complex geometries and parameter distributions. However, for tissue thicknesses of several centimetres, typical photon paths include several hundred interactions, and many millions of photons need to be followed to obtain useful statistics for which a very lengthy computation times is required. Variance reduction Monte Carlo models such as controlled Monte Carlo(CMC) [74], semi-analytical [75] and condensed [76] Monte Carlo provide better statistics at short time scales.

Random Walk

Random walk (RW) theory describes the statistical behaviour of random walks in the 3D medium, constrained along the elements of a discrete lattice. Although working within a simple cubic lattice severely restricts the number of directions in which motion is possible, a powerful description of photon migration is achieved using a relatively simple mathematical analysis [77]. When motion in an homogeneous space occurs with each of the lattice directions having equal probability, RW theory can be considered to be equivalent to a finite-difference approximation of the diffusion equation. Expressions for the time-dependent transmittance through homogeneous scattering slabs have been derived by Gandjbakhche *et al* [78]. Their work has also provided an analytical description of the spatial distribution of photons in the medium. A simple model for the dependency of spatial resolution on photon flight-time has also been developed by Gandjbakhche *et al* [79].

Path Integral

This method of solving stochastic problems is based on Feynman's path integral formalism [80]. An application of path integrals to particle transport in turbid media was

first demonstrated by Feynman himself. More recently Perelman *et al* [81] have used path integrals and the Lagrangian formalism to explore their application to TI. The path integral formalism states that the probability of occurrence of a photon trajectory is governed by the action (hence the Lagrangian) evaluated along that path. As such *any* path is probable. However, the classical path (which results in a minimum action) becomes dominant with other paths deviating from this path but constrained by the temporal and spatial boundary conditions. The path integral approach is therefore attractive when the distribution of photon trajectories is of interest [82].

Markov random field method

Grünbaum and Zubelli, and also others [83, 84] have developed a very different and general stochastic model based on transition probabilities. Given the exact value of the probabilities and the boundaries and for an ideal noiseless system, the model can recover the internal transition probabilities in the time-independent case. The method has not been applied to real systems because of the difficulty in relating the essentially topologically invariant analysis to real conditions.

1.5 Transillumination imaging techniques

Transillumination imaging aims to determine the optical response of the medium based on absorption, scattering and polarization effects. A transillumination image is a two dimensional map of a measurable characteristic of the transmitted intensity through a turbid medium. The recorded distribution may then be used to infer the optical properties of the medium. Imaging techniques are generally classified as *direct* and *indirect* [44, 85]. In a direct imaging technique the measured quantity, e.g., the transmitted intensity, is directly translated into a pixel value which forms a projection (two dimensional) image. This method assumes a one-to-one and direct, although not necessarily perfect, correlation between the measurement and the information along the detector line-of-sight. In the case of indirect imaging, a set of measurements of one or more temporal or frequency characteristics of the transmitted light, e.g., mean

flight time, is considered. This is followed by a reconstruction of the distribution of the scattering and absorption coefficients which would yield the set based on a model of radiative transport. Both direct and indirect imaging can be performed in either frequency or temporal domains. The mathematical equivalence of the temporal and frequency domain approaches is established through the Fourier transform of the radiative transport description.

1.5.1 Frequency domain techniques

In a frequency domain measurement, high frequency (100 MHz-10 GHz) intensity modulated laser beams illuminate the medium and create photon density waves within the medium. For each modulation frequency, the photon density wave characteristics are changed by propagation through the medium. The detector records the AC modulation amplitude and phase shift at each modulation frequency. A continuous wave (CW) light source can generally be utilised and hence measurements of this type involve less cost and are simpler to perform. A frequency domain measurement of photon transport in tissue was first reported by Lakowicz and Brendt [86]. The frequency domain technique has been applied in optical imaging (tomography) [6, 87, 88, 89], fluorescence imaging [90], haemoglobin imaging and tissue oxygenation [8, 91], measurements of optical properties of diseased and normal tissue [8, 92, 93], cancerous breast tumour diagnosis [94], human brain imaging [95] and IR photo-thermal dental imaging [96].

The resolution in the reconstruction of the TPSF in this technique depends on the range of modulation frequencies [97]. An observation of the phase shift for a single frequency enables the estimation of the first moment (mean flight time) on the TPSF. The limited availability of high frequencies has limited the temporal resolution to a few nanoseconds. Fishkin and Gratton [97] were able to study the spatial-resolving power of frequency domain methods. Their experimental measurements and Monte Carlo simulations were used to confirm that the spatial resolution improves with increased modulation frequency. The results also suggested that direct imaging would require frequencies of several GHz in order to achieve a spatial resolution substantially better than that obtained using simple CW intensity measurements.

1.5.2 Temporal domain (time-resolved) techniques

Recent developments in the production of ultra-short laser pulses and fast detectors have led to the advent of time-resolved TI which has high potential for use as a diagnostic tool in medicine [41, 45, 85].

A typical time-resolved (or gated) transillumination experiment as shown schematically in Fig. 1.2 consists of a source-medium-detector geometry with a pulsed laser beam made incident on the surface of a medium. As the pulse traverses the medium, both its macroscopic (e.g., temporal and spatial) and microscopic (e.g., directionality, coherence and polarisation) characteristics are convolved with the medium characteristic function. The detector then records measurements of the transmitted signal characteristics as a function of time. At each scan position, the number of photons passing through a detecting aperture as a function of time is described by a temporal point spread function (TPSF) as illustrated in Fig. 1.3. In this figure, the minimum flight time L_z/c marks the zero of the time scale where c is the speed of light in the medium. In a conventional integrating time-gated system, the integration time $\Delta t = [0, t_g]$ represents the time interval up to the closure of the detector. The application of temporal gating (integration over a gating window $[0, t_g]$) removes the long flight time photons which contain little or no useful information content with regard to the scatter/absorption characteristics of the medium in the direct path between the source and detector.

The transmitted photons can be classified into *ballistic* (coherent), *snake* (quasi straight forward) and *diffused* components. Although there is no clear distinction between the snake and the diffused component, analytic [48, 49] and experimental [62] results suggest that when the photon path length exceeds $\sim 10l'/c$ relative to the ballistic time (L_z/c), the diffusive regime may apply. Beer's law implies that the intensity of the coherent beam, i.e., number of ballistic photons travelling along the central axis without interacting, decreases exponentially with the thickness, L_z, of the medium. It is evident that for most medical applications in which the tissue thicknesses exceed a few tens of mean free paths, the probability of detection of ballistic photons rapidly drops to zero in practice. Due to large deviations from the detector line-of-

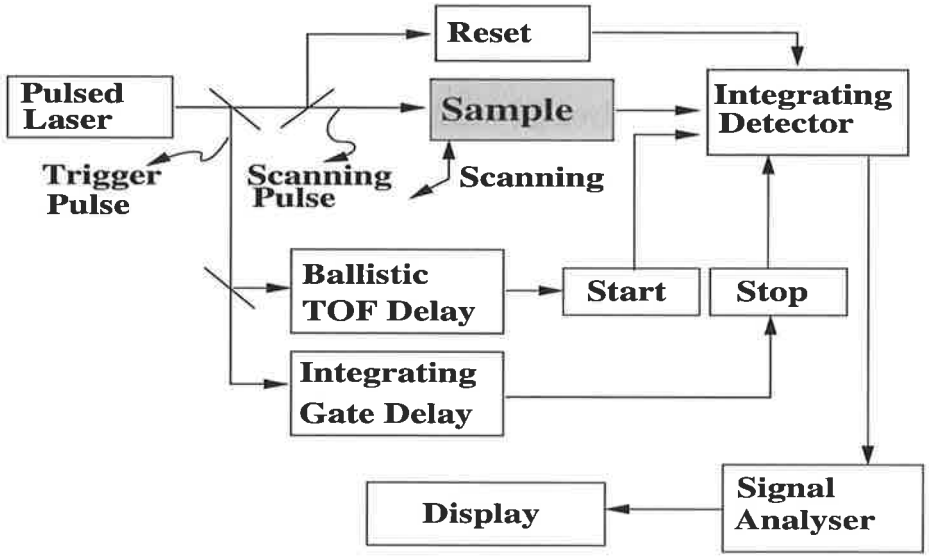

Figure 1.2: Schematic diagram for a conventional time-gated integrating system. The source-detector (propagation) direction coincides with the positive z direction. The beam scans the normal x-y plane and the sample (medium) thickness is L_z. The detector is triggered after a minimum ballistic time of L_z/c. The detector integrates the signal within the gating window as determined by the integrating gate delay.

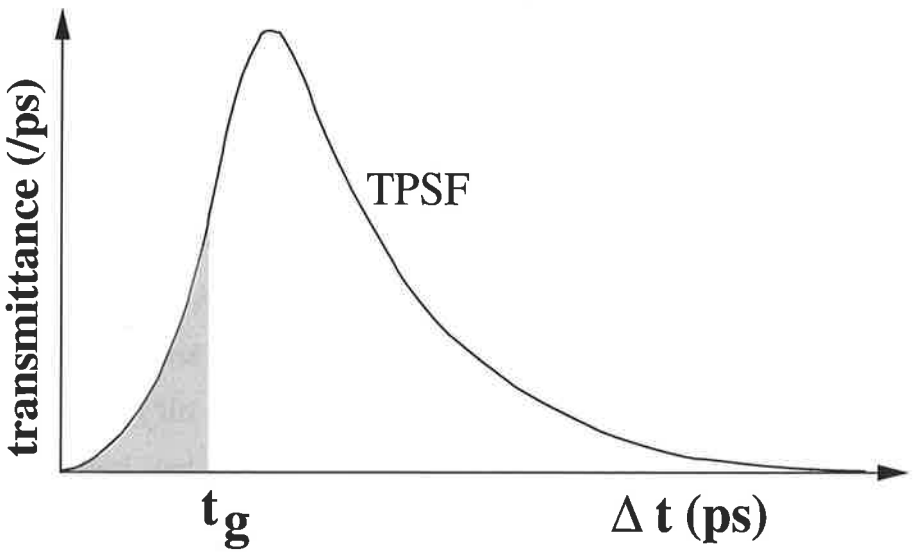

Figure 1.3: An illustration of the TPSF and the detector (gating) aperture $[0, t_g]$. The output from the integrating detector is the integrated intensity over $[0, t_g]$ as presented by the shaded region.

sight, the diffused component does not provide accurate information about the medium along this direction. On the other hand, snake photons which are least scattered provide inherently better spatial resolution and contrast since they propagate closest to the detector line-of-sight. Therefore, appropriate filtering, or *gating*, to isolate this component from the majority of the multiply scattered photons suggests itself as an efficient technique for achieving improved spatial resolution. Although this filtering can be obtained in either the temporal or frequency domain, current technological considerations make the temporal domain more attractive. Moreover, the performance of temporal domain direct imaging methods are relatively easy to quantify and predict.

A broad variety of gating techniques have been proposed and tested experimentally. The sub-nanosecond time scale required to isolate snake photons from the majority of light transmitted through thick turbid media eliminates the use mechanical shutters. Ultrafast gates include optical and electronic shutters such as the streak camera and time to analogue convertor (TAC) systems [98].

Martin *et al* [99] first reported the use of a fast optical shutter consisting of a Kerr cell [100]. A Kerr gate combined with a spatial filter was employed by Liang *et al* [101] to improve the spatial resolution. The performance of Kerr gate imaging techniques is ultimately limited by the dynamic range[10] of the transmission opacity of the cell, which is typically no better than 10^4. Thus, the shortest-flight-time (*snake*) photons cannot be sampled accurately as their number is much less than the total transmitted intensity.

The ideal time gate detector is one which can sample transmitted photons over any temporal window without contamination by photons arriving outside that window (i.e. it has an infinite extinction coefficient[11]). The streak camera is the device closest

[10]The dynamic range is the range of incident intensities over which the current output from the photodiode is linearly related to the input power. It is sometimes expressed as the ratio of the upper and lower limit over which the detector operates.

[11]The extinction coefficient (or transmission ratio), E_g, for a time-gated detection system is defined by $E_g = \frac{\kappa}{\varepsilon}$, where κ and ε are the transmission factors of the optical gating mechanism when in the open and closed states respectively. Ideally $\kappa \longrightarrow 1$ and $\varepsilon \longrightarrow 0$ which would correspond to zero rise time of the detector. E_g is a figure of merit for a time-resolved detection system; large E_g corresponds

to this ideal and is the most commonly used gating system in TI as it provides high temporal resolution ($\sim 10ps$) [102]. The first streak camera measurements of tissue were described by Delpy *et al* [103]. A streak camera was used by Mitic [104] to obtain a series of breast TPSF measurements enabling *in vivo* optical properties of breast tissue to be derived. Hall *et al* [102] used a streak camera to evaluate the spatial resolution of time-resolved transillumination imaging. Streak cameras are disadvantaged in terms of cost and detection sensitivity [98] when used in measurements involving thicker media in the sub-$100ps$ time scale where high spatial resolution is expected to be achieved.

Kirkby and Delpy [105] combine a cross-correlation technique [106] with an avalanche photodiode detector (APD) to sample the TPSF with a resolution of $100ps$ using relatively inexpensive components. Haller and Depeursinge [107] describe a photodiode detector with temporal resolution of about $10ps$. Other ultrafast optical gates have been investigated. Examples include: a parametric amplifier [108], second-harmonic generation [109] and Raman amplifier [110]. These have been assessed for their clinical utility[19,88,105,111-115]. However, these reports indicate that there is room for improvement in the spatial resolution by considering detectors with narrower time windows.

The effectiveness of gating methods depends strongly on the thickness and degree of scattering of the tissue. Experiments and Monte Carlo simulations [116] have demonstrated that total depolarization of an incident beam would occur after a penetration of about 10 transport lengths ($10l'$). The phase of the electromagnetic vector of the transmitted beam is randomized rapidly in the tissue with an exponential rate of μ_s'. This suggests that for thick samples coherent and polarization sensitive techniques are not effective in time gated imaging. However, *time-of-flight* (TOF) techniques remain attractive but are presently limited by the lack of adequate instrumentation. This deficiency has motivated the theoretical research outlined in this report which explores the potential of the TOF technique by utilising first photon detection.

---

to better system performance.

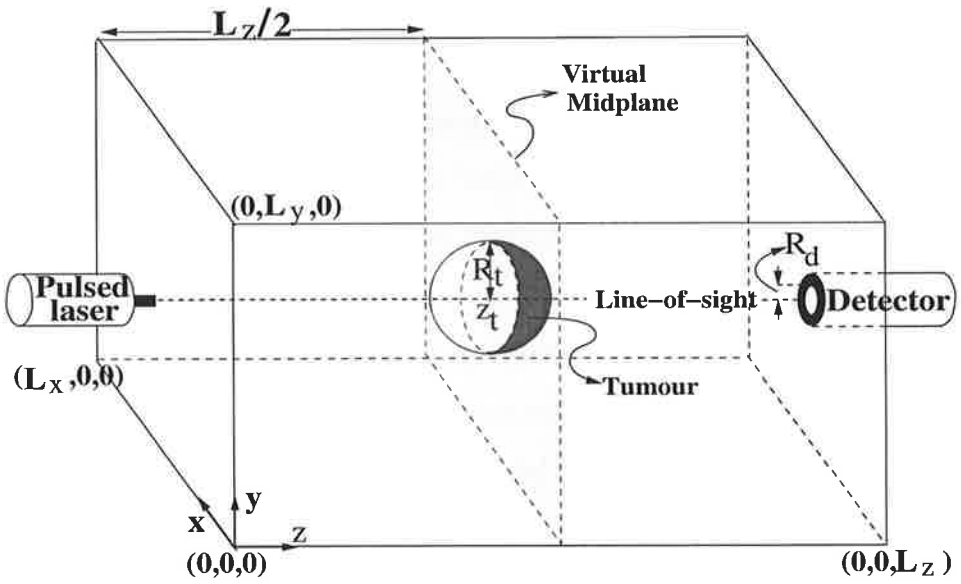

Figure 1.4: Set up of the system for the MC simulation.

1.6 Description of the system

1.6.1 Spatial characteristics

The simulation geometry of a time-resolved TI system used in this report consists of a collinear source-medium-detector geometry as shown in Fig. 1.4. For the purpose of the MC simulations, the medium is represented by a rectangular cube of dimensions $L_x \times L_y \times L_z$ and a δ-function source in space and time is assumed. The availability of fast lasers capable of delivering narrow pulses of a few tens of femtoseconds allows this assumption to be realistic. The laser beam is incident normally at the centre of the x-y surface at $z = 0$, i.e., $(\frac{L_x}{2}, \frac{L_y}{2}, 0)$. For the simulation of a scanning beam, this incident point may be varied. The detector was considered to be a 100% efficient, non-collimated disk located at $(\frac{L_x}{2}, \frac{L_y}{2}, L_z)$ facing the incident beam and forming a collinear source-medium-detector geometry. The beam axis or the detector line-of-sight along the z-direction is referred to as the central (or propagation) axis. For the purpose of this report the tumour is represented by a spherical inhomogeneity of radius R_t centred at $(\frac{L_x}{2}, \frac{L_y}{2}, \frac{L_z}{2})$ on the mid-plane.

1.6.2 Temporal characteristics

Figure 1.5 presents a schematic diagram of a possible single photon detection system. At each scan position, a ***sequence*** of fast laser pulses is made incident normal to the surface of the turbid medium. For each incident pulse a delayed logic pulse initiates the picosecond timer at a time equal to the ballistic (straight pass) flight time. ***Termination of the timing occurs on the detection of the first photon.*** A re-triggering reset by the next scanning pulse is required to eliminate the possibility of detecting the remaining photons in the same pulse. The recorded arrival time of the first detected photon from each pulse is then recorded and constitutes the temporal distribution for the first arriving photon for each scan position. This distribution is characterised by the temporal probability density function, $f_1(t)$, which is illustrated in Fig. 1.6. A shift in $f_1(t)$ between two different scan positions is indicative of a change in the optical characteristics of the medium. By rectilinear scanning across the medium, a 2-D map of the mean arrival time of the first detected photon can be created and displayed as a grey scale image.

1.7 Work of this thesis

The specific objective of this work is to propose and theoretically evaluate the limiting case of time-resolved TI, namely, a (single) first photon detection (FPD) system.

Collectively, the theoretical, Monte Carlo (MC) and the experimental results suggest that gating times of less than a few 10s of picoseconds are required for millimetre spatial resolution [117, 118] for a tissue thickness of about $5cm$. However, the scarcity of photons at such short times of flight [102] imposes severe constraints on the lower timescale achievable by systems which utilise conventional time-gated integrating detectors. It is therefore desirable to develop a FPD system, as a new experimental techniques, to achieve high spatial resolution. Also, new methods of theoretical analysis are implemented to achieve the objective stated above.

First, new MC methods are developed in chapter 3 to facilitate efficient simulations to acquire accurate spatial and temporal information about the transmitted photons

contributing to the sub-100 picosecond portion of the TPSF. This has not been achieved previously for turbid media similar to thicker biological tissues such as human breast. Chapter 2 outlines the standard MC procedure that forms the foundation for the indeterministic Monte Carlo (IMC) technique described in Chapter 3. The IMC, which is an extension of the controlled MC (CMC) [74], is a variance reduction MC technique which is based on the modification of longer trajectories to obtain shorter ones. The IMC along with a superposition technique is utilised in chapter 4 to fully construct the TPSF with high precision in the early sub-100ps region. To confirm the accuracy of the method the spatial resolution based on a conventional integrating time-gated system is evaluated and compared with the published experimental and theoretical results.

In chapter 5 the notion FPD is introduced and the statistics of the first detected photon are derived mathematically. The application of FPD to TI is evaluated assuming an ideal detector capable of detecting the first arriving photon with 100% efficiency (infinite extinction coefficient as well as zero background). The FPD system is also examined for the case of spherical inhomogeneities embedded in the centre of an otherwise homogeneous medium. The effect of embedded inhomogeneity (with different size and optical densities) and optical properties of the medium are also studied. A heterogeneous medium which resembles tissue more realistically will be considered in chapter 6. Practical and experimental considerations such as contrast and signal-noise-ratio (SNR) are discussed in chapter 7.

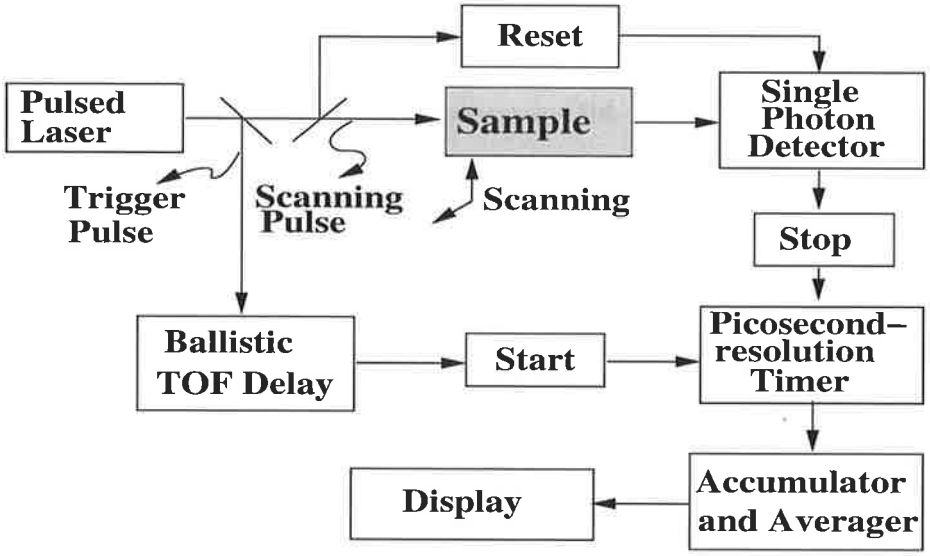

Figure 1.5: Schematic diagram for a FPD system. At each scan position a sequence of pulses is made incident onto the sample (medium). A signal triggers (starts) the timer at a delayed time (equivalent to the ballistic TOF). The first photon detected by the detector stops the timer. This first photon arrival time contributes to the temporal distribution recorded by the accumulator (see Fig. 1.6). The detector is reset by a re-trigger signal when the next pulse in the sequence is made incident onto the sample. After a statistically sufficient number of first photons is detected (from each pulse in the sequence), the averager produces a mean arrival time from the temporal distribution of these first detected photons which is then converted into a gray scale pixel.

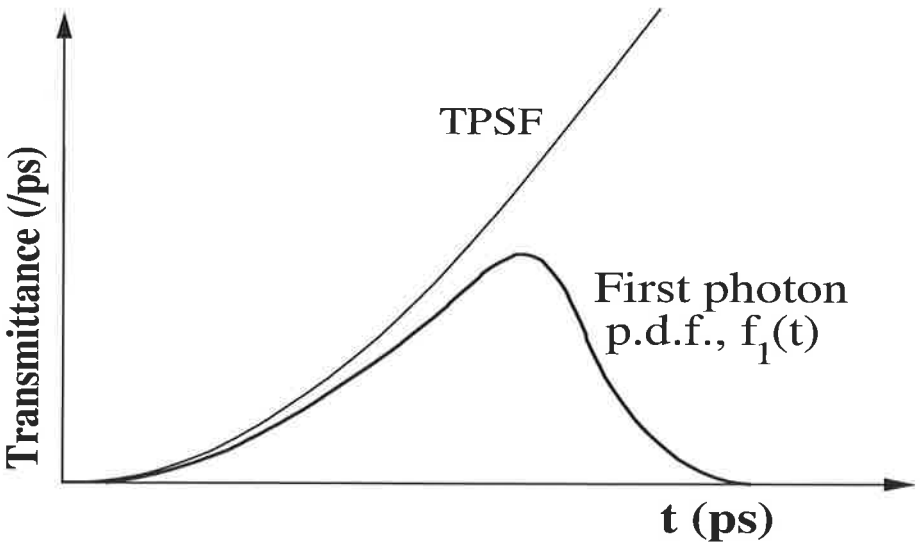

Figure 1.6: Illustrative curves showing the first arriving photon probability density function, $f_1(t)$, w.r.t. the early portion of the TPSF for the entire pulse.

Chapter 2

Monte Carlo simulation

2.1 Motivation

For medical diagnostic TI, the challenge is to solve the inverse problem of constructing an image of regions of differing attenuation (tumours) in a medium (normal tissue). Consider a fast laser pulse propagating through a turbid medium to a small detector. The earliest arriving photons, with the shortest times of flight, are more likely to have only interacted with the tissue close to the central propagation axis and hence potentially provide good spatial resolution as well as more accurate and useful information about the optical properties of the medium [15]. For the evaluation of snake photons, diffusion theory is no longer appropriate as the diffusion approximation is now violated. An exact analytic solution of the RTE may be considered, however, an analytic solution is unavailable except for extremely simplified situations [50, 44].

The Monte Carlo (MC) simulation [54, 73], which draws on the probabilistic nature of light propagation in the medium offers a flexible yet rigorous approach toward photon transport in turbid media. It can be used without imposing simplifying assumptions for situations where analytical methods are too difficult or unavailable.

Throughout this chapter, unless otherwise specified, a random number takes a value uniformly distributed over the interval $[0, 1]$.

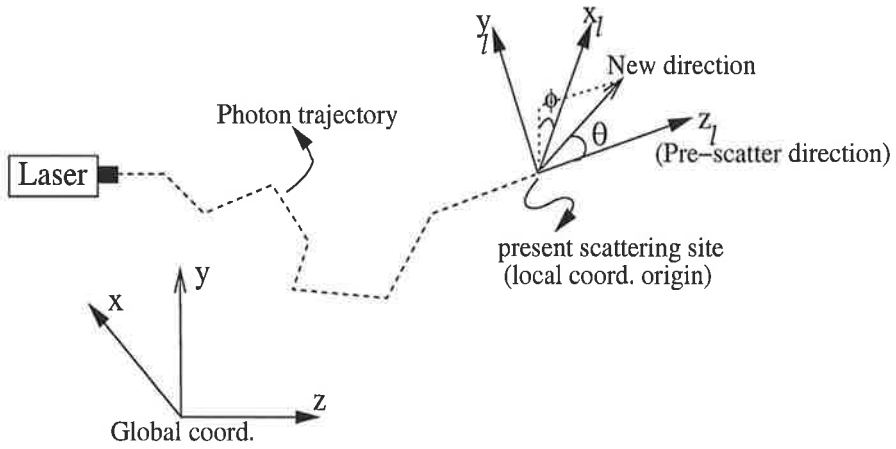

Figure 2.1: Global, x, y, z, and local (photon),x_l, y_l, z_l, coordinate systems.

2.2 Standard Monte Carlo (SMC) simulation

In the application of a MC simulation, a stochastic model is constructed in which the expected value of a certain random variable, or a function of several random variables, is equivalent to the values of a physical quantity to be determined.

In a TOF technique, the main physical quantity to be determined is the light intensity at the detector as a function of time. The light intensity is also a function of several random variables which are evaluated along each photon trajectory. These random variables are:

- the scattering azimuthal and zenith angles (ϕ, θ), measured w.r.t. the local photon coordinate (see Fig. 2.1),

- free scattering path-length between the scattering sites (l) and

- reflection at the boundaries (r).

The zenith angle θ is sampled [72] according to:

$$\cos(\theta) = \begin{cases} \frac{1}{2g}\left[1 + g^2 - \left(\frac{1-g^2}{1-g+2g\chi}\right)^2\right] & \text{if } g \neq 0 \\ 2\chi - 1 & \text{if } g = 0 \end{cases}, \tag{2.1}$$

where g is the anisotropy. Eqn. 2.1 may be derived from the distribution given by the Henyey-Greenstein's phase function:

$$f(cos\theta) = \frac{1-g^2}{2(1+g^2-2g\cos\theta)^{3/2}}. \tag{2.2}$$

The azimuthal angle ϕ which has a uniform p.d.f. is sampled according to:

$$\phi = 2\pi\chi, \tag{2.3}$$

where χ is a random number. The scattering angles are randomly sampled from their p.d.f..

The distribution of the scattering free path-length l is exponential with the p.d.f., $f(l)$, given as

$$f(l) = \mu_t \exp^{-\mu_t l}, \tag{2.4}$$

where μ_t is the attenuation coefficient. Given a random number, χ, then l can be randomly generated [72] as follows:

$$l = \frac{-\ln(\chi)}{\mu_t}. \tag{2.5}$$

When the trajectory intercepts a boundary, l is broken into two parts. The first part is the distance to the boundary, and the remainder is then re-evaluated by applying an adjustment according to the local parameters of the next medium. It has been shown [119] that it is equally valid to discard the remaining portion and generate a new l according to Eqn. 2.5.

To model the absorption, a random number, χ, is generated and the following condition is tested [73]:

$$\chi < \frac{\mu_a}{\mu_s}. \tag{2.6}$$

If the inequality holds, the photon is absorbed and the trajectory is terminated. Otherwise, the photon continues to propagate.

In determining the reflection at boundaries, total internal reflection is considered for incident angles bigger than the critical angle. In the case of normal incidence or boundaries of equal refractive indices, the surface is assumed to be non-reflecting and

total transmittance is applied. In all other cases, Fresnel's formula (see below) was used to determine the reflectance, r. In order to decide on reflection or transmission, a random number greater than r would rule that the photon crosses the boundary. On crossing the boundary, the exit angle is evaluated according to the Snell's law. The flow chart for a SMC algorithm is given in Fig. 2.2.

The SMC algorithm, as described above, results in the detection or loss of each photon. In order to increase the efficiency of the SMC, the concept of a single photon is extended to a photon *package*. When a trajectory is launched, it is given an initial *weight*, $W = 1$. At each scattering site, the probability of the photon being lost (by escape or absorption) is calculated and the weight is reduced accordingly [72] as described below. The detected photon package then represents the *probability* of detection for each incident photon.

At each boundary a *partial* transmittance, $1-r$, is calculated, where the reflectance, r, is determined by Fresnel's formula:

$$r = \frac{1}{2}\Big(\frac{\sin^2(\alpha_i - \alpha_t)}{\sin^2(\alpha_i + \alpha_t)} + \frac{\tan^2(\alpha_i - \alpha_t)}{\tan^2(\alpha_i + \alpha_t)}\Big),$$

where α_i and α_t are the incident and transmission angles respectively. The incident photon weight, W_i, reduces to $W_r = rW_i$ for the reflected portion, which continues to propagate within the original medium in a new direction. The transmitted portion of the photon package is assigned a weight $W_t = (1 - r)W_i$. This portion will either continue to propagate through the post-boundary medium or contribute to the signal according to this weight if it intercepts the detector.

Similarly, at each scattering site the probability of absorption is calculated and the photon weight is reduced according to the following:

$$W_f = W_i e^{-\mu_a l},$$

where W_i and W_f are pre and post-scatter weights. When the weight drops below a preset critical weight, W_c, a roulette procedure is applied to determine the fate of the trajectory. A trajectory survives the roulette if a random number is bigger than a "chance" (=0.1). In the case of survival, the weight is reduced by the value of the

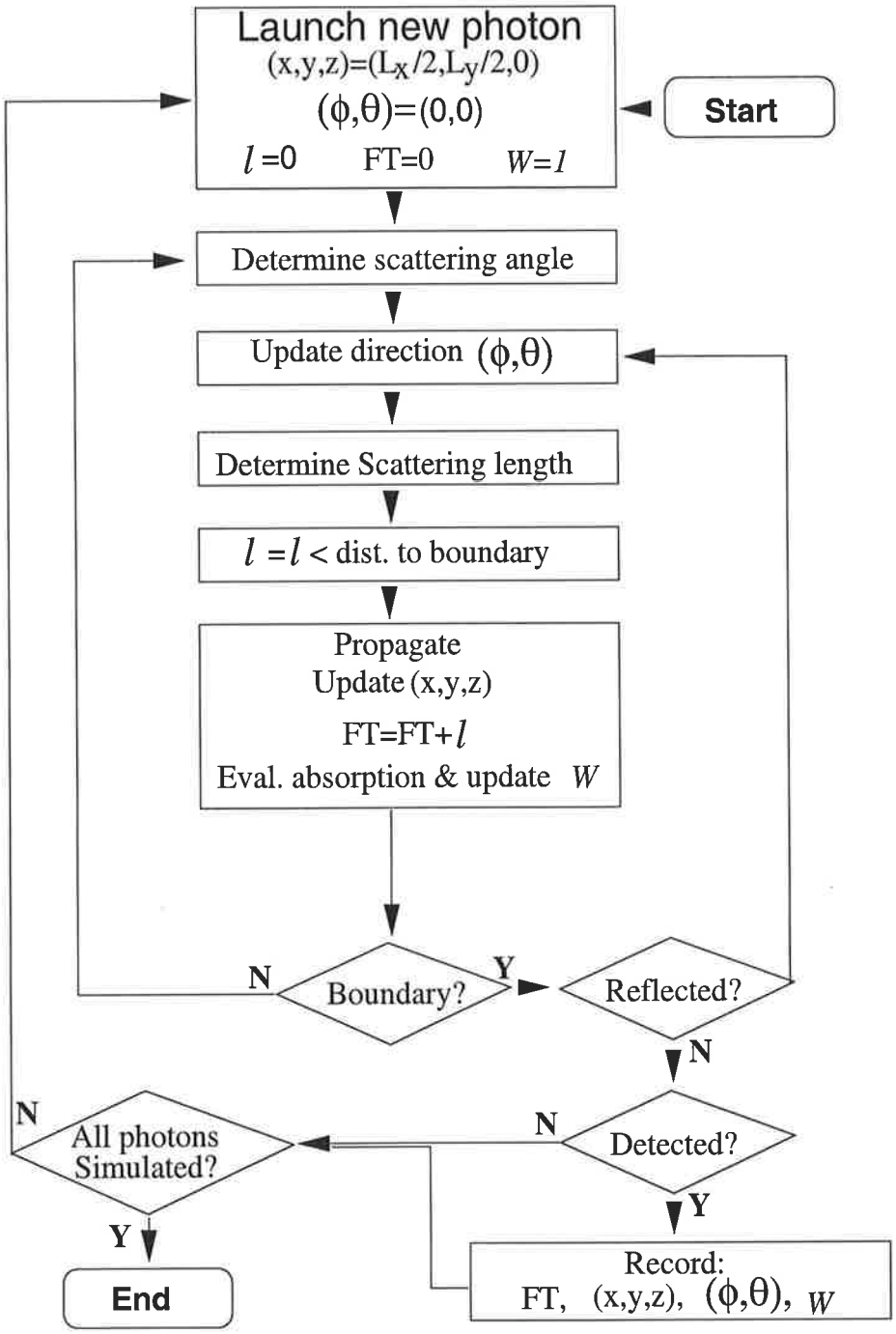

Figure 2.2: Flow chart for the standard Monte Carlo (SMC) simulation.

chance. Otherwise, for computational efficiency, the trajectory is terminated[1]. Also, when the trajectory exits the medium without intercepting the detector the trajectory is terminated.

As a large fraction of the trajectories is not detected due to their escape from the surface without contributing to detection, the above method of calculating the absorption effect is inefficient. This is because at each scattering site, the calculation is performed regardless of whether or not the trajectory will contribute to the detector signal. It is therefore more efficient to calculate the absorption effect only for the detected trajectories in the following manner. Let L be the total trajectory length, N, the total number of scattering events and l_i $(i \in 1, \cdots, N)$ the free path-length between each two consequent scattering sites. If the initial photon package is assigned a weight of unity, then the final weight is

$$W_f = e^{\sum_{i=1}^{N} -\mu_a l_i} = e^{-\mu_a \sum_{i=1}^{N} l_i} = e^{-\mu_a L}.$$

When inhomogeneities are present, it is straight-forward to show that:

$$W_f = e^{-(\mu_a^H L_H + \mu_a^I L_I)},$$

where $L_{H,I}$ represent the total path-length, and $\mu_a^{H,I}$, the absorption coefficients in the homogeneous (H) and inhomogeneous (I) parts of the medium respectively. This suggests that, if L_H and L_I are updated as the photon is propagated, the effect of the absorption can be accounted for after detection, by readjusting the weight as given above.

2.2.1 Validation of the algorithm used and computation procedure.

As the SMC algorithm forms the foundation of the Indeterministic Monte Carlo (IMC) technique described in chapter 3, the essential components of the SMC algorithm are validated here.

[1]The roulette procedure was not used in this work as the absorption was taken into account after the detection (see end of the present section). Moreover, this did not introduce a bias due to a safe value of the critical weight $W_c = 10^{-100}$ used in this work.

The corner stone of any MC algorithm is its (pseudo) random number generator (RNG). As well as other requirements which will be discussed later, it was essential to take computational efficiency into account when choosing the RNG. The RNG *mzran13* described by Marsaglia and Zaman [120] was implemented to produce uniformly distributed pseudo-random numbers in the interval $[0, 1]$. This algorithm has been validated to perform satisfactorily under several statistical and application tests (see for example [121]). Nevertheless, to ensure compatibility, the method of Sim and Nitschke [119] was followed to test *mzran13*. The results of the statistical and visual tests are presented in Appendix A. Here, the sampling of the propagation angles and scattering free path-length are considered. These are the main random variables on which the photon propagation is based.

Application test 1: The azimuthal component (ϕ) of the propagation direction is sampled uniformly as indicated by Eqn. 2.3. Therefore the uniformity tests described in appendix A also apply to the sampling of θ. The cosine of the zenith angle $\cos(\theta)$ is sampled according to Eqn. 2.1. It is not obvious whether the distribution obtained follows that dictated by the Henyey-Greenstein's phase function as given by Eqn. 2.2. To test this, a sample size of $N = 10^6$ was generated for the variable $\cos(\theta)$. The sample was then binned into 100 bins of equal size over the interval $[-1, 1]$. Figure 2.3 presents the observed (sampled) and the expected (theoretical) distributions.

Application test 2: A second application test, the scattering free path-length, l, was sampled according to Eqn. 2.5 whose distribution is expected to be exponential described by Eqn. 2.4. Figure. 2.4 compares the results of a randomly sampled l with the expected (exponential) theoretical distribution.

A χ^2 test showed that the two sampled distributions of $\cos(\theta)$ and l are equivalent to their respective mathematical distributions at 95% or better confidence level.

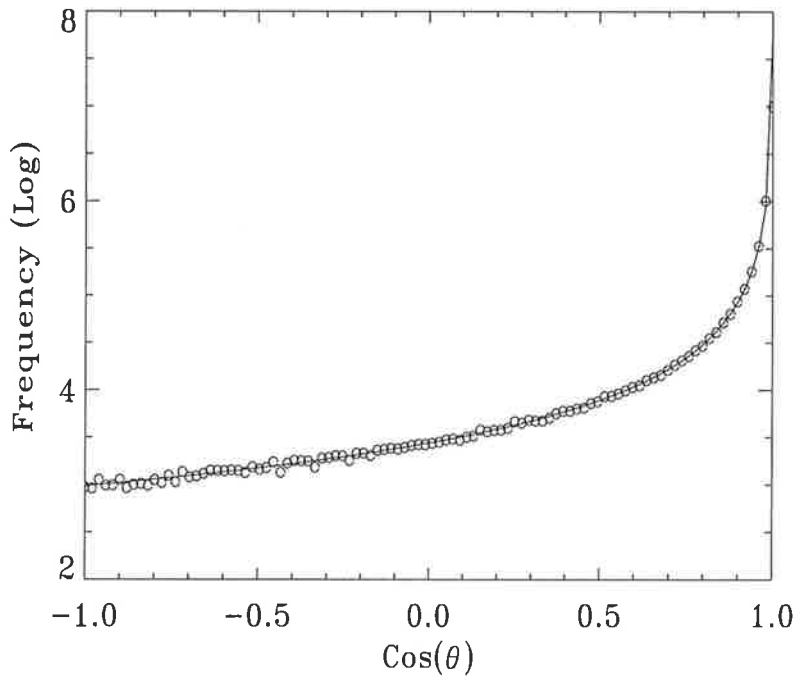

Figure 2.3: Observed distribution (o) of the random variable $\cos(\theta)$ sampled from the distribution given by Eqn. 2.1 with a sample size of 10^6. The expected theoretical curve as given by Henyey-Greenstein's phase function (Eqn. 2.2) is also presented.

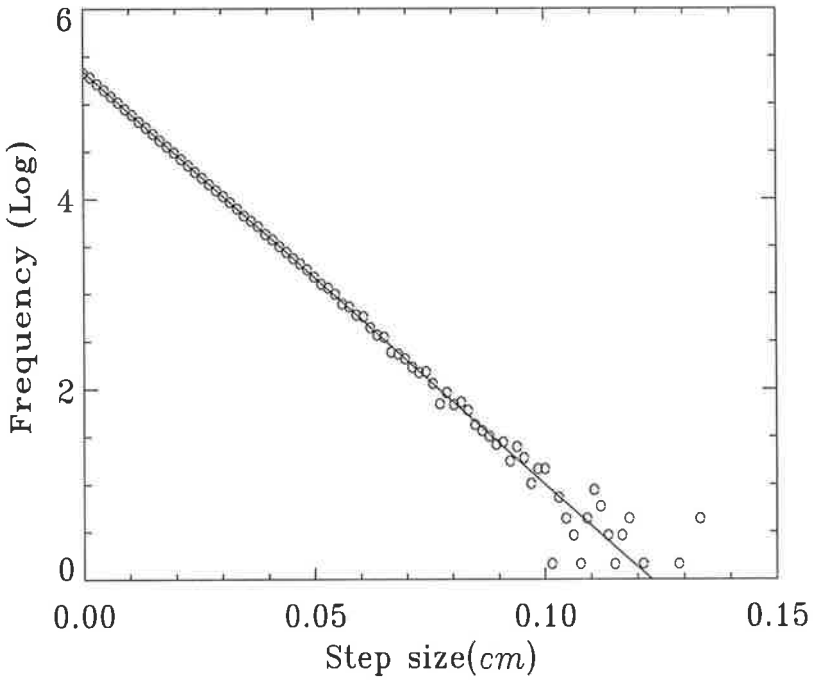

Figure 2.4: Comparison of a sampled (○) scattering free path-length, l, as given by Eqn. 2.5 and the expected exponential distribution suggested by Eqn. 2.4.

2.2.2 Execution of the MC algorithm

To produce the results of the following chapters, each MC simulation was run in parallel and independently on an equivalent[2] network up to 10 Digital UNIX 500au Personal Workstations. The number of machines utilised depended on the number of photons to be simulated. When more than one machine was utilised, the seeds to the RNG were generally extracted from the clock time of each machine and the simulations started 7 seconds apart to ensure different seeds and hence different random number sequences. The seeds extracted from the clock time were within the acceptable range for *mzran13* [120]. Also for reproducibility and future cross checks one of the machines utilised the standard seed which would consistently produce the same sequence (and hence MC results for a specified medium). It is further noted that the period length of *mzran13* is 2^{125}. This length is sufficiently large to ensure no sampling repetition[3].

2.3 Conclusion

The standard Monte Carlo (SMC) simulation as applied to a turbid medium presented by Fig. 1.4 has been described. The overall performance and validation of the SMC algorithm as applied to solve the RTE for a given source-medium-detector geometry is discussed in chapter 3. However, in this chapter (and Appendix A) the RNG, *mzran13*, which provides the algorithm with a uniformly distributed random number over $[0, 1]$ has been assessed and validated by means of statistical, visual and application tests.

[2]At any given time, up to 35 workstations were utilised, however, the availability of CPU time dictated that effectively only about 25% of the full capacity was taken by the simulations.

[3]For the simulation of 10^9 photons, a conservatively safe sequence length of about $10^{14} \ll 2^{125}$ is sufficient to ensure no sampling repetition. This conservative estimate assumes about 10000 (for $\mu_s = 200$ and $L_z = 5.0cm$) scattering events per photon trajectory. To determine angles, free path-lengths, reflection etc., RNG is called at most 10 times at each scattering event. Moreover, by searching the output data for the re-occurrence of the first few detected events, the collected data from a simulation of 10^9 photons showed no sampling repetition.

Chapter 3

Indeterministic Monte Carlo (IMC) Simulation

3.1 Motivation

In this chapter an Indeterministic Monte Carlo (IMC) simulation technique is proposed for the efficient construction of the early part of the TPSF. This provides an accurate profile of the TPSF in the short TOF region where the probability of the photon being detected is of the order of one per pulse. The earliest arriving photons are more likely to have interacted with the tissue close to the propagation axis and hence potentially may provide good spatial resolution as well as more accurate information about the optical properties of the medium [15]. Such information can then be used to study the limit of spatial and contrast resolution achievable with fast TOF techniques. It also provides a useful tool for the analysis of single photon detection in TI, as will be described in later chapters.

Consider a fast laser pulse propagating through a scattering medium to a small detector. Beer's law suggests that the intensity decreases exponentially with the thickness, L_z, of the scattering medium. Experimental studies (see Fig. 5 of [102]) have shown that the intensity of the detected pulse also decreases approximately exponentially with flight times in the region of a few hundred picoseconds from the ballistic time, L_z/c. The thickness of typical tissue samples of interest, $\sim 5cm$, and short gat-

ing times result in very small detection efficiencies and a poor signal-noise-ratio (SNR). Therefore, the probability that a photon trajectory intersects with the detector within a given time becomes so very small that a very large number of initial trajectories is necessary to produce reliable statistics when using the SMC simulations. This requires extensive computational time.

Variance reduction techniques such as the semi-analytical [75], controlled (CMC) [74] and condensed [76] Monte Carlo techniques have been introduced to reduce the computation time in Monte Carlo simulations. This chapter describes a new Indeterministic Monte Carlo (IMC) technique which is an extension of the CMC method proposed by Chen & Bai [74]. Chen & Bai introduced an attractive point behind the detector into the simulation with an adjustable attractive factor that forces photons to propagate along directions more likely to intersect with the detector. The increase in the number of trajectories intercepting the detector is compensated by reducing the incoming photon weight, W_i at each scattering site according to the following formula:

$$W_f = \frac{W_i}{P_\varepsilon(e_f.e_a)} \int\int_{4\pi} \frac{1}{2\pi} f(e_i.e'_f) P_\varepsilon(e'_f.e_a) d\Omega'_f, \tag{3.1}$$

where subscripts i and f denote the initial and final states, f is the phase function and unit vectors $e_{i,f}$ denote the pre- and post-scatter propagation directions and e_a is the direction of the attractive point. P_ε, a function of the attractive factor ε, is used as a probabilistic discriminator against unfavourable scattering directions (away from the attractive point). A correction for absorption is applied on the basis of the final path-length. An increase in the attractive factor forces the selection of smaller scattering angles from the direction of the attractive point (detector), e_a. This results in shorter trajectories and hence earlier times can be studied. Although a large attractive factor will result in a distortion of the later part of the TPSF [74], its effect decreases as the shorter times of flight are approached and the leading edge (near the ballistic time) of the TPSF can be estimated.

The objective of this chapter is to describe a new method to improve the CMC method of Chen & Bai by introducing the IMC which extracts shorter photon paths from the later arriving photons. In order to assess the IMC technique, the results are

compared with those of SMC and CMC simulations in calculating the TPSF. A comparison is also made with the theoretical results of diffusion theory [55] and random walk theory [79].

3.2 Theory

3.2.1 The indeterministic approach

The temporal profile of the detected photons from an incident pulse (assumed to be a δ-function in time and space) can be rescaled by the number of photons in the incident pulse to represent the temporal probability density function, $f(t)$, for the arrival time of a single photon. A photon which never reaches the detector is considered as one which arrives at a time $t \to \infty$, then:

$$\int_0^\infty f(t)dt = 1.$$

The collection of all photon paths (*events*) forms a probability space [134]. The *flight-time* is a random variable which maps from this space to that of positive real numbers representing the time domain. In practice, time is measured in a discrete manner. Therefore the probability of detecting a particular photon trajectory is proportional to the value of $f(t)$ at a time represented by the flight-time associated with that trajectory. Before the detection of the photon, $f(t)$ describes the probability of a photon arriving at the detector within a given time interval. However, after the photon is detected the arrival time becomes definite and is referred to as the outcome of the simulation.

An already detected photon has a definite path (and flight-time) and may be considered as *determined.* An *indeterministic* approach (i.e., not pre-determined) is to assume that a particular detected photon with its associated trajectory, $\mathbf{r}(t)$, is a superposition of a number of components representing several other physically allowed trajectories. Each of these trajectories is assigned a certain weight, the initially detected trajectory being assigned the heaviest weight, that is:

$$p(\mathbf{r}(t)) = \textstyle\sum_i W_i p(\mathbf{r}_i(t)),$$

where $p(\mathbf{r}(t))$ is the probability of occurrence of a trajectory $\mathbf{r}(t)$. This is similar to the *path integral* technique in relation to the classical path proposed by Feynman [80]. The random variable, flight-time, is a function of these paths giving a time T_i for each path with an associated weight W_i. On this assumption, once a primary photon is detected, one can then proceed to find *faster component trajectories* (shorter paths) by re-initiating the propagation from the point of maximum delay in the previously detected path (see Fig. 3.1).

3.2.2 Allocation of photon trajectory weights

For greater efficiency, the method of Chen & Bai [74] (CMC) is used initially to propagate a photon. On detection, the flight-time T_0 is recorded and a weight W_0' is allocated in accordance with Eqn. 3.1. The resulting trajectory is referred to as the *initial* trajectory. The photon propagation is then re-initiated from the point of maximum delay (cf. section 3.3.1) until it is detected again or its flight-time exceeds a time limit. This may be repeated with each detection resulting in the generation of a new trajectory referred to as the i^{th} component with $i \in \{0, 1, \cdots\}$ and the initial trajectory being the 0^{th} component.

The detected i^{th} component photon trajectory is allocated its flight-time, T_i, a weight, W_i' (in accordance with Eqn. 3.1) along with the total number of *attempts*, A_i, the path was modified before the photon is detected again. The number of attempts for the initial trajectory is taken to be 1.

The *raw* results obtained in this manner need to be corrected as follows. For each component a new weight, W_i^A is calculated as:

$$W_i^A = W_i'/A_i, \qquad i \in \{0, 1, \cdots\} \tag{3.2}$$

which reflects the fact that a modified path is less probable because more attempts are required in obtaining it.

A second normalisation correction aims at the conservation of photon number. In order to achieve this, the weighting factors W_i^A for all components should be scaled

according to:

$$W_i = \alpha W_i^A, \tag{3.3}$$

such that the final weighting factors W_i add up to the weight of the initial component. This demands the final weighting factors satisfy the following equation:

$$\sum_i W_i = W_0'. \tag{3.4}$$

The proportionality constant α in Eqn. 3.3 is the same for all components. This linear scaling ensures the linear relationship between the intensity of the incident and the detected pulse. Solving the above equations simultaneously for α and for the final weights, W_i, gives:

$$\alpha = \frac{W_0'}{\sum_j W_j'/A_j}, \qquad j \in \{0, 1, \cdots\}$$

and

$$W_i = \frac{W_0'}{\sum_j W_j'/A_j} W_i'/A_i. \tag{3.5}$$

This result (Eqn. 3.5) means that all trajectory components can be assumed to be the result of real photon paths, each with a flight-time of T_i and weight W_i.

Note that Eqn. 3.5 reduces to $W_0 = W_0'$ when only one (the initial) trajectory is detected. This reflects that fact that in this case no corrections are required as is the case with all trajectories which are produced without using the IMC technique. This means that the IMC naturally reduced to CMC if no re-initiation of detected trajectories is implemented.

3.3 Method

3.3.1 Description of IMC simulation and path modification

A collinear source-medium-detector geometry was simulated as shown in Fig. 3.1. The assumptions were made that the source was a δ-function in space and time, the detector a 100 per cent efficient non-collimated disk, and the medium was homogeneous.

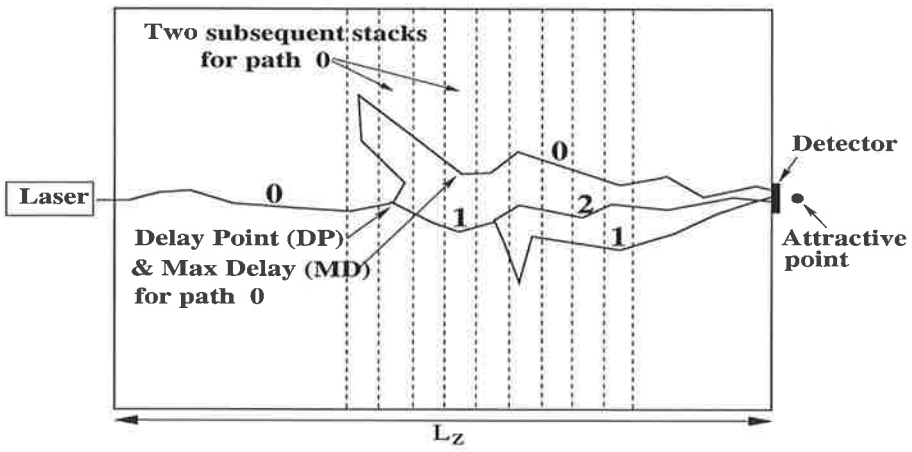

Figure 3.1: Representation of trajectories taken by components of a detected photon. The initial (path 0) and two modified trajectories (paths 1 and 2) are shown. On detection, a flight-time, weight and number of attempts, (T_0, W_0', A_0), (T_1, W_1', A_1) and (T_2, W_2', A_2) are assigned to each detected path 0, 1 and 2 respectively. In recording the history of the trajectory, the photon (path 0), which interacts at the delay point, DP, and is scattered back to a preceding stack is not recorded until it jumps forwards.

The flow chart in Fig. 3.2 illustrates the algorithm for the IMC technique (see also Appendix B). The dashed sub-routines and arrows delineate the implementation of the IMC technique. If these are skipped, the algorithm reduces to the CMC algorithm, which in turn reduces to a SMC algorithm described in chapter 2 with expanded flowchart presented by Fig. 2.2. A photon trajectory was simulated (Chen & Bai [74]) through random generation of a free path-length and propagation direction at each scattering site in the medium and the weighting factor W' was updated according to Eqn. 3.1.

A virtual stack system which divides the medium in equally spaced slab partitions along the direction of photon propagation was created as shown in Fig. 3.1. The first time the trajectory advanced to a new (not necessarily neighbouring) stack along the propagation axis, the photon (i.e., all its parameters) was recorded. At this point, a delay (D) was also recorded. This delay was the difference between the flight-time at the new and the most recent stack at which the photon was previously recorded.

To find the site (within 0.1mm accuracy) where the longest delay occurred, on the successful detection of a photon within a pre-set flight time limit (FTL), a *maximum*

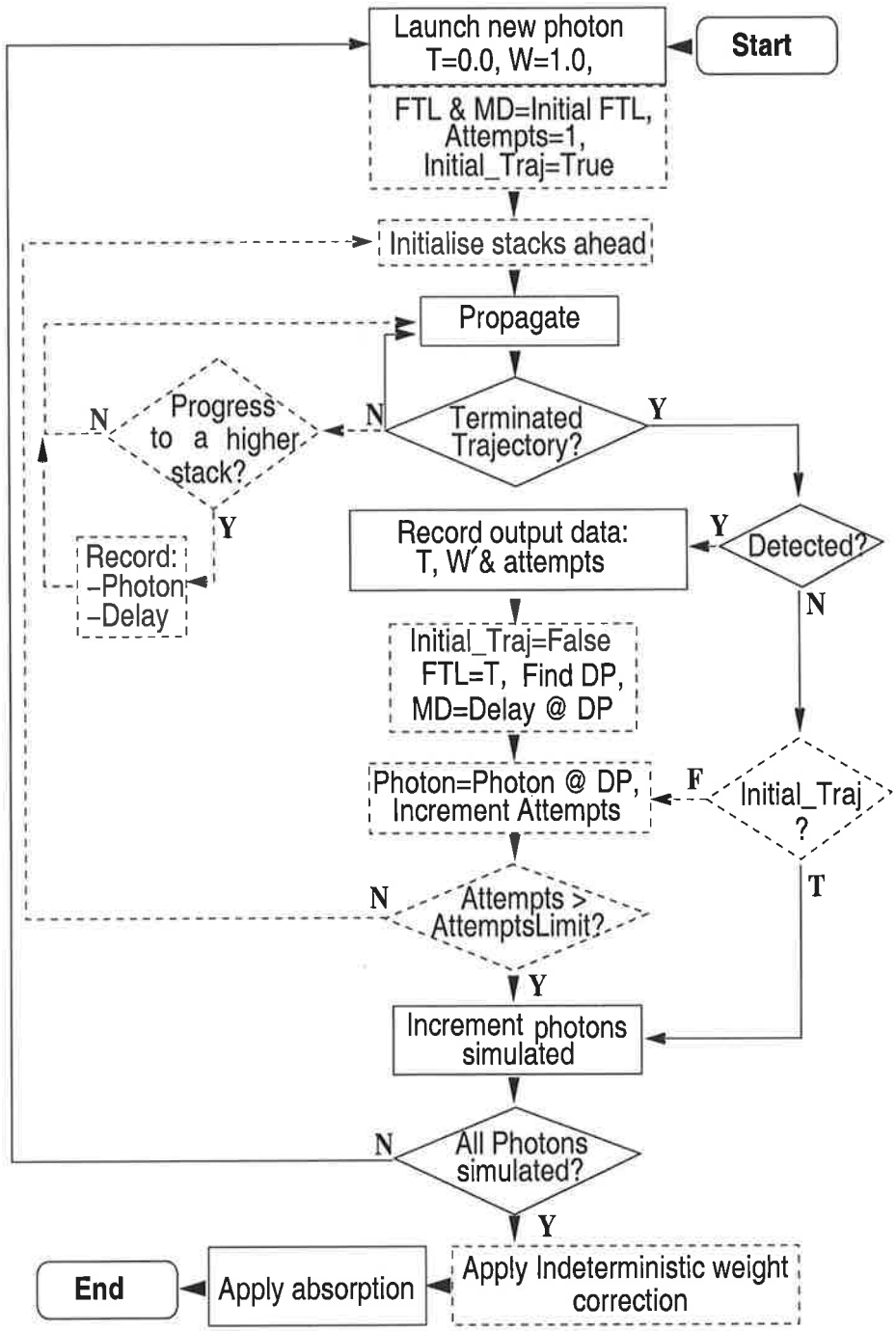

Figure 3.2: Flow chart of the algorithm for the IMC technique. The dashed arrows and sub-routines highlight the IMC sections. The propagation sub-routine is based on the CMC algorithm which also updates T and W' for each component.

delay (MD) was determined by comparing the recorded delays, D, along the trajectory. The trajectory was then re-initiated, from the Delay Point (DP), as recorded by the stack immediately prior to a point of maximum delay, where a new direction and free path-length was generated. The Delay Point was where the photon was recorded on its entry in the respective stack. The FTL was also re-initialised to take the value T, the flight-time of the previously detected (parent) trajectory (component). This ensured each newly detected trajectory had a smaller value of T than its parent component.

On launching each new photon, the value of the MD was re-initialised to take a conservative value of the initial FTL. The latter may vary depending on the time-scale of interest (cf. section 3.4 and chapter 4).

A trajectory was terminated if any one of the following occurred:

- the flight-time (T) exceeded the initial or updated FTL,
- the delay (D) exceeded the maximum allowable delay (initial or updated MD),
- the weight W' reached a lower limit pre-set by a critical weight,
- the number of *attempts* exceeded a pre-set *Attempts Limit* (A), or
- the trajectory exited the medium.

For each detected photon trajectory, the algorithm outputs a flight-time T, a weight W' and the number of attempts A. Weight corrections were applied retrospectively to all detected photons in accordance with Eqn. 3.5 outside of the MC simulation.

3.3.2 System parameters and simulation specifications

An infinitely thin, pulsed pencil beam, a $1.0mm$ in diameter detector and a slab of $5cm$ thick tissue were simulated. The optical properties of the medium were [24] $\mu_a = 0.1cm^{-1}$, $\mu_s' = 5cm^{-1}$, $g = 0.95$ and $n = 1.56$. The number of stacks was pre-set to 500 (0.1 mm equivalency) and an initial *attempts limit* of 2000 was chosen. This number is not critical, being a compromise between the statistical variation acceptable and computational time (cf. Fig. 3.8). An initial FTL was set to be $520ps(\equiv 10cm$

path-length) when each new photon was launched. An attractive factor of 0.4 was found to result in the construction of the TPSF in the timescale where the SMC could produce the corresponding TPSF to facilitate comparison. The attractive point was positioned $0.5mm$ behind the detector to give a 90 degree acceptance angle.

I corrected upto here because Peywan came to disturb me. If I die then it is her fault for not having finished this. 10:47, 2/3/2003.

3.3.3 Algorithm evaluation

To evaluate the accuracy and efficiency of the IMC technique, the TPSF was generated by IMC, CMC, SMC methods and analytical techniques of diffusion and random walk theories. The IMC technique was bench-marked against the CMC and against the SMC technique for the time scales for which overlap occurred (cf. Fig. 3.3). The numbers of simulated photons were 1.8×10^8 for the IMC, 6×10^8 for the CMC and 10^9 for the SMC simulations. Standard deviations (σ) for the simulated TPSFs using IMC and SMC were calculated as a function of flight-time. The standard deviations for time intervals of $100ps$ centred on each point are shown in Table 3.1.

The efficiency of the IMC algorithm was compared with that of the CMC by simulating equal number of photons as well as equal computation times. To quantify the efficiency, the number of simulated photons was reduced in the IMC simulation to yield the same statistics in the TPSF as that of CMC for which a higher number of photons was simulated.

The efficiency of the IMC technique was also studied by considering the average reduction in the flight time compared with that of the initial trajectory as a function of the number of attempts made in modifying the trajectory. The effect of the number of stacks and the position of the attractive point were also assessed.

3.4 Results and discussion

The TPSFs presented here are normalised to represent the transmission per single incident photon and the flight times are relative to the ballistic time L_z/c.

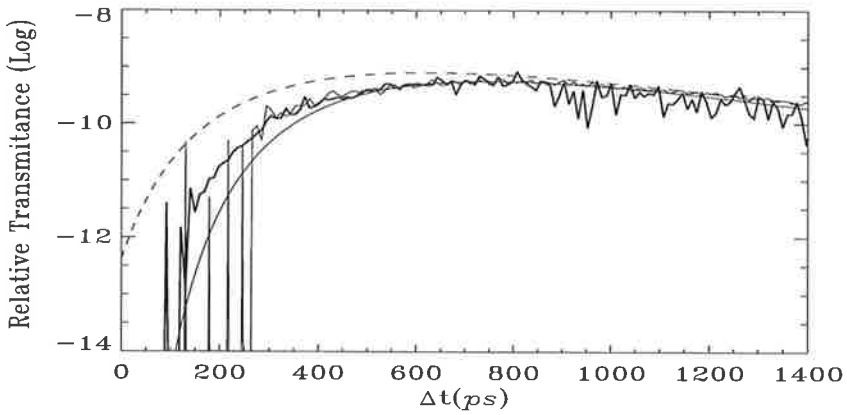

Figure 3.3: The temporal point spread function (TPSF). Thin noisy curve: SMC, dashed smooth curve: diffusion theory [55] and smooth curve: random walk [79]. Thick noisy curve: IMC with CMC (0-260ps) and CMC (260-1400ps).

$\Delta t(ps)$	IMC($\times 10^{-10}$)		SMC($\times 10^{-10}$)	
	I/I_0	$\sigma(\pm)$	I/I_0	$\sigma(\pm)$
150	0.08	0.0059	–	–
250	0.6	0.033	–	–
350	3.0	0.14	2.4	0.18
450	5.8	0.24	6.6	0.40
550	7.7	0.32	7.4	0.43
650	8.3	0.38	8.6	0.47
750	9.0	0.48	9.7	0.50
850	9.2	0.47	11.0	0.55
950	9.1	0.45	13.1	0.54

Table 3.1: Standard deviations calculated for the IMC and SMC techniques for the data presented by Fig. 3.3. The mean values of the transmittance per incident photon have also been included. The standard deviations were calculated from the variance of the data w.r.t. a smooth fit to the data within each 100ps interval.

Accuracy: Figure 3.3 shows the TPSF as evaluated by both the IMC and CMC techniques along with the results of calculations using SMC, diffusion theory [55] and random walk [79] theory. This figure and Table 3.2 show that the SMC requires a prohibitively long computation time to generate sufficient photon trajectories shorter than $\sim 350ps$. In a shorter computation time (Table 3.2), the CMC can reduce this to $\sim 160ps$ while the IMC generates enough photons to provide information near $110ps$ (see Fig. 3.6).

As reported by Chen & Bai [74], Fig. 3.3 suggests that some distortion introduced by the CMC occurs in the later part of the TPSF. However, the accuracy of this technique is better than 10% for trajectories with an excess flight time of less than $800ps$. This time range, over which the CMC and SMC agree, decreases as larger attractive factors are used. This reduction is compensated by improved statistics in the earlier part of TPSF. Table 3.1 shows that in the range $350 - 750ps$ where the IMC and SMC data sets may be compared, the difference is within 2σ. Beyond $750ps$ the IMC differs from the SMC by more than 2σ. While random walk and diffusion theories model the later part of TPSF with better accuracy, the results produced by the IMC technique are clearly more satisfactory for the earlier parts for which the excess time, $\Delta t < 400ps$.

Precision: Table 3.1 presents standard deviations for the IMC and SMC techniques for the results presented in Fig. 3.3. The figure demonstrates that the standard deviations of the IMC technique are less that those of SMC for a flight time of less than $700ps$. The results presented in Figs. 3.4 and 3.5 compare the IMC (thick line) and CMC methods of simulation with an expanded time scale in the early part of the temporal profile. Figure 3.4 shows the result of using an equal number of photons (1.8×10^8) for both methods. For equal number of photons the IMC technique extends the data set from $190ps$ to $110ps$. Figure 3.6 compares the same results of IMC technique as in Fig. 3.4 with that of the CMC for which an increased number of input photons, 6×10^8, was used. A comparison of the two figures shows that the IMC method is capable of extracting early arriving photons from those taking longer paths and calculates the TPSF more precisely.

Efficiency: Figure 3.6 also compares the results obtained over equal computation

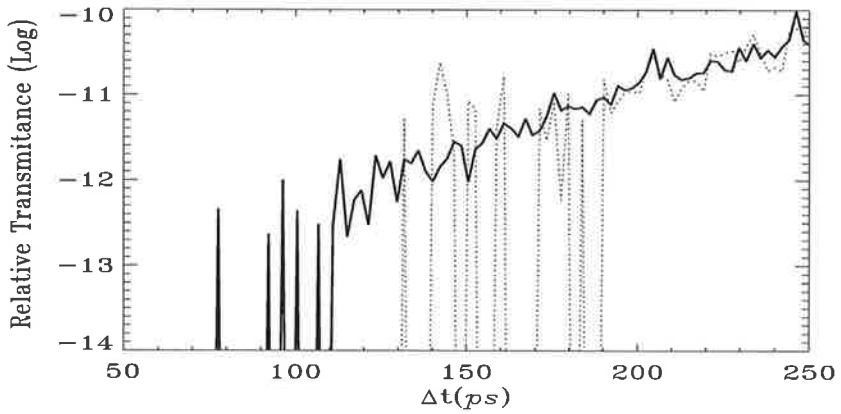

Figure 3.4: Expanded time scale to present the early part of the TPSF produced by IMC (thick curve) and CMC (dotted curve) methods. An equal number of photons (1.8×10^8) were used to produce the results.

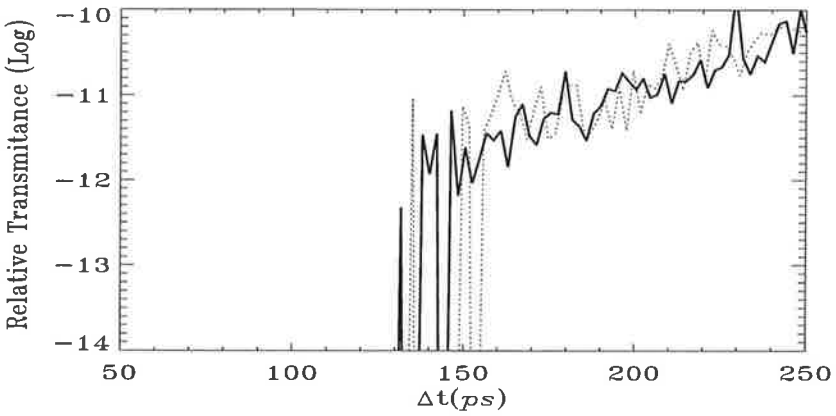

Figure 3.5: This figure also presents similar results shown in Fig. 3.4 with 4×10^7 photons used to produce results for IMC (thick curve) compared to 6×10^8 used for CMC (dotted curve).

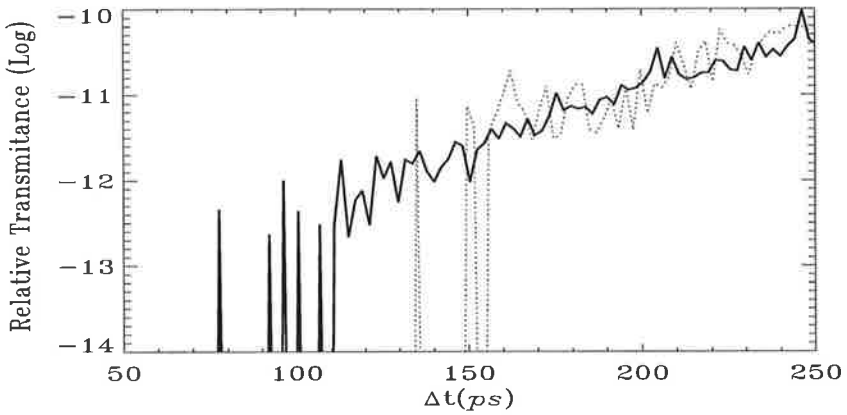

Figure 3.6: As in Fig. 3.4 with equal computation time for both IMC (thick curve) and CMC methods (dotted curve). The total computation time corresponds to 1.8×10^8 photons simulated using IMC method.

Simulation method	Photons simulated	Comp. time (h)	Time scale (ps)
IMC	4×10^7	167	0-260
CMC	6×10^8	700	0-260
CMC	7×10^7	82	0-800
SMC	10^9	2200	0-800

Table 3.2: Comparison of the computation time for the IMC, CMC and SMC methods. The number of simulated photons where chosen to yield the same statistics (cf. Figs. 3.3 and 3.5). The time scale refers to the excess flight time w.r.t. L_z/c.

times with 1.8×10^8 photons used in IMC. The corresponding number of photons for the CMC method was found to be 6×10^8 (cf. Table 3.2). Again, the superiority of the IMC technique in predicting the TPSF in the shorter time scales is clearly demonstrated over the time scale of $160ps$ down to $110ps$. In order to compare the time efficiencies, the number of simulated photons in the IMC simulation was reduced (4×10^7) to yield the same statistics (cut-off) in TPSF as that of CMC with 6×10^8 simulated photons. The results are shown in Fig. 3.5 and Table 3.2. The significant reduction (by a factor of 15) of photons simulated gives rise to a reduction by a factor of at least 4 in computation time. The results of Figs. 3.4 and 3.5 and Table 3.2 for a given computation time demonstrate the ability of the IMC technique to extend the CMC method and predict the TPSF in the shorter time scales.

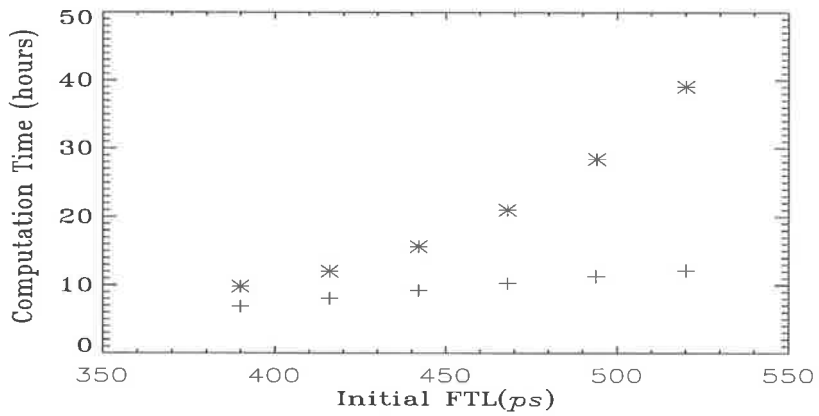

Figure 3.7: Computation time (for 10^7 photons) as a function of initial FTL shown for IMC(∗) and CMC(+) techniques. The IMC becomes computationally less efficient as longer initial FTL is used.

Influence of flight time limit (FTL) and number of attempts limit: Figure 3.7 compares the computation time taken for the simulation of 10^7 photons as a function of the initial FTL (also used as a limit in CMC method). In performing these simulations a network of 10 work stations (Digital Unix, PWS 500au) was utilized and the results present the total simulations time from all machines. The extra time taken by the IMC as indicated in this figure is offset by increased statistics in the earlier time scale. This was demonstrated by the results of Fig. 3.6 in which the efficiency of the IMC was assessed based on equal computation times.

Figure 3.8 presents the average reduction in the flight time compared with that of the initial trajectory as a function of the number of attempts. The figure shows that the beneficial reduction decreases as a function of the number of attempts. This is because as the FTL reduces, the maximum delay is on average smaller (as photons have less time to wander around the medium) and hence more attempts are required to modify an already relatively short path.

The results of Fig. 3.7 together with those of Fig. 3.8 also indicate that a choice of a large initial FTL decreases efficiency. This is due to the fact that longer trajectories are most likely to have their delay point far from the detector, possibly in the first few stacks. On the other hand, a smaller initial FTL results in a reduction in the detected

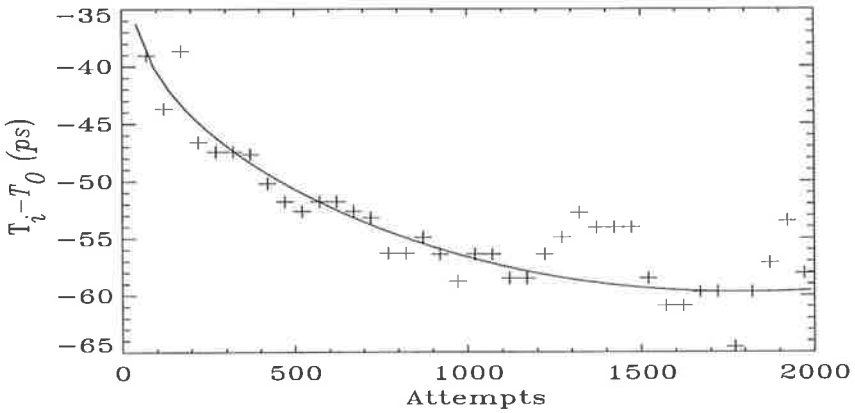

Figure 3.8: The average reduction in the flight time obtained as a function of *attempts limit* and an initial flight time limit of $260ps$. The smooth curve is the least square fit to the data.

trajectories and hence reduces the applicability of IMC technique. Figure 3.8 suggests that the efficiency decreases as larger *attempts limits* are used. A small *attempts limit* is, however, not very useful as shorter components will not be found when the FTL is large. The optimal choice of the *attempts limit* and initial FTL depends on the system parameters and geometry.

Influence of number of stacks: The computation time for the IMC technique was found to decrease as the number of stacks increases. Finer stacks locate the delay point (DP) more precisely which prevents either un-necessary backtracking or possibly missing delay points that are too close. For example, the computation time was found to decrease by a factor of 0.72 when the number of stacks were increased from 50 to 500. A stack width of less that the mean free path-length is not efficient. Moreover, too small stack width increases the computation time as this increases the time spent in recording the photons and searching back for the delay point.

Influence of attractive point position: The position of the attractive factor was found to be optimal at a distance equivalent to the the radius of detector and directly behind it. This position, comparable with the detector size, gives the attractive point a 90 degree field of view. A position too far behind the detector would result in the loss of trajectories that have been followed and just miss the detector.

3.5 Conclusion

An indeterministic approach to the trajectories taken by the photons *after they have been detected* has been demonstrated to lead to an efficient technique for the extraction of shorter trajectories (faster components). This facilitates the accurate construction of the very early part of the temporal profile of a fast laser pulse transmitted through a turbid medium. For the given geometry and attractive factor (0.4), the IMC technique reduces the computation time by a factor of at least four compared to the Controlled MC method of Chen & Bai. This is significant when simulation time can be reduced from weeks to days.

Although a CMC method was employed to provide the initial unmodified photon paths, the proposed IMC method can be used independently of other variance reduction techniques. However, it is more efficient when used in conjunction with methods such as the one of Chen & Bai because the IMC technique relies on a modification of (and hence existence of) an already detected trajectory to find a faster one.

Chapter 4

Validation of IMC: Spatial resolution in conventional integrating time-resolved TI.

4.1 Motivation

The objectives of the present chapter are: (a) to validate the IMC technique. This is achieved by re-evaluation of the spatial resolution associated with a conventional integrating time-gated system for longer time scales and then bench marking the results against the experimental results of Hebden *et al* [122, 123], (b) to assess the spatial resolution potentially achievable in an integrating time-resolved TI for short times of flight ($< 200ps$) and (c) to fully construct the TPSF for the time scale of $10ps$ and longer.

The spatial resolution Δx of an imaging system is related to its spatial frequency resolving power which is assessed based on the limiting spatial frequency resolvable by the observer (human or non-human). Previously a USAF resolution test chart [124] consisting of parallel bars of diminishing frequency was the standard tool to assess this resolving power. In simple terms, two bars will be resolved if the dip in central image density is greater than some threshold quantity determined by the total noise. On replacing the bars with slits, this leads to consideration of the line spread function

(LSF). The modulation transfer function (MTF) which is the Fourier transform of the LSF acts as a weighting function for any particular spatial frequency. The spatial resolution is commonly defined as the value corresponding to a 10% response on the MTF [124, 125]. Bentzen [126] noted that the value of the spatial resolution obtained in this manner relates to the edge response function (ERF).

Geometrical symmetry and other investigations [127] suggest that the worst spatial resolution in time-resolved TI occurs at the mid-plane of the medium (cf. Fig. 1.4). Therefore this is where the spatial resolution is evaluated.

A number of analytic approximations and models have been published calculating the transmitted pulse and associated spatial resolution of fast TI. To a first approximation, the spatial resolution Δx and the gating-time Δt (over which period the signal is integrated) are related according to $\Delta x \propto \Delta t^{1/2}$ when various models such as the path integral [82], random walk [79] and diffusion approximation [51] are used. Furthermore, Hee *et al* [117] demonstrated that the normalised resolution, $\Delta x/L_z$, falls between the worst case geometric limit $(2c\Delta t/L_z)^{1/2}$ [128] and a linear degradation, $c\Delta t/L_z$, where c is the speed of light in the medium and L_z is the medium thickness. Second order approximations to the random walk model have been suggested using scaling arguments [129]. Existing theoretical models are still inadequate when short detection times and spatial boundary conditions are imposed. In order to overcome some of these problems, approximate techniques such as multiple images [55] and extended boundary conditions [130] have been applied. However, the results of these techniques lack accuracy in the short time scales.

Hebden *et al* [122, 123] (also Hebden and Gandjbakhche [118]) have conducted experiments on time-resolved TI using an aqueous suspension of latex micro-spheres as a medium and a streak camera as a detector. They have evaluated the spatial resolution as a function of both gating time and medium thickness in a series of reports. Hebden *et al* [122] used the diffusion theory (Patterson *et al* [55]) to extrapolate their experimental results to the shorter gating times. Several other experimental techniques have been applied to measure the spatial resolution of time-resolved TI such as those of Cia *et al* (1999), Grosenick *et al* [19] and de Haller *et al* [107].

A rapid decrease in the number of transmitted photons as the integration time decreases, leads to statistical uncertainty in the experimental results for the time range below $200ps$. This effect becomes more marked as the tissue thickness is increased. The IMC technique is applied in this paper to accurately evaluate the spatial resolution (in the mid-plane) theoretically achievable for times of flight less than $\sim 200ps$. A simple and accurate theoretical fit to the edge response function (ERF) is proposed from which the spatial resolution is then determined.

4.2 System description

The simulation geometry was an homogeneous, tissue equivalent medium of dimensions $15 \times 10 \times 5.1cm$ that matched the experimental configuration of Hebden *et al* [122]. The set up geometry is similar to that shown in Fig. 1.4 without the presence of the spherical inhomogeneity at the centre.

The results reported here are for a medium thickness of $L_z = 5.1cm$, refractive index, $n = 1.33$ and $\mu_a = 0.1cm^{-1}$. Values of μ_s' of $2cm^{-1}$ ($\mu_s = 28.6cm^{-1}$, $g = 0.93$) and $8cm^{-1}$ ($\mu_s = 98cm^{-1}$, $g = 0.918$) were used to facilitate validation by comparing the results with the experimental results of Hebden *et al* [122, 123] respectively for the two values of μ_s'. The effect of exponential absorption in the medium was included after the MC simulation by considering the final path-length of individual trajectories, as described in section 2.2.

4.3 Method

From their time-resolved optical imaging experiments, Hebden *et al* and also Sassaroli *et al* evaluated the spatial resolution using a method proposed by Bentzen [126] which is based on an estimate of the line spread function (LSF). The LSF is related to the ERF [124] which Hebden *et al* measured experimentally. Here a similar but more direct and simple approach is taken to evaluate the spatial resolution from the LSF.

From the results of the IMC technique, the ERF is obtained from the distribution of

the trajectories as they cross the mid-plane (normal to the propagation axis). The simulation provides the minimum and maximum radial offset positions of the trajectories from the propagation axis. From this spatial information and the temporal constraint, an ERF was obtained for each gating time Δt in increments of $5ps$. Each ERF was obtained by moving a completely absorbing knife-edge along the mid-plane and measuring the integrated detected intensity profile due to only the trajectories whose flight times fell within Δt. In obtaining the ERF for each gating time, the trajectories with equal flight times (within $1ps$) were assigned a mean weight. This reflects the fact that an exact solution of the radiative transport equation (RTE) [12] would yield a *definite* value of the intensity at a point (detector) as a function of flight time given a specified set of medium characteristics.

4.3.1 Full construction of the TPSF

The IMC algorithm was used to produce the data required for the evaluation of the spatial resolution. To avoid the effect of the attractive point on the directions of the photons as they encounter the boundary where both transmission and internal reflection occur, the IMC was not implemented when the trajectories were within a *transport* scattering length from the boundaries.

Chen and Bai [74] pointed out that large attractive factors introduce distortion at the later part of the TPSF, with the start of the distortion being related to the magnitude of the attractive factor. The distortion causes the calculated curve to fall below the correct TPSF. Too small an attractive factor however reduces the efficiency of the simulation. Calculation of the TPSF with a given attractive factor is only accurate over a limited range, determined by the statistical fluctuations at early times and distortion at the later times. This restricted range of validity also flows on to the IMC technique when the CMC technique is used to generate the initial trajectories. Therefore, to accurately construct the TPSF over the wider range, upto $800ps$, separate segments of the temporal profile were produced with increasing attractive factors and were later combined as follows. The TPSFs were calculated using attractive factors in the range 0.3-16.0. Starting with the TPSF associated with an attractive factor of 0.3,

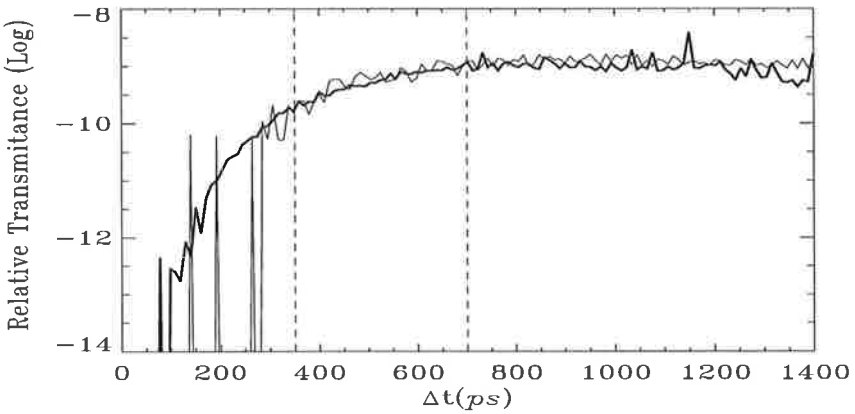

Figure 4.1: A comparison of the temporal point spread functions calculated by the SMC simulation (thin noisy curve) and IMC simulation (thick curve) with attractive factor = 0.4 and $\mu_s' = 5cm^{-1}$. The region between the dotted lines is where both simulations may be compared to within 5% standard deviation.

the standard deviations for $50ps$ time intervals were obtained by comparing the data with a smooth fit to similar data with a higher attractive factor (see Fig. 4.1), using a Gaussian-quadratic method of curve fit [131]. The upper end of a segment was limited by a deviation of 5% from the curve fit. It was necessary to decrease the initial $50ps$ time intervals over which the standard deviations were calculated as higher attractive factors were approached to match the standard deviations. The lower end was chosen where the TPSF with a higher attractive factor began to fluctuate by more than 5% from the smooth curve. The location of this boundary was not critical due to coverage of the region by the TPSF of the lower attractive factor over the overlapping region.

The TPSF obtained from a standard Monte Carlo simulation (i.e., "*deterministic*" with attractive factor of 0), together with the IMC results are shown in Fig. 4.1. The dotted vertical line on the left marks the lower limit in the time scale below which the SMC simulation did not yield statistically significant results within the allowed simulation time. The dotted line on the right marks the upper limit beyond which time the IMC technique is not valid due to distortion.

Finally, these acceptable segments were superimposed and averaged where they overlapped, to yield the complete TPSF as shown in Fig. 4.2. The extension of the TPSF to a time scale, as small as $10ps$, is noted in this figure which is due to highest

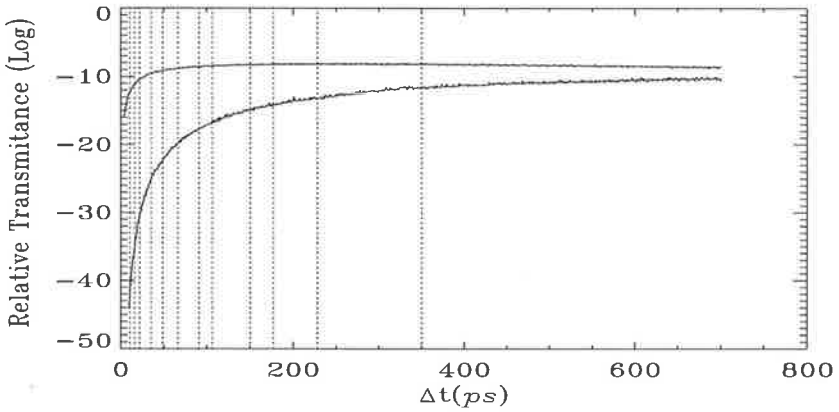

Figure 4.2: Temporal point spread functions (TPSF) through a slab of thickness of $L_z = 5.1cm$ with $\mu_s' = 2cm^{-1}$ (upper curve) and $\mu_s' = 8cm^{-1}$ (lower curve).

attractive factors.

4.3.2 Calculation of image spatial resolution

The image spatial resolution, Δx, defined by the value corresponding to a 10% response on the MTF, is obtained from the point spread function[1](PSF) [124, 127] evaluated at the mid-plane, $z = L_z/2$, where maximum spread of the beam occurs, with z being the propagation axis. For an homogeneous medium and a pencil beam described by a δ-function in space and time, the PSF can be approximated by a 2-dimensional Gaussian distribution [79], expressed in terms of a single radial variable, r. For a point source located at the origin, the PSF is described by:

$$P(r) = \frac{C_0}{2\pi\sigma} e^{-\frac{r^2}{2\sigma^2}}, \tag{4.1}$$

where C_0 is a constant. The LSF can then be expressed [124] as,

$$L(x) = \int_x^\infty P(r)(r^2 - x^2)^{\frac{1}{2}} r dr = \frac{C}{\sqrt{2\pi}\sigma} e^{-\frac{x^2}{2\sigma^2}}, \tag{4.2}$$

with a constant C. For a linear system the ERF is then found to be

$$E(x) = \int_{-x}^\infty L(x')dx' = \frac{C}{2}[\frac{2}{\sqrt{2\pi}\sigma} \int_0^x e^{-\frac{x'^2}{2\sigma^2}} dx' + 1]. \tag{4.3}$$

[1]The (spatial) PSF should not be mistaken with TPSF.

With a change of variable, $\xi = x'/\sqrt{2}\sigma$ and the identification of the error function one finds

$$E(x) = \frac{C}{2}[erf(\frac{x}{\sqrt{2}\sigma}) + 1]. \tag{4.4}$$

Bentzen [126] noted a similar expression to Eqn. 4.3, $E(x) = C_1 f(\frac{x}{\sigma}) + C_2$, where $C_{1,2}$ are constants and $f(x) = \int_x^\infty e^{-x'^2/2} dx'$. However, they approximated $f(x)$, using an inverse polynomial rather than an exact analytic form.

To enable comparison with the experiments the spatial resolution Δx as defined equates to:

$$\Delta x \approx 2.93\sigma. \tag{4.5}$$

However, Eqn. 4.4 suggests that the ERF from either experiment or MC simulations may be fitted with an analytic expression using the error function with a varying parameter, σ. A least squares fit by Eqn. 4.4 was made to the simulated ERF by varying σ. Using this best fit value for σ, the spatial resolution was evaluated as a function of Δt from Eqn. 4.5.

Figure 4.3 shows the normalised ERFs obtained from the IMC simulation and the theoretical fit given by Eqn. 4.4 for the case of $\mu_s' = 2cm^{-1}$. The results shown correspond to gating times, Δt, of 10, 150 and 750 picoseconds and illustrate the sharpening of the ERF and hence improvement in the spatial resolution as the gating time is reduced.

The spatial resolutions as a function of gating time for the cases $\mu_s' = 2cm^{-1}$ and $\mu_s' = 8cm^{-1}$ are presented in Fig. 4.4 and Table 4.1. For comparison, experimental measurements obtained by Hebden [122, 123] and theoretical curves calculated from random walk theory [79], also Hebden and Gandjbakhche [118] and random walk with scaling considerations [129] are also shown. The experimental results of Hebden *et al* [122] ($\mu_s' = 8cm^{-1}$) and Hebden [123] ($\mu_s' = 2cm^{-1}$) correspond to an incident laser beam of less than $1mm$ in diameter and a wavelength of $790nm$ and $600nm$ respectively.

The errors in the calculation of the spatial resolution from the IMC technique as presented in Table 4.1 incorporate the following:

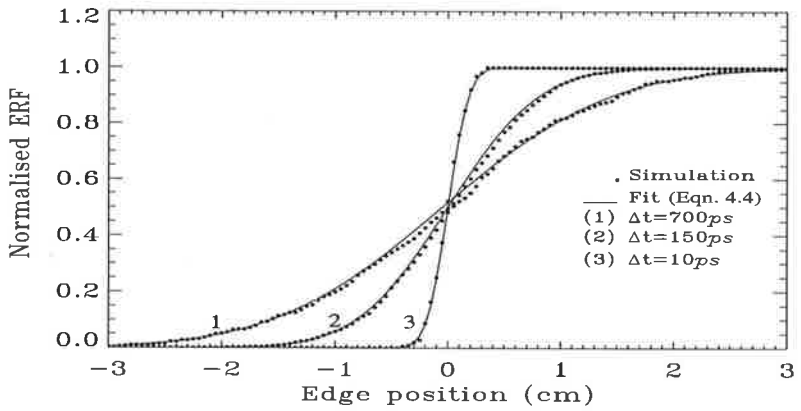

Figure 4.3: Edge response functions (ERF) for gating times of $750ps(1)$, $150ps(2)$ and $10ps(3)$ evaluated from the data presented in Fig. 4.2 (dotted curve) as obtained from both spatial and temporal information provided by the IMC simulation for $\mu_s' = 2cm^{-1}$. The theoretical fit (solid curve) represents the ERF as evaluated by Eqn. 4.4.

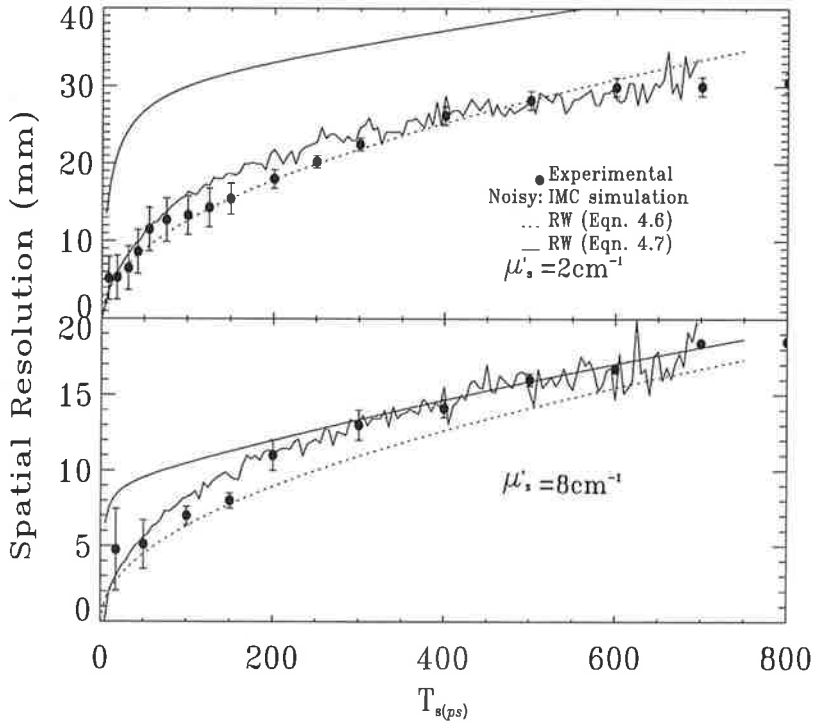

Figure 4.4: The spatial resolution obtained for the IMC simulations with $\mu_s' = 2cm^{-1}$ (top, noisy curve) and $\mu_s' = 8cm^{-1}$ (bottom, noisy curve). The experimental data ($\diamond$): Hebden [123] ($\mu_s' = 2cm^{-1}$) and Hebden *et al* [122] ($\mu_s' = 8cm^{-1}$) along with the theoretical results from the random walk theory: [79], also Hebden and Gandjbakhche [118] (dotted curves representing Eqn. 4.6) and random walk with scaling [129] (solid curves representing Eqn. 4.7) are also presented.

$\Delta t(ps)$	Spatial resolution ($\pm$ error)(mm)			
	$\mu_s' = 2cm^{-1}$		$\mu_s' = 8cm^{-1}$	
	IMC	Exp.	IMC	Exp.
10	$4.3\pm < 0.5$	5.2 ± 2.8	$2.2\pm \sim 1.0$	–
20	$6.0\pm < 0.5$	5.3 ± 2.8	$3.5\pm < 0.5$	4.8 ± 2.7
30	$8.2\pm < 0.5$	6.5 ± 2.8	$4.2\pm < 0.5$	–
40	$9.5\pm < 0.5$	8.6 ± 2.8	$4.9\pm < 0.5$	–
50	11.2 ± 0.5	11.2 ± 2.8	$5.7\pm < 0.5$	5.1 ± 1.6
100	15.8 ± 0.6	13.3 ± 2.5	8.1 ± 0.5	7.0 ± 0.6
150	18.5 ± 0.8	15.5 ± 2.0	9.7 ± 0.7	8.0 ± 0.5
200	20.3 ± 1.0	18.0 ± 1.2	11.0 ± 0.6	11.0 ± 1.0
300	23.7 ± 1.5	22.5 ± 0.8	13.1 ± 1.0	13.0 ± 1.0
400	26.3 ± 1.6	26.2 ± 1.2	14.6 ± 1.2	14.1 ± 0.6
500	28.2 ± 1.5	28.2 ± 1.2	15.8 ± 1.6	16.0 ± 0.4
600	29.6 ± 2.3	29.5 ± 1.2	16.7 ± 2.2	16.7 ± 0.3
650	30.1 ± 2.7	29.7 ± 1.2	17.1 ± 2.1	17.3 ± 0.3

Table 4.1: Spatial resolution and precision as shown in Fig. 4.4 compared with the experimental data of Hebden [123] ($\mu_s' = 2cm^{-1}$) and Hebden *et al* [122] ($\mu_s' = 8cm^{-1}$).

- The uncertainty in the value of σ when the theoretical fit to the ERF was determined.
- Multiple passes of photon trajectories through the mid-plane, particularly those associated with longer flight times ($\gtrsim 200ps$). The maximum axial distance in this plane produces the worse resolution while the minimum yields better resolution. The average was taken.
- The variation in the weights of the trajectories with equal times of flight (within $1ps$). To estimate the influence of this factor, the spatial resolution was evaluated by allowing the trajectory weights to vary within one standard deviation of the mean.

4.4 Discussion

The results of Fig. 4.4 and Table 4.1 demonstrate that the IMC technique yields a good fit to the data of Hebden *et al* [122, 123] and thereby imply the accuracy of

the temporal and spatial distribution of photon trajectories with times of flight ($\lesssim$ $400ps$) for which the technique is most efficient. The apparent disagreement with the experimental results between 100-$300ps$ for the case of $\mu_s' = 2cm^{-1}$ may be related to an unexplained experimental effect acknowledged by Hebden ([123], figure 6) as warranting further investigation. Based on this comparison, it can also be inferred that the IMC technique provides accurate information about the TPSF as presented in Fig. 4.2. The experimental results by Hebden *et al* are assumed to determine the spatial resolution accurately for time scales of greater than 200 and $400ps$ for $\mu_s' = 2cm^{-1}$ and $8cm^{-1}$ respectively. Hall *et al* [102] also studied the effect of medium thickness on both the spatial resolution and transmittance. However, the errors in their measurements increase as shorter time scales are approached. These experiments face challenges common to all present time-gated integrating systems: low detection sensitivity and poor SNR. Hebden *et al* [122] and Hall *et al* [102] used diffusion theory to extrapolate their experimental results and this does not have sufficient accuracy. Nevertheless, the experimental data are useful in that they provide a bench mark for validation of the IMC results in the longer timescales($\gtrsim 400ps$).

The theoretical results of random walk theory have also been included in Fig. 4.4 (dotted lines). To a first order approximation, the random walk theory provides a spatial resolution of:

$$\Delta x = 1.19\sqrt{\frac{c\Delta t}{\mu_s'}} \tag{4.6}$$

derived from a Gaussian fit to the point spread function [79, 118]. Chernomordik *et al* [132] have also published a depth dependence version of Eqn. 4.6 which reduces to this equation for a depth evaluated at mid-plane. A second order approximation has also been suggested for the random walk results based on scaling relations [129] as:

$$\Delta x = 1.19\left(\frac{c\Delta t}{\mu_s(1-g)\left[1-\frac{g\left(1-g^{\mu_s(1-g)c\Delta t}\right)}{(1-g)^2\mu_s c\Delta t}\right]}\right)^{1/2} \tag{4.7}$$

This formula has been presented by the solid curves in Fig. 4.4. The results here show that the second order approximation is only valid for higher values of transport

coefficient and longer ($\sim ns$) time scales.

The IMC gives rise to better statistics and higher precision in the early part of the TPSF. However, the code is less efficient for smaller attractive factors. The increased noise in the IMC results (cf. Fig. 4.4) above $\sim 400ps$ is due to the decreased detection efficiency as the attractive factor is decreased. For instance, in the case of $\mu_s' = 2cm^{-1}$, the detection efficiency for an attractive factor of 16 is about 0.04 per incident photon per picosecond time interval, whereas the corresponding efficiency for a factor of 0.3 is approximately 10^{-6}. Therefore the number of simulated photons must be increased to maintain the quality of the signal over the entire timescale.

The results of Fig. 4.4 and Table 4.1 show that the spatial resolution continues to improve as the photon flight times are restricted to times shorter than a few 10s of picoseconds. For an integration time of $10ps$, the resolution obtained was $\sim 2mm$ with transport coefficient $\mu_s' = 8cm^{-1}$ for a medium of thickness $L_z = 5.1cm$. Although the simulated incident beam is described by a δ-function in time and space, in practice the spatial resolution will be influenced by the spatial and temporal profile of the incident beam. The detector size used in the simulations is comparable with the resolution obtained and the outcome is a convolution of the ideal resolution with the detector. Joblin [133] has extensively explored the effect of the system size and the results may be applied here. At present, SNR may make it difficult to achieve these limits experimentally with conventional integrating detectors. However, multiple sampling techniques can give improved signal to noise ratios.

It is further noted from Fig. 4.4 that better spatial resolution can be achieved when scattering coefficient is higher. This is because, for higher a scattering coefficient and a given transit time, the detection probability of a trajectory which deviates from the direct line-of-sight becomes smaller.

Figure 4.5 shows the effect of the absorption in the medium on the TPSF and the spatial resolution in the case of $\mu_s' = 2cm^{-1}$. These results are consistent with the findings of simulations performed by Hebden and Kruger [127] who suggested that an increased absorption improves the spatial resolution for a given integration time. This can be explained as follows. As the probability of absorption increases, the trajectory

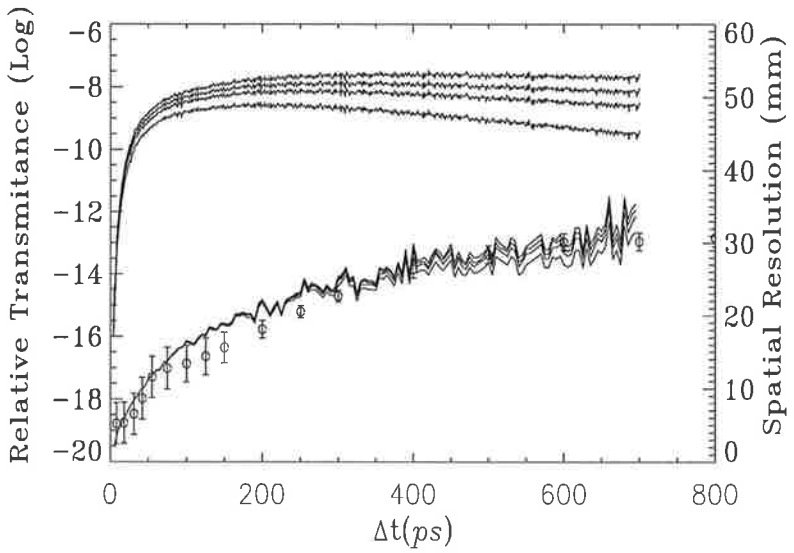

Figure 4.5: The lower set of curves show the spatial resolution (right scale) obtained for the IMC simulations with $\mu_s' = 2cm^{-1}$ and with varying absorption coefficient, $\mu_a = 0.0$, 0.05, 0.10 and 0.20 from top to bottom, again including for comparison, the experimental results of Hebden [123]. The top set of curves represents the effect of respective absorption coefficients on the TPSF (left scale).

weight decreases exponentially depending on the absorption coefficient. Longer flight paths therefore carry less weight as the absorption coefficient increases. Therefore a gated detector for a fixed gating time would, statistically, count a smaller number of long trajectories and more of the shorter ones leading to an improved spatial resolution. The improved spatial resolution as the absorption increases, is achieved at the cost of a decrease in the detected signal. The figure also shows the spatial resolution is not significantly affected by the absorption for short gating times. This suggests that the resolution performance of TI is improved for smaller values of the absorption coefficient as this enhances the detected signal without compromising the resolution.

4.5 Conclusion

The indeterministic Monte Carlo (IMC) simulation technique was used to evaluate the spatial resolution (at the mid-plane of a turbid medium) achievable with integrating time-resolved TI in the sub-100 picoseconds range. The calculation shows that a spatial resolution of about $2mm$ is theoretically achievable for an optically thick medium ($\sim 5cm$). To obtain this result, the TPSF was fully constructed and an edge response function (ERF) was estimated. The results are in agreement with the published experimental data for longer times of flight. An increased absorption within the range of interest has a minimal effect on the spatial resolution but would significantly affect SNR. The results obtained with this technique correspond more closely with the experimental data than the published analytical results. The MC technique also has the flexibility to readily incorporate inhomogeneities within the turbid medium.

Chapter 5

First photon detection (FPD)

5.1 Motivation

In this chapter, a limiting case of time-resolved TI systems, *first* photon detection (FPD), is studied by considering the first detected photons from a sequence of incident laser pulses. The spatial and temporal specifications of the system were described in section 1.6 with Figs. 1.4 and 1.5 showing schematic diagrams of the spatial and temporal characteristics of the system. At each scan position, $\sim 10^3$ laser pulses of $< 1ps$ in width and with $\sim$ 1MHz repetition rate are made incident onto the surface of the turbid medium. The first arriving photon from each pulse is detected. The recorded arrival times of the first detected photons then form the temporal distribution for the first arriving photon for each scan position.

Assuming an ideal single photon detector, an analytic method of deriving the temporal probability density functions (p.d.f.) for the first arriving photon from the TPSF is presented. The potential performance of the FPD system is evaluated through MC simulation. Initially, an ideal detector capable of detecting the first arriving photon with 100% efficiency is assumed. With this ideal detector, the FPD technique is then applied to obtain the first photon p.d.f. for different laser pulse intensities incident on an homogeneous medium. The variation in the mean arrival time of the the first detected photon is then assessed as a function of the thickness, absorption and scatter coefficients of the medium and introduced inhomogeneities. The technique is also

applicable to the derivation of the p.d.f. of the second and later arriving photons, enabling a detection time limit to be specified to eliminate the later arriving photons and thereby overcome distortions of the first photon p.d.f. caused by any inefficiency of the single first photon detectors.

5.2 Theory: Statistics of the first arriving photon

Let N_0 be the number of photons in an incident pulse and let N be the total number of detected photons arriving at *any* time within $[0, \infty)$ with the TPSF represented by $T(t)$. The flight time t is calculated relative to the minimum flight time of the ballistic photon, L_z/c, and hence represents the delay time of each photon trajectory. This implies:

$$\int_0^\infty T(t)\, dt = N. \tag{5.1}$$

On normalization to one photon per incident pulse, i.e., when $N_0 \to 1$, T(t) becomes $f(t) = T(t)/N_0$ which is the *probability density function* (p.d.f) for the detection of *any* single incident photon with the corresponding *cumulative (probability) distribution function* (c.d.f.) $F(t)$. One then writes:

$$\int_0^\infty f(t)\, dt = N/N_0. \tag{5.2}$$

Now, let t_d be the gating time of the detector integrating from $t = 0$. The number of detected photons $N(t_d)$ within $[0, t_d]$ is not fixed from one incident pulse to the other. This is due to the stochastic nature of the process dictated by the turbid properties of the medium. However, the average number of detected photons $\overline{N(t_d)}$ within $[0, t_d]$, approaches the *expectation value* (or average) of the detected photons, $\langle N(t_d) \rangle$ within $[0, t_d]$, given by:

$$\langle N(t_d) \rangle = \frac{\int_0^\infty N(t_d) f(t)\, dt}{\int_0^\infty f(t) dt} = \int_0^{t_d} T(t)\, dt; \tag{5.3}$$

This is simply denoted by N_d. The second equality follows from the definition of the TPSF. One may then say that, for every gating time t_d there corresponds a positive number $N_d \leqslant N$ such that the expectation value of the detected number of photons within $[0, t_d)$ is N_d. One also notes that for any $t'_d \leqslant t_d$, it is found that $N'_d \leqslant N_d$, which is a restatement of the requirement that the c.d.f. be piecewise-continuous, monotonically increasing [135]. By induction, this argument can be extended down to $N_d = 1$ and a corresponding time t_1 for which

$$N_d = \int_0^{t_1} T(t)dt = 1. \tag{5.4}$$

It then follows that for times $t'_1 = t_1 \pm \delta t$, on average, less $(-)$ or more $(+)$ than one photon is *expected* to be detected within $[0, t'_1)$. It is clear that when a finite number of pulses is incident, not always exactly one photon is detected within $[0, t_1)$. The probability of detecting one photon within $[0, t_1)$ is evaluated by knowing the p.d.f $f_1(t)$ for the **first** arriving photon. This follows because *one* photon being detected within $[0, t_d]$ implies that it is the first photon.

In deriving $f_1(t)$, let p be the probability that the first photon arrives within $[0, t_1)$. Then the probability of the first photon *not* arriving within that time would be $q = 1-p$. The value of q can be evaluated as follows: let q' be the probability that *any* single photon arrives within $[t_1, \infty)$, i.e., not before t_1, and hence is determined by:

$$q' = \frac{\int_{t_1}^{\infty} f(t)dt}{\int_0^{\infty} f(t)\,dt} = \frac{N_0}{N}\int_{t_1}^{\infty} f(t)\,dt. \tag{5.5}$$

Assume that the arrival time of each photon is an *independent* event (i.e., no photon-photon interactions) then q is equivalent to the probability of *all* N photons arriving after t_1. Therefore $q = q'^N$, and hence the probability of the first photon arriving within $[0, t_1)$ is

$$p = 1 - q'^N = 1 - \left[\frac{N_0}{N}\int_{t_1}^{\infty} f(t)\,dt\right]^N. \tag{5.6}$$

It is noted [135] that p has the characteristics of a c.d.f.. The c.d.f., $F_1(t)$, for the arrival time of the first detected photon is therefore given as:

$$F_1(t) = 1 - \left[\frac{N_0}{N}\int_t^{\infty} f(t')\,dt'\right]^N, \tag{5.7}$$

and the p.d.f. for the first arriving photon, $f_1(t)$, normalised to unity, is given by:

$$f_1(t) = \frac{d}{dt} F_1(t). \tag{5.8}$$

Substitution of Eqn. 5.7 in Eqn. 5.8 and using Eqn. 5.2 yields:

$$\begin{aligned} f_1(t) &= -N_0 \left[\frac{N_0}{N} \int_t^\infty f(t')\, dt' \right]^{N-1} \frac{d}{dt} \left(\frac{N_0}{N} - \int_0^t f(t')\, dt' \right) \\ &= \left[\frac{N_0}{N} \int_t^\infty f(t')\, dt' \right]^{N-1} N_0 f(t) \\ &= \left[\frac{\int_t^\infty T(t')\, dt'}{N} \right]^{N-1} T(t) \\ &= a\, T(t), \end{aligned} \tag{5.9}$$

with $a \approx \left[\frac{\int_t^\infty T(t')\, dt'}{N} \right]^N$ for large N. The numerator in a integrates the tail end of the TPSF from t onwards. When t is small ($t \longrightarrow 0$),

$$a = \left(\frac{N}{N} \right)^N = 1,$$

as $\int_0^\infty T(t)dt = N$. This implies $f_1(t)$ is close to (or is equal to) the TPSF, $T(t)$ for t near 0. For larger t values than zero $\int_t^\infty T(t')dt' < N$ (total possible detected photons), and hence:

$$\frac{\int_t^\infty T(t')dt'}{N} < 1,$$

which implies

$$a = \left(\frac{\int_t^\infty T(t')dt'}{N} \right)^N \longrightarrow 0,$$

and this makes $f_1(t)$ drop to zero as t increases. This has been demonstrated in Fig. 5.12.

The above formulation shows that, given N_0 and T(t), one is able to derive the c.d.f. and hence p.d.f. for the first arriving photon of an incident pulse. Given that the pulses within a sequence are equivalent within statistical variations, the p.d.f so obtained describes the temporal distribution of the first detected photon from each pulse. An FPD system, as previously described in section 1.6 would produce the density function given by Eqn. 5.9.

5.3 Monte Carlo (MC) simulation

As indicated by Eqns. 5.7 and 5.9, a full construction of the TPSF is necessary both to evaluate N and also to determine the TPSF in the early time scale which most contributes to $f_1(t)$. In this study, the normalised TPSF, $f(t)$, was obtained through the IMC simulation technique.

With a reference to the possible FPD system configuration outlined in section 1.6, the simulation modelled a collinear source-detector combination positioned on opposite sides of an homogeneous medium representing the normal tissue. For the simulation, while constant values of 1.45 and 0.95 were adopted for n and g respectively, the values attributed to the thickness L_z, the absorption and scatter coefficient, μ_a and μ_s, were varied as per simulations outlined below. However, the values were consistent with typical values for breast tissue [8, 24]. The detector active collection area corresponds to a disk of $0.5mm$ in radius. However, to reduce the computation time, the detection efficiency was increased by doubling the detector radius when simulating segments for the later ($> 800ps$) portion of the TPSF. A (detection) area correction was then applied to the final photon weights by a multiplication factor of 0.25. The accuracy of this method was verified by examination of the transmittance profile across the exit surface near the detector. Figure 5.1 shows the results. These confirms that the physical situation is that the late-arriving (**diffused**) photons have an approximately uniform fluence over the exit surface near the detector. Moreover, it was found that the discrepancy in the total number of detected photons, N, was less than 1.5% after the correction. Since the late part of the TPSF only influences N, this method of increased detection area for longer time scales was considered valid. A 3-point median filter was also applied to the TPSF for smoothing before $F_1(t)$ and $f_1(t)$ were evaluated as represented by Eqns. 5.7 and 5.9 respectively.

The p.d.f. for all detected photons, $f(t)$ (normalised TPSF to one incident photon) and the corresponding c.d.f., $F(t)$, are shown in Fig. 5.2(a) for times of flight up to $3000ps$. Figure 5.2(b) expands the first $200ps$ time scale in which the first arriving photon contributes most to the TPSF and demonstrates that the IMC technique is

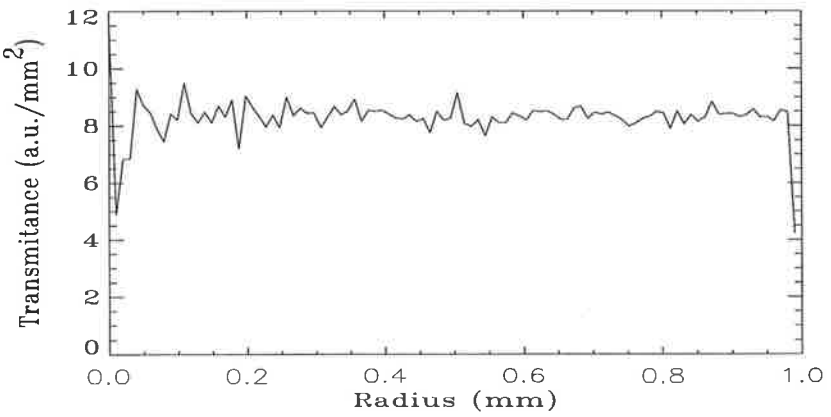

Figure 5.1: The transmittance per unit area at the exit surface near the detector. The reduced noise towards larger radii is due to larger collection areas (rings) associated with a given radius which resulted in improved statistics.

well conditioned at very short times in excess of the ballistic TOF.

For each of the simulations described below, a separate simulation was carried out for each scattering coefficient and medium thickness. The absorption was evaluated as described in section 2.2.

5.4 Number of photons per incident pulse (laser power)

For a given number of photons, N_0, per incident pulse, there is a unique t_1 (up to the statistical variation and measurement tolerance) such that $F_1(t_1) = 1$, i.e., the first photon arrives *almost* definitely within[1] $[0, t_1]$. Now, let $N_0^k (= 10^k N_0,\ k = 1, 2, \cdots)$ represent the number of photons per incident pulse for an increasing sequence of laser powers w.r.t. a reference laser power containing N_0 photons. In an ideal case the linearity of Eqn. 5.1 dictates that the ratio N_0^k/N^k remains constant where N^k is the corresponding total number of detected photons. From Eqn. 5.7, it is evident that the c.d.f. for the first arriving photon approaches unity faster as k increases. This means

[1]More precisely, t_1 is the infimum of a time interval, $[t, \infty]$, for which $F_1(t)$ is sufficiently close to unity within a tolerance limit.

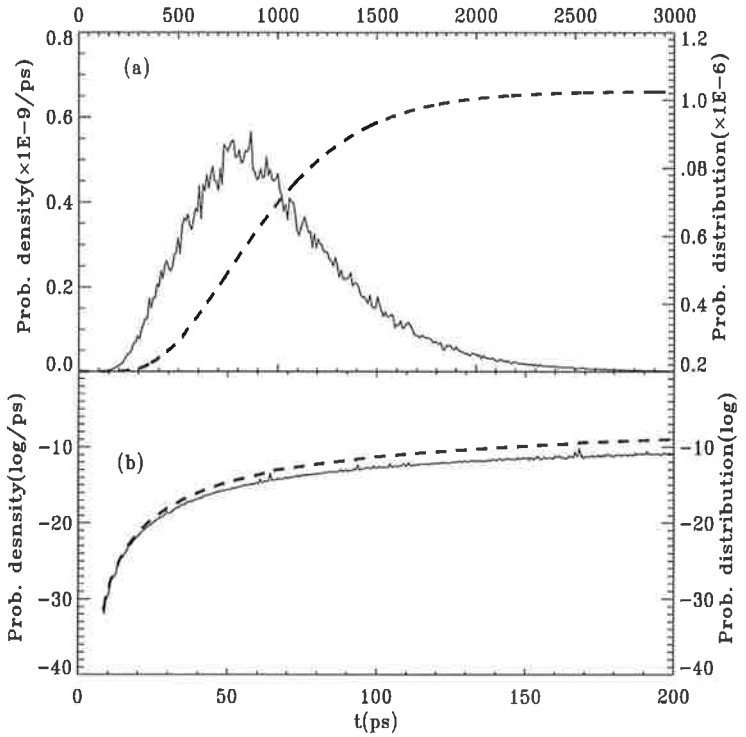

Figure 5.2: (a) The p.d.f. for any detected photon, $f(t)$ (solid curve, normalised TPSF to one incident photon) and the corresponding c.d.f., $F(t)$ (dashed curve, left scale). (b) magnification of the first $200ps$ of the time scale.

that the probability density function integrates to unity within a time interval $[0, t_1^k]$, where $t_1^k < t_1$ is a decreasing sequence. Physically, this reflects the expectation for the first photon to arrive earlier as the laser power is increased. The relationship is however non-linear and depends on the form of the TPSF, a characteristic function of the medium. For example, if the gradient of the TPSF is steep, the points in the sequence t_1^k are closer together.

By varying N_0, the number of photons per pulse, a range of incident laser powers on an homogeneous medium with specific p.d.f., $f(t)$, was simulated. The change in N_0 resulted in a corresponding change in N (Eqn. 5.9) and subsequently in $F_1(t)$ and $f_1(t)$. For a pulsed laser with an average power of $\sim 10mW$, a repetition rate of 1MHz and a wavelength of 1μm, N_0 would be $\sim 10^{11}$ photons per pulse. A repetition rate of 1MHz would avoid any cross talk between pulses as the TPSF typically extends to only a few nanoseconds.

The application of Eqns. 5.7 and 5.9 to the TPSF curves results in the p.d.f. for the transition time of the first arriving photons. Figure 5.3 shows the p.d.f. for different values of laser power N_0 (the smooth curves are Gaussian-quadratic fits to the MC data). The right hand curve of Fig. 5.3 represents $N_0 = 10^{11}$ photons per pulse. N_0 increases by one order of magnitude for each curve towards the shorter time scales, equating to a range of powers from $10mW$-$1MW$. Whilst a megawatt of power is impractical, the curves demonstrate that the p.d.f. for the first arriving photon approaches a delta function at $t = 0$ as the laser power increases infinitely. Therefore, an increase in laser power produces a corresponding decrease in the mean arrival time which implies improved spatial resolution as well as faster response time requirement for the detector. However, for a pulse repetition of 1MHz and detector area of about $1mm^2$, the maximum permissible exposure[2] (MPE) of $15mW$[3] is equivalent to about

[2]This maximum permissible exposure limit has been evaluated according to the Australian and New Zealand laser standards [136].

[3]The MPE due to a single pulse within a *train* is calculated via, $\text{MPE}_{train}=\text{MPE}_{single} \times C_1$ where $C_1 = N^{-0.25}$ is the correction factor and N is the number of pulses in the train. $\text{MPE}_{single} = 5 \times 10^6 \times C_2 \times C_3 \times C_4$ where $C_2 \sim 3$, $C_2 \sim 1$ for $\lambda \sim 1\mu m$ and C_4 is the proportion of the total integral sum of the pulse widths and the exposure time.

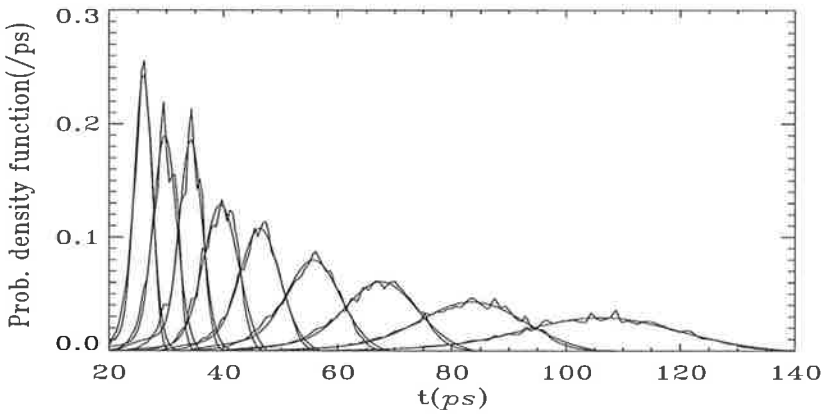

Figure 5.3: The first arriving photon p.d.f., $f_1(t)$ for a range of laser powers. The curves represent different input laser intensities from 10^{11} photons per pulse (RHS) to 10^{19} (LHS). The smooth curves are fits to the data.

10^{11} photons per incident pulse.

A limiting case: When N_0 is large (high laser power) or when the medium is thin, giving rise to a very large number detected photons N, Eqn. 5.7 characterises an important physical phenomenon, namely a sharp increase in the probability of the detection of ***a number*** of (first) photons immediately after the ballistic flight time. This can be seen by noting that $\left[\int_t^\infty f(t')\,dt'\right]^N < 1$ and hence $\lim_{N\to\infty}\left[\int_t^\infty f(t')\,dt'\right]^N = 0$ and, in the limit when $N \to \infty$ it follows that:

$$F_1(t)\begin{cases} = 1 & \text{for } t > 0 \\ = 0 & \text{for } t = 0 \end{cases},$$

which forces $f_1(t)$ to approach a δ-function.

5.5 Medium thickness and optical properties

The TPSF and subsequent $f_1(t)$ were evaluated under conditions of changes in the medium thickness, L_z. Media with three values of L_z = 4.0, 5.0 and 6.0cm were simulated. Simulations were carried with constant absorption and transport coefficients of $\mu_a = 0.1cm^{-1}$ and $\mu_s' = 5cm^{-1}$.

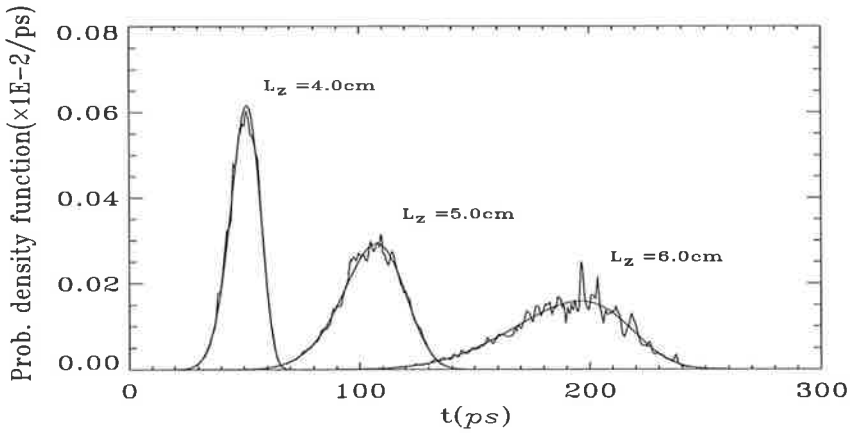

Figure 5.4: The variation in the first photon p.d.f. versus thickness of the homogeneous medium.

The decrease in the thickness of the medium results in a decrease in the (mean) arrival time of the first photon as shown in Fig. 5.4. This is not simply due to the reduced path-length, as t represents the delay time w.r.t. the ballistic TOF. This decrease in the arrival time is attributed to the increase in the total detected number of photons, N. As was previously demonstrated a decrease in N results in an increased first photon transit time.

The first photon p.d.f, $f_1(t)$, was also evaluated as the scattering and absorption coefficient of the medium were varied. Simulations with different transport coefficients of μ_s' =5, 8, and $10cm^{-1}$ and fixed absorption ($\mu_a = 0.1cm^{-1}$) were performed as well as with a fixed transport coefficient ($5cm^{-1}$) and variable absorption (0.1, 0.15, 0.2 and $0.25cm^{-1}$).

The results are presented by Figs. 5.5 and 5.6. The shift for an increase of μ_s' from 5.0 to $10.0cm^{-1}$ results in a mean transit time change of approximately $200ps$ whilst an increase in μ_a from 0.1 to $0.25cm^{-1}$ causes a mean transit time shift of approximately $10ps$. An increased absorption results in smaller detection probability and hence a decrease in N. Also, an increase in the scattering coefficient results in a decrease in the reduced mean free path, l', and hence increased optical thickness which in turn implies a reduction in N. These, again supports the prediction of the theory, i.e., increase in the first arriving photon mean transit time as N decreases.

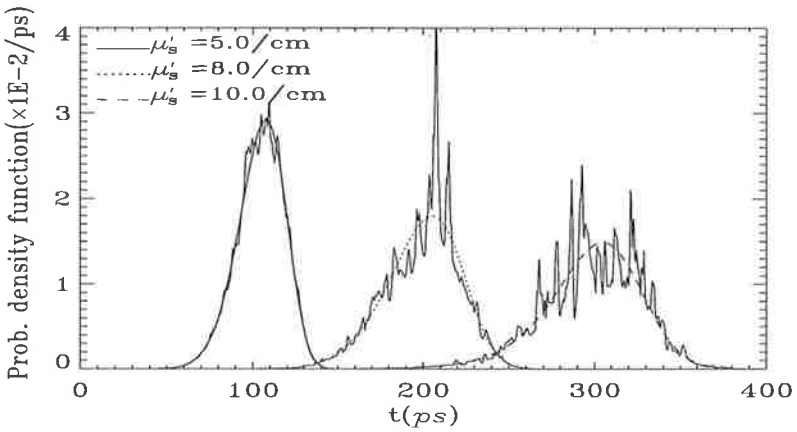

Figure 5.5: This figure shows the the variation in the first photon p.d.f. versus increased transport scattering coefficient of the homogeneous medium.

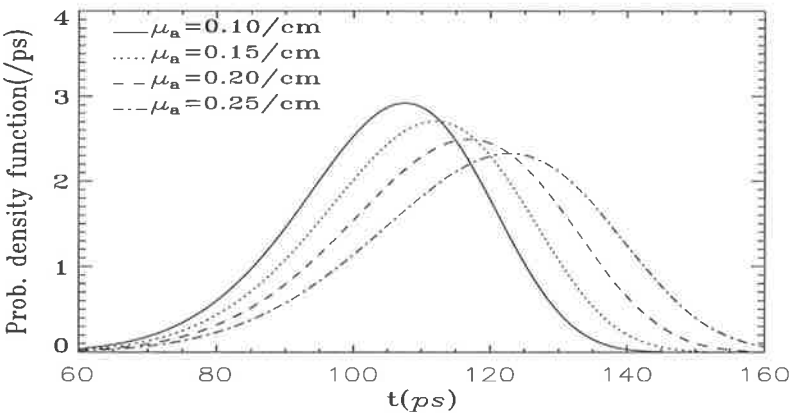

Figure 5.6: The variation in the first photon p.d.f. versus increased absorption coefficient of the homogeneous medium.

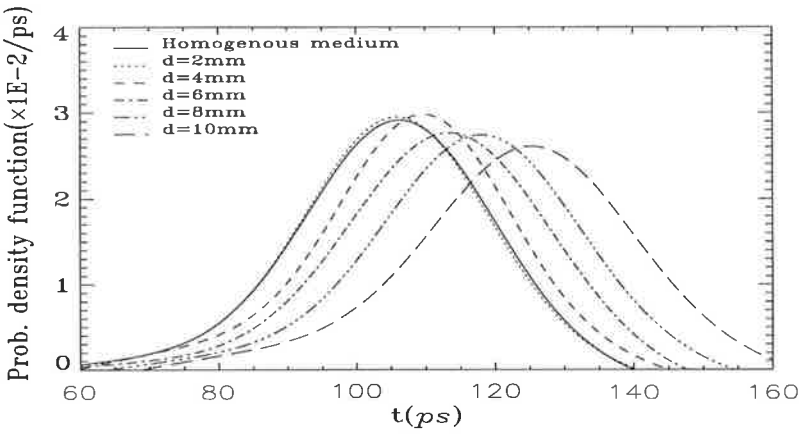

Figure 5.7: The p.d.f.s for the first arriving photon corresponding to the presence of totally absorbing spherical inhomogeneities with varying diameters in an otherwise homogeneous medium. The results are shown for totally absorbing inhomogeneities located at the centre of the medium.

5.6 Introduced inhomogeneities

MC simulations were undertaken to determine the TPSF when a spherical inhomogeneity was introduced at the mid-plane. A separate simulation was computed for each totally absorbing sphere within the diameter range of 2-10mm. Similarly, further simulations were performed with sphere having a fixed diameter (6mm) and constant absorption ($\mu_a = 0.1cm^{-1}$) over a range of transport coefficients ($\mu_s' = 7.5\text{-}2.5cm^{-1}$), as well as one having a fixed transport coefficient ($7.5cm^{-1}$) with the absorption coefficient varying ($0.1\text{-}4.0cm^{-1}$).

The p.d.f. of the first arriving photons with totally absorbing spherical inhomogeneities of increasing diameter, located at the centre of mid-plane, are shown in Fig. 5.7 for an incident pulse of 10^{11} photons. Figure 5.8 plots the increase in the mean arrival, $\bar{t}_1$ time for the p.d.f.s of Fig. 5.7 against the diameter of the inhomogeneity.

The mean arrival time is an average over the flight time of a number of possible (*"snake"*) trajectories which zigzag to the detector, but not necessarily along the geometric shortest path. At each scan position, the first arriving photons from a sequence of incident pulses may be thought of as a photon *cloud* [48] with the leading edge being the ballistic photon (or that which follows the geometric shortest path). The

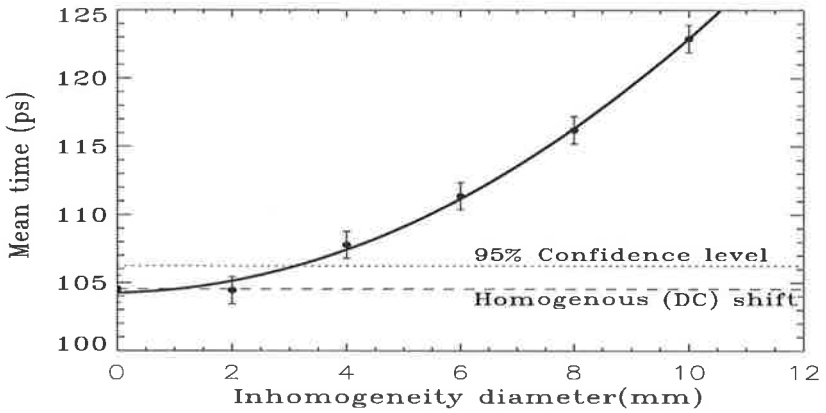

Figure 5.8: Mean (arrival) time of the first photon density function corresponding to spherical inhomogeneities with varying diameters as presented in Fig. 5.7 (•). The solid smooth curve is a parabolic fit to the data.

Diameter(mm)	2.0	3.5	4.0	>4.0
P-value	0.46	0.05	0.001	<0.0001

Table 5.1: P-values corresponding to significance test on the p.d.f.s presented by Fig. 5.7.

remainder consists of photon trajectories within a volume bounded by the source and the detector around the most likely *classical* path as described by the path integrals of Feynman [80]. The *classical* path is the ballistic trajectory only for the case when the detector is perfectly collimated. For measurements of the early part of the TPSF, it is not practical to utilise such a detector, as this significantly reduces the flux.

A significance T-test was performed on the results of Fig. 5.7 to assess the null hypothesis that the spherical inhomogeneities do **not** have an effect on the first photon p.d.f.. Table 5.1 present the results of the significance test. The P-value corresponding to a 3.5mm inhomogeneity was evaluated by extrapolation using the parabolic fit to the data presented in Fig. 5.8. It is concluded that a totally absorbing spherical inhomogeneity, $3.5mm$ in diameter, is distinguishable from the the uniform medium at the 95% confidence level.

Figures. 5.9 and 5.10 show the shift towards longer transit times due to an increase in the transport scattering ($7.5\text{-}25cm^{-1}$) and absorption ($0.1\text{-}4.0cm^{-1}$) coefficient respectively, of a fixed $6mm$ diameter spherical inhomogeneity. The increase in the mean

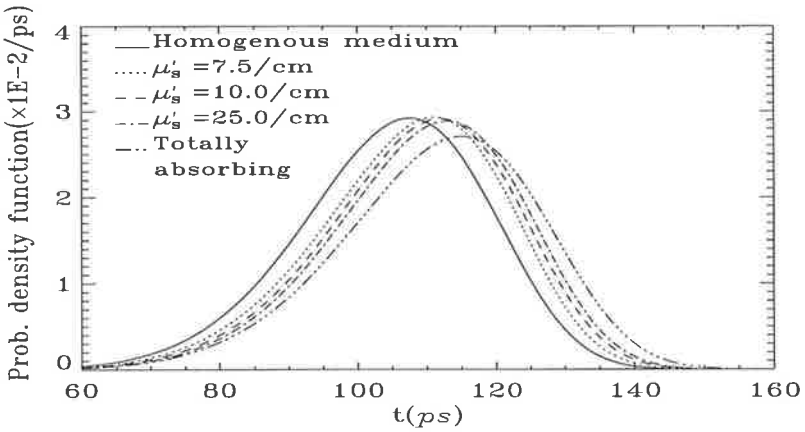

Figure 5.9: The effect of the variation in the transport scattering coefficient μ_s' associated with a $6mm$ in diameter spherical inhomogeneity located at the centre of the medium. The absorption coefficient was fixed at $\mu_a = 0.1cm^{-1}$. The solid curve represents an homogeneous medium with $\mu_a = 0.1cm^{-1}$and $\mu_s' = 5cm^{-1}$.

arrival time highlighted by these figures reflects an increase in the effective path-length due to either more scattering within the spherical medium or to travelling around it. It can be deduced that inhomogeneities with smaller scattering and absorption coefficients than the medium, result in a shift towards the left of the p.d.f. representing the homogeneous medium. As most tumours have higher values of scatter and absorption coefficients [27] than normal tissue, the maximum differential in the TOF is offered by the totally absorbing inhomogeneity.

The results as shown in Figs. 5.9 and 5.10 in combination with those of Fig. 5.8 indicate that solution of the inverse problem (i.e., determining the characteristics of an inhomogeneity from the increase in transit time) may be non-unique. For example, a medium with a $6mm$ spherical inhomogeneity with lower scatter/absorption coefficients than a totally absorbing sphere may result in a shift equal to that of a $4mm$ one with higher values of scattering/absorption coefficients. However, Fig. 5.8 suggests that a shift above a threshold specified by the 95% confidence level guarantees the presence of a spherical inhomogeneity of at least $3.5mm$ in diameter.

The detectability of a specific inhomogeneity within an homogeneous medium is indicated through examination of Figs. 5.5 and 5.6. The shift in the mean transit time, while consistent with those indicated by Figs. 5.9 and 5.10, are of greater magnitude

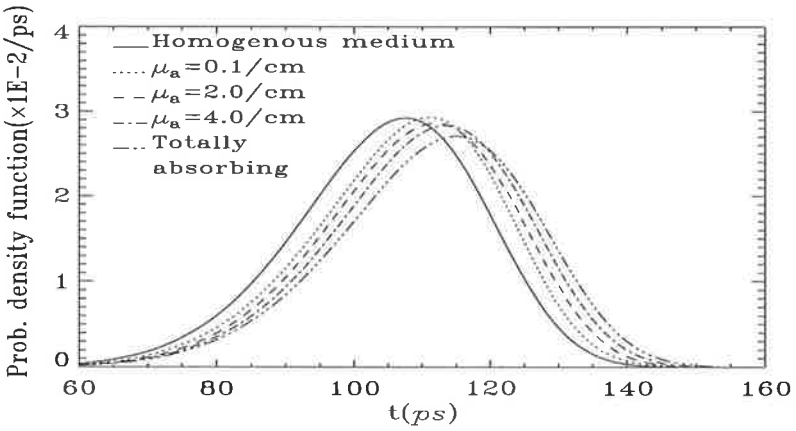

Figure 5.10: This figure is similar to Fig. 5.9 but shows the effect of a varying absorption coefficient μ_a. The transport scattering coefficient of the inhomogeneity was fixed at $\mu_s' = 7.5cm^{-1}$ and the solid curve represent an homogeneous medium with $\mu_a = 0.1cm^{-1}$and $\mu_s' = 5cm^{-1}$.

due to the larger volume occupied by the medium of high scattering coefficients through which the trajectories propagate.

5.7 The effect of a non-ideal detector

A single photon detector is unlikely to be 100% efficient and hence will detect some later arriving photons. Assuming no photon-photon interactions and that the arrival time of each photon is an independent event, the effect of missing the first arriving photon by the detector may be evaluated by removing its contribution to the TPSF. The remaining signal would then have the second photon of the originally detected signal as its first photon. The 2^{nd} photon p.d.f. may therefore be obtained by subtracting $f_1(t)$ from $T(t)$ and applying the above calculations (Eqns. 5.7 and 5.9) to the remaining signal. This technique can be extended to the 3^{rd} and later arriving photons.

For a less than 100% efficient detector, 2^{nd} and later orders of photon may be detected. The p.d.f.s for these later arriving photons, $f_n(t)$, were calculated as described above, from the simulated TPSF of an homogeneous medium with $\mu_s' = 5cm^{-1}$.

A model for the first photon p.d.f. $f_{r_1}(t)$ corresponding to a non-ideal (realistic)

detector[4] may be considered as:

$$f_{r_1}(t) = \sum_{n=1}^{N} \alpha_n \, f_n(t), \tag{5.10}$$

where $\sum_{n=1}^{N} \alpha_n = 1$ with the characteristic efficiency response factors α_n being real positive numbers that characterise the detector efficiency with respect to the detection of the n^{th} arriving photon. The α_n may be a function of several technical factors, consideration of all of which is beyond this theoretical evaluation. It is however noted that high values of α_1 and a fast decreasing sequence of α_n is indicative of an efficient detector.

Figures 5.11 shows the p.d.f.s for the n^{th} arriving photons, while Fig. 5.12 shows the integrated first n arriving photons statistics. The results also present the contribution of the integrated number of first arriving photons to the TPSF. Figure 5.12 also confirms the expected results that the temporal distribution of the integrated first n arriving photons follows the TPSF. Based on the results of Figs. 5.11 and 5.12, a detector with an efficiency of less than 100% will (a) always have a finite and increasing chance of detecting the second or later arriving photons unless the gating time is limited or the first photon is detected within less than $103ps$, and (b) not be able to readily resolve the later orders of arriving photons due to the fast rising TPSF. Without knowing the characteristic efficiency response of the detector, an accurate prediction of the proportions of first, second and third order content of the final measured p.d.f. cannot be made. However, with an upper acceptance limit of $140ps$, photons of the fourth order and above will be eliminated and the relative proportions of the first, second and third order will be, at worst, the relative areas under the curves up to that time limit.

5.8 Conclusion

A method for determining the temporal p.d.f., $f_1(t)$, of the first arriving photon at a detector from laser pulses incident on a turbid medium has been developed. The

[4]The subscript, r in $f_{r_1}(t)$ reflects the first photon p.d.f. output of a realistic (non-ideal) detector.

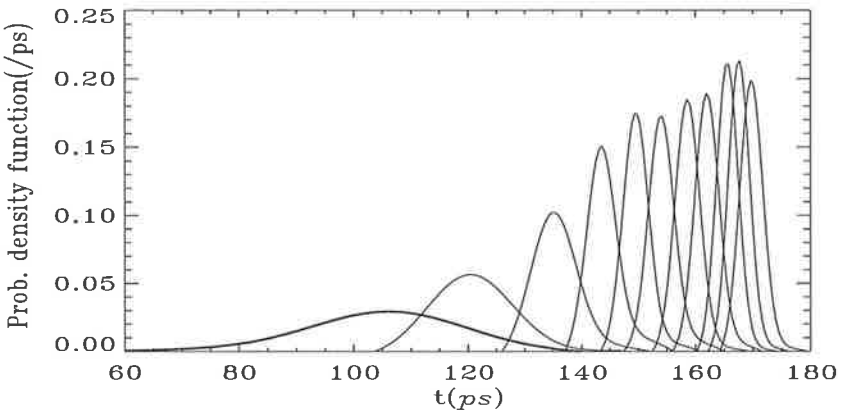

Figure 5.11: The p.d.f. for later (n^{th}) arriving single photons. The same conditions apply as in Fig. 5.3 with a fixed laser power at $10mW$. The first thick curve to the left corresponds to the first arriving photon and only the even orders (thin curves, $n = 2, 4, 6, \cdots, 20$) have been shown for clarity.

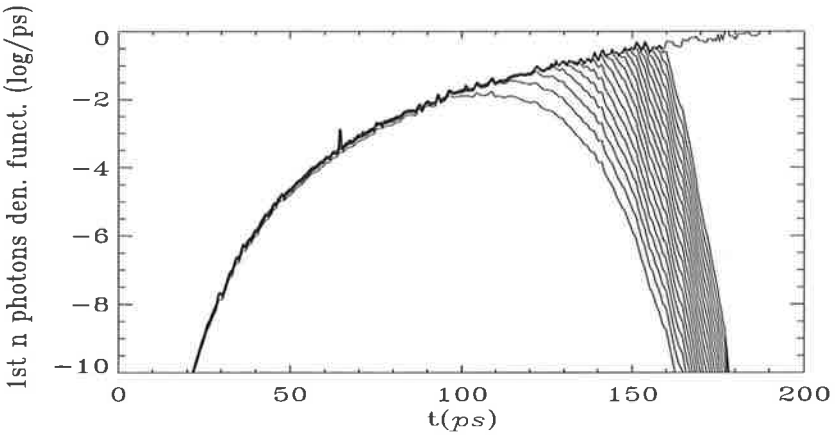

Figure 5.12: Contribution of the temporal distribution of the integrated first n arriving photons to the TPSF. The first thin curve to the left corresponds to the first arriving photon, $f_1(t)$, and those to the right correspond to $n = 2, 3, 4, \cdots$ respectively. The enveloping (continually rising) curve represents the TPSF. A logarithmic scale has been used as the range of amplitudes spans more than two orders of magnitude.

potential information content of $f_1(t)$ and the possibility of its use to form a basis of a first photon detection (FPD) TI system has been theoretically assessed. For a tissue-like medium of about $5cm$ in thickness, the p.d.f. for the first arriving photon of an incident pulse constitutes the sub-150 picosecond portion of the TPSF. Under ideal conditions, a system based on first photon detection can discriminate a totally absorbing sphere of $3.5mm$ in diameter in an homogeneous medium, when a laser power of about $10mW$ at 1MHz repetition rate is utilised. The FPD system also demonstrates significant sensitivity with variations in the optical properties of the homogeneous medium as well as the presence of inhomogeneities.

Chapter 6

Heterogeneous medium

6.1 Motivation

The FPD system described in chapter 5 assumed an homogeneous medium with no spatial variation in its optical properties. Although useful in demonstrating a theoretical basis for FPD, it is an idealised case. In this chapter the effect of heterogeneity in the medium is considered.

A heterogeneous medium is one in which the optical density varies spatially(here, with an emphasis on the scattering coefficient). A $5 \times 5 \times 5cm$ medium was divided into a three dimensional $11 \times 11 \times 11$ array of cubic cells[1]. These cells have a size that approximates the size of the lobules in the breast. Over a number of simulations the cells were assigned random values of scattering coefficients with a mean of $100cm^{-1}$, uniformly distributed between 70-$130cm^{-1}$. For computational efficiency the cells were each assumed to have the same refractive index, $n = 1.45$, and anisotropy, $g = 0.95$.

[1] A choice of an odd number of cells in each dimension avoids the central propagation axis coinciding with the adjoining line of column cells in the propagation direction.

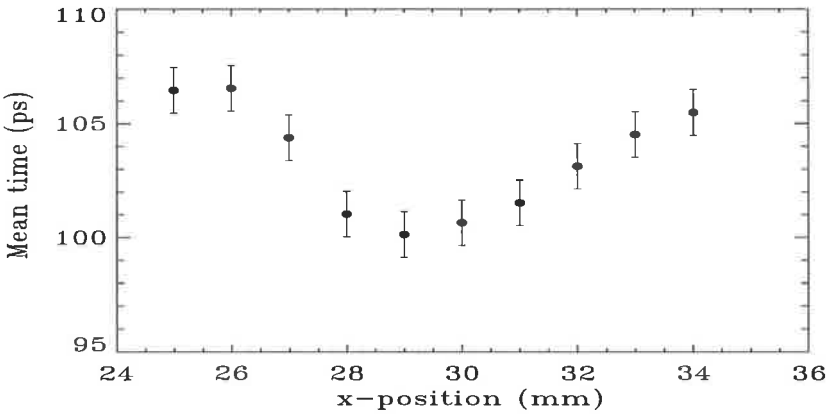

Figure 6.1: First photon mean arrival time $\bar{t_1}$. The x-axis indicates the position of the incident beam (and the detector) with $(y, z) = (L_y/2, 0)$ and $(y, z) = (L_y/2, L_z)$ being constant for the source and detector respectively.

6.2 Effect of heterogeneity on the first photon mean arrival time

With a reference to the same model set-up as shown in Fig. 1.4, the TPSF was computed for source-detector positions along the x-axis between x =25-34mm at 1mm intervals. This interval covers the distance between the centre of three adjacent cell columns including and parallel to the central axis. This range allows consideration of variation in the optical properties of the medium as seen by the first arriving photon, i.e., close to the central axis.

At each position, the FPD technique was applied to calculate the first photon p.d.f., $f_1(t)$, and consequently, the first photon mean arrival time, $\bar{t_1}$. Figure 6.1 plots $\bar{t_1}$ as a function of source-detector x-position in which a variation of about 10ps is observed. As the source-detector moves, the trajectories which contribute to $f_1(t)$ scatter through different regions (as well as the overlapping regions associated with the previous position). Therefore the 10ps variation reflects the (random) variations in the heterogeneous medium along the detector line-of-sight. An analysis of this variation will be included in later sections (6.5).

6.3 Embedded inhomogeneity

A heterogeneous medium with embedded totally and partially absorbing spherical inhomogeneities was simulated following the same procedures as described in section 5.6. The minimum inhomogeneity sphere size was $3mm$ in diameter as a $2mm$ one was not expected to be temporally resolved within an acceptable confidence level as shown in Fig. 5.8. Figure 6.2(a) plots $\bar{t_1}$ as a function of inhomogeneity diameter.

To compare the results of Fig. 6.2(a) with those of Fig. 5.8 corresponding to an homogeneous medium, the results of the two figures are over-plotted as shown in Fig. 6.2(b). In order to consider only the effect of embedded inhomogeneities, this figure plots the first photon mean arrival time w.r.t. that of the corresponding medium (heterogeneous or homogeneous) without the presence of inhomogeneity. The results of Fig. 6.2(b) indicate that, the heterogeneous medium is equivalent to that of an homogeneous one with its optical properties averaged over the local variations along the trajectories. In other words, an inhomogeneity causes the same shift in $\bar{t_1}$, so long as the surrounding media have the same average optical properties near and close to the propagation axis.

Following the above, $\bar{t_1}$, here corresponding to the (heterogeneous) medium in the absence of an embedded heterogeneity constitutes the "*background*". In the case of the 3 and $4mm$ inhomogeneities, $\bar{t_1}$ was also obtained for source-detector positions between x =25-30mm and x =25-32mm respectively[2], at $1mm$ intervals along the x-axis. The data of Fig. 6.1 were used to mark the background and Fig. 6.3 shows the results relative to this background, both for totally and partially absorbing cases.

Figs. 6.1 suggests that the variation in the background signal due to medium heterogeneity is of the order of $10ps$. This variation is larger than the observed shift in $\bar{t_1}$ due to the presence of a spherical inhomogeneity ($> 3mm$ in diameter). Tomographic techniques may be utilised to resolve the variations due to the heterogeneity and detect the shift in $\bar{t_1}$ due to the inhomogeneity. However, the implementability of tomographic techniques in a FPD system will be out of the scope of this report.

[2]The upper limit for the range of x marks the position for which $\bar{t_1}$ drops to within $0.5ps$ of the background (i.e. medium without the embedded inhomogeneity).

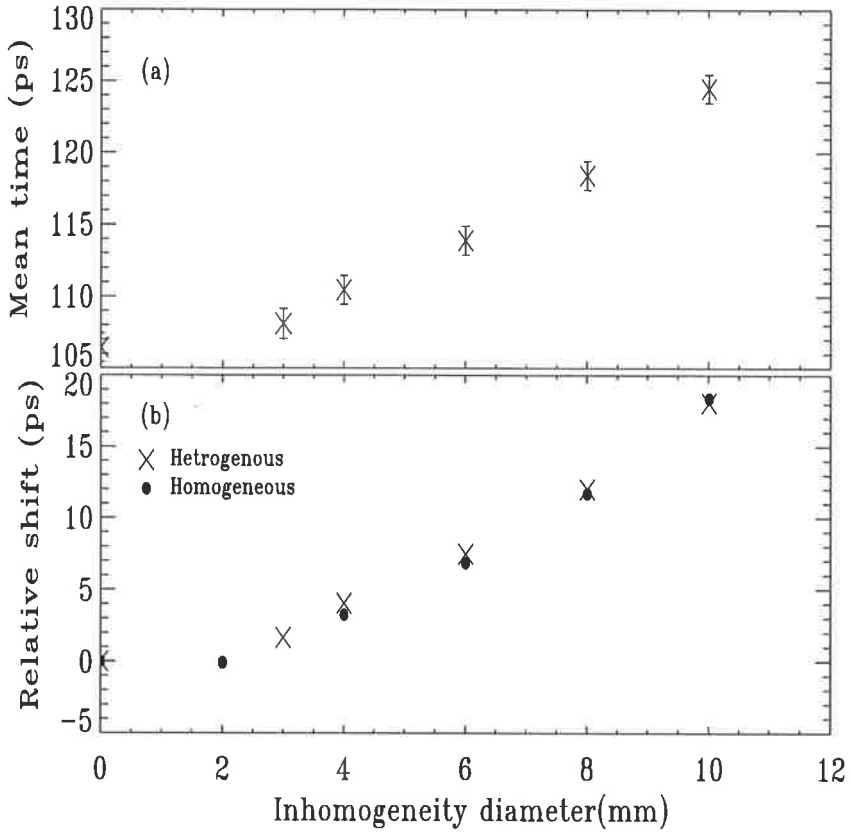

Figure 6.2: (a): Mean arrival time, $\bar{t_1}$, versus the inhomogeneity diameter for the totally absorbing spherical inhomogeneities located at the centre of the heterogeneous medium. Source and detector x-position was $x = L_x/2$. The zero inhomogeneity diameter corresponds to the absence of inhomogeneity. (b): A comparison of the shift in $\bar{t_1}$ due to introduced inhomogeneity in the homogeneous (cf. Fig. 5.8) and heterogeneous media. The scale in (b) is relative to $\bar{t_1}$, corresponding to the medium in the absence of the inhomogeneity. For clarity the error bars have not been shown in (b), however, it can be seen that the data for the heterogeneous medium ($\times$) falls within the error limits ($\pm 1ps$) of those of the homogeneous medium ($\bullet$).

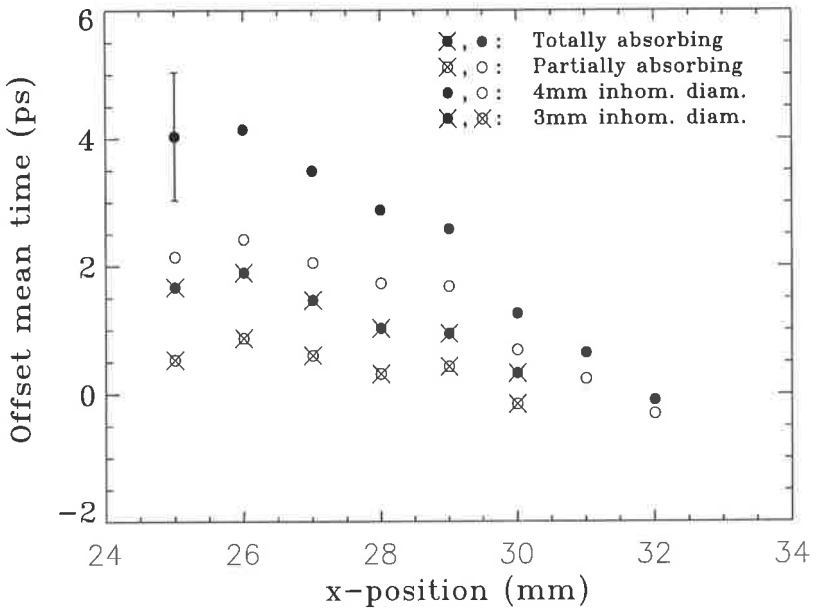

Figure 6.3: Relative (background subtracted) shift in the mean transit time, $\bar{t_1}$, for totally(solid) and partially absorbing inhomogeneities embedded at the centre of a heterogeneous medium. The inhomogeneity diameters were, $3mm$ ($\times$) and $4mm$. In the partially absorbing case $\mu_a = 0.2cm^{-1}$ and $\mu_s = 200cm^{-1}$. The x-axis represents the source-detector x-position. At each position, the mean arrival time corresponding to that of a heterogeneous medium without the inhomogeneity constituted the background and was subtracted from the corresponding $\bar{t_1}$ for the data with the embedded inhomogeneity.

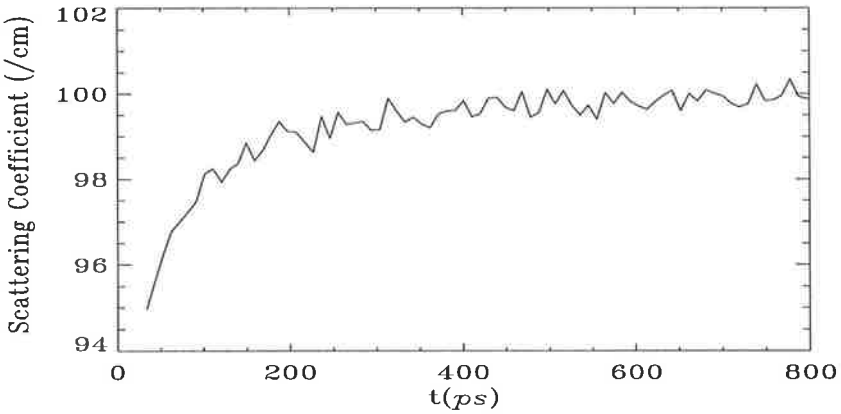

Figure 6.4: The *effective* scattering coefficient of a homogeneous medium as a function of the flight time.

6.4 Scattering coefficient and flight time

Theoretical studies [12, 77] propose that the detected photons with short times of flight undergo a smaller number of scattering events. This implies that the scattering cross section *effectively* decreases with a decrease in the flight time limit imposed by the detector. However, this has not been previously investigated quantitatively, due to theoretical as well as experimental difficulties in measurements involving short photon times of flight. In order to assess the response of the FPD system as a function of medium optical characteristics, one needs to accurately measure the effective optical properties of the medium for the applicable time scale.

In a simulation of an homogeneous medium the number of scatterings was recorded for each detected trajectory, which enabled the evaluation of number of scatterings per unit length experienced by the photon, here referred to as the *effective* scattering coefficient[3]. This quantity may then be plotted as a function of the trajectory flight time, as presented by Fig. 6.4. In producing these results a nominal scattering coefficient of $\mu_s = 100cm^{-1}$ was used and each trajectory contributed according to its weight.

It is evident from Fig. 6.4 that the effective scattering coefficient approaches the

[3]The effective scattering coefficient as defined here should not be mistaken with the effective attenuation coefficient, $\mu_{eff} = \sqrt{3\mu_a(\mu_a + \mu_s')}$ commonly used in the literature (described also in section 1.2).

nominal value for longer time scales. However, in the short flight time regime it drops rapidly, as it is expected that the number of scattering approach zero for the ballistic photons (i.e., the plot of Fig. 6.4 is expected to go through the origin). Figure 6.4 suggests that the considered effect is mainly evident for photon trajectories with flight times less than $300ps$. As $\bar{t_1}$ is expected to correlate with the optical properties of the medium, this effect may be significant for the FPD system as the first photon mean arrival time, $\bar{t_1}$, is near $100ps$ for a laser power of $10mW$ (cf. Fig. 5.3).

The mean of the effective scattering coefficient for the first arriving photon may then be evaluated as:

$$\bar{\mu_s} = \int_0^\infty \mu_s(t)\, f_1(t)\, dt, \tag{6.1}$$

where $\mu_s(t)$ is the effective scattering coefficient as a function of the flight time and its value is obtained from the plot of Fig. 6.4. $\bar{\mu_s}$ is the expectation value, $\langle \mu_s \rangle$, considering the non-uniform distribution of the first photon arrival time, t_1. Therefore, the trajectories contribute to this mean according to $f_1(t)$ as highlighted by Eqn. 6.1. This simply means that trajectory flight times which have a higher probability of occurrence contribute more heavily to $\bar{\mu_s}$. Equivalent results may be obtained for a heterogeneous medium in a similar fashion. The results presented in the rest of this chapter will be based on the determined values of $\bar{\mu_s}$.

6.5 Effect of the variations in scatter and absorption of heterogeneity on $\bar{t_1}$

In chapter 5 the sensitivity of the FPD system was assessed for uniform media of different optical density (cf. Figs. 5.5 and 5.6). It is, however, necessary to examine the FPD system w.r.t. heterogeneous media, as they better represent the small variations in the optical densities of a soft tissue such as the breast.

Random values of scattering coefficients, uniformly distributed between 70-130cm^{-1}, were assigned to cubical cells constituting 7 different heterogeneous media, each as described in section 6.1. The TPSF, $f_1(t)$, and the corresponding mean transit time, $\bar{t_1}$,

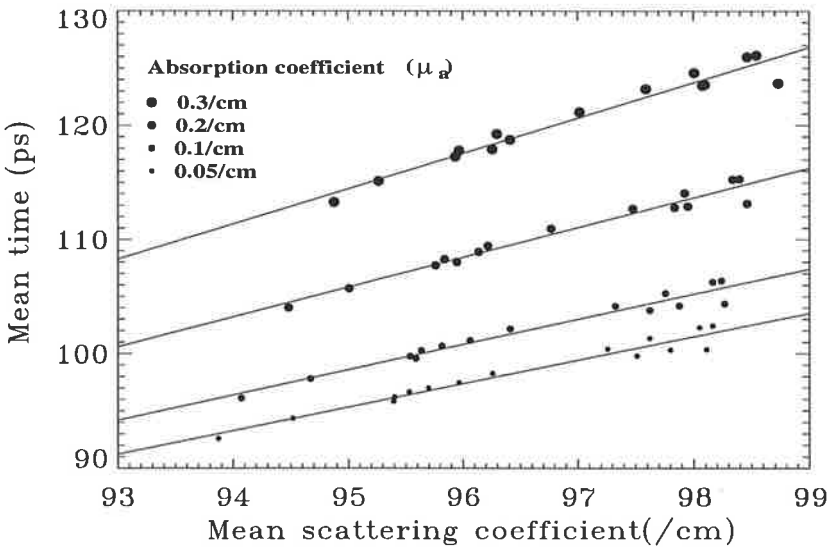

Figure 6.5: First photon mean arrival time as a function of the mean scattering and absorption coefficients. The lines represent linear least squares fit to the data as the absorption coefficient is varied.

were obtained for each configuration. In addition, the TPSF's (obtained at various x-positions) from section 6.3 for a heterogeneous medium without inhomogeneity were also used in producing the results of this section.

Figure 6.5 plots the mean arrival time of the first photon, $\bar{t_1}$, against the mean effective scattering coefficient, $\bar{\mu_s}$, corresponding to different values of μ_a. This figure demonstrates a strong correlation (with correlation coefficient [131], $r > 0.99$) between $\bar{t_1}$ and $\bar{\mu_s}$. This implies a strong correlation displayed by the FPD system in detecting variations in the optical properties of the medium close to the propagation axis (detector line-of-sight) as encountered by the first arriving photon.

From the results of Fig. 5.6 of the previous chapter, it can be concluded that a stronger or weaker dependence of absorption on the scatter may result in larger or smaller shifts in $\bar{t_1}$. However, quantitative assessment of the possible outcome, when no clear relationship between the absorption and scatter is available, is out of the scope of the present paper.

The above results confirm those of chapter 5, in suggesting an increase in $\bar{t_1}$, as $\bar{\mu_s}$ and μ_a are increased. The linear fit to the data of Fig. 6.5 for $\mu_a = 0.1cm^{-1}$ pre-

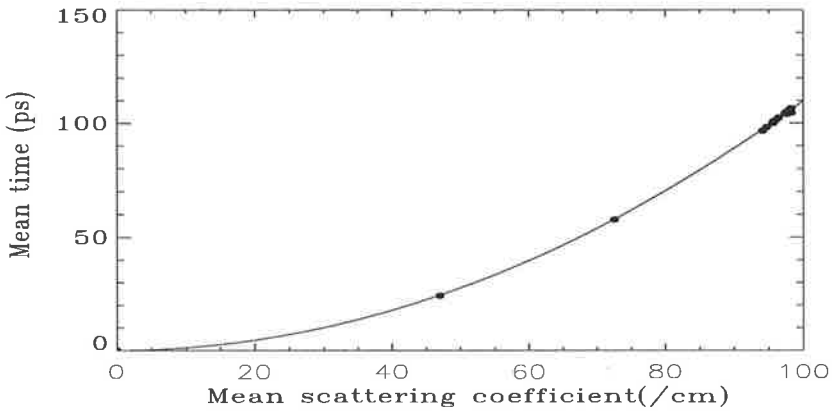

Figure 6.6: First photon mean arrival time, $\bar{t_1}$ versus $\bar{\mu_s}$. The results of Fig. 6.5 (group of points) have been combined with those corresponding to lower values of μ_s=50 and $75cm^{-1}$.

dicts $\bar{t_1}$ =200 and $300ps$ ($\pm 10\%$) corresponding to scatter coefficient values of 160 and $200cm^{-1}$. This is in agreement with the previously obtained results of Fig. 5.5. However, it is noted that this linear fit does not intersect the origin. The intersection with the origin reflects the requirement that for the unscattered trajectories (e.g., a medium with $\mu_s = 0cm^{-1}$) the delay should vanish as all trajectories become ballistic. Homogeneous media with scattering coefficients of 50 and $75cm^{-1}$ were therefore simulated. The results are presented in Fig. 6.6.

The data of Fig. 6.6 was fitted with a quadratic curve. From the fitted curves it was found that, for a laser power of $10mW$, the following equation describes $\bar{t_1}$:

$$\bar{t_1} = 0.01\bar{\mu_s} + 0.0109\bar{\mu_s}^2 \tag{6.2}$$

Equation 6.2 was evaluated based on $\mu_a = 0.1cm^{-1}$. Although this equation accurately describes the dependence of $\bar{t_1}$ on $\bar{\mu_s}$, it over estimates the results for a medium with higher values of the scattering coefficient. It is therefore concluded that the quadratic and the linear models should be used for mean scattering coefficients of below and above $\bar{\mu_s} \approx 100cm^{-1}$ respectively.

6.6 The FPD versus the integrating system

In order to compare the ability of the FPD and conventional integrating systems in detecting small variations in the optical densities along the detector line-of-sight, two cell arrangements of section 6.5 were re-examined and are referred to as arrangements 1 and 2. It is noted that the rearrangement of cells ensured the same global average scattering coefficient for the two media. This is analogous to two tissues of the same type but different subjects.

Figures 6.7(a) and (b) show the integrated intensity (c.d.f., F(t)) and the normalised TPSF, $f(t)$, for the two arrangements, while Fig. 6.7(c) is a graph of the effective scattering coefficient as a function of trajectory flight times. The data of Fig. 6.7(c) demonstrates that the two media are indeed different along and near the propagation axis, the most likely region for shorter times of flight. The merging of the curves reflects the fact that, globally, the two media exhibit similar optical characteristics. In particular Fig. 6.7(a) indicates that for times of flight longer than about $220ps$ (corresponding to $\log(F(t)) \simeq -8.5$), the two media become indistinguishable for an conventional integrating system whose output is the integrated intensity based on the graph of $F(t)$.

The two arrangements, 1 and 2, were also represented by the two data points on Fig. 6.5 at $(\bar{\mu_s}, \bar{t_1})_1 = (94.7, 98.0)$ and $(\bar{\mu_s}, \bar{t_1})_2 = (98.2, 106.4)$ where the subscripts mark the corresponding arrangement. Assuming a temporal resolution of $1ps$ for the FPD system, these two points are clearly distinct from one another on the $\bar{t_1}$ scale, i.e., yielding a difference of $8.4ps$ in $\bar{t_1}$.

The above results indicate the superiority of the FPD system over a conventional integrating system in detecting variations in the optical properties of the medium of the order of a few percents. It is noted that this difference in the two media becomes more significant and hence detectable at or below $\sim 100ps$ which is typically the mean arrival time of the first detected photon. It is also observed that near this time scale a significant difference is also observed in the integrated intensities as presented by Fig. 6.7(a). However, current integrated systems fail to detect (less than) single or

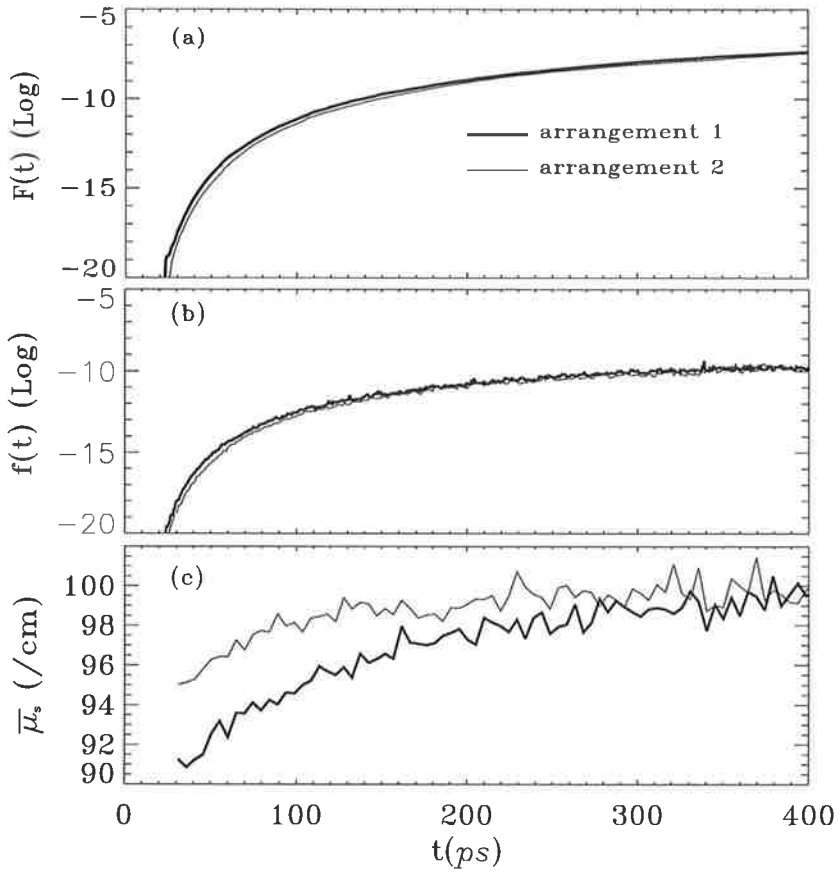

Figure 6.7: (a): the c.d.f., $F(t)$, (b): normalised TPSF, f(t), and (c): the effective scattering coefficient, $\bar{\mu_s}$, for two heterogeneous media representing two random arrangements of the same set of cubical cells. The c.d.f. F(t) represents the response of conventional integrating systems. Note that the noise characteristics of such integrating systems have not been included in (a) and (b).

partial photons[4]. Therefore, although the two curves of Fig. 6.7(a) may differ by a factor of ~ 3 in $F(t)$, at $\sim 100ps$, this does not reflect the ability of a conventional integrating system in differentiating between the two media.

[4]A partial photon represents the probability of detection of a single photon per incident pulse within the detection time.

6.7 Conclusion

For a FPD system, it has been shown that a heterogeneous medium may be regarded as the homogeneous medium with the spatial variations in the optical properties averaged over the trajectory path. Back-projection techniques may be applied using measured mean transit time of the first arriving photon, $\bar{t_1}$, to resolve these variations which are averaged over the detector line-of-sight for each projection angle. A high degree of positive correlation between $\bar{\mu_s}$ and the variation in the optical properties, μ_a, and $\bar{t_1}$, suggests high sensitivity w.r.t. the small variations in the optical properties of the medium as required in TI. This strong positive correlation, particularly with μ_a, provides a basis for a high contrast resolution which will be discussed in the following chapter.

Chapter 7

Contrast and signal-noise-ratio

7.1 Motivation

In this chapter, a concise account is given for the evaluation of the contrast and signal-noise-ratio (SNR) for a FPD system. Based on an analysis of the SNR, the number of incident pulses per scan position needed to achieve a required SNR is also derived.

7.2 Contrast

For a conventional integrating time-gated TI system, the contrast $C_{conv.}$ is defined [107] as the difference in the signal intensity transmission per unit length and with reference to Fig. 7.1a,

$$C_{conv.} = \frac{I_1 - I_2}{L_z}. \tag{7.1}$$

However, for a FPD system where the received signal does not change (one photon per pulse) this definition of contrast cannot be used. Instead, the contrast C_{FPD} (or just C) is defined to be the difference in *mean transmission time* (of the first arriving photon) per unit length, i.e.,

$$C = \frac{\bar{t_1} - \bar{t_2}}{L_z}. \tag{7.2}$$

In Fig. 7.1 where the tissue types are homogeneous, $\bar{t_1}$ does not have a spatial dependence except close to the boundaries. For the contrast to be a meaningful pa-

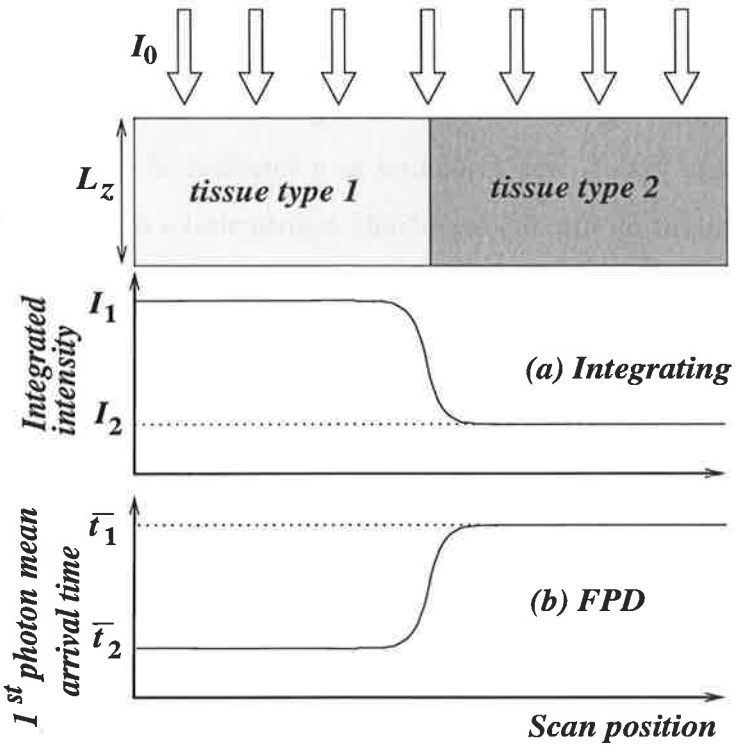

Figure 7.1: Determination of contrast by even illumination of the medium consisting of two adjacent tissues of different optical densities.

rameter, it is also expected that C varies continuously with smooth variations in the optical properties. Therefore, a measurement of mean arrival time, $\bar{t_1}$, is expected to correlate with the optical properties and provide information about the contrast.

7.2.1 Contrast and medium optical properties

Instead of the step function configuration illustrated in Fig. 7.1, assume a medium with a continuously varying optical properties (e.g., μ_s) from left to right, in an FPD system, with a fixed laser power. Then, the horizontal (spatial) axis of Fig. 7.1 would correspond to variations in the optical properties. This configuration would be equivalent to that of Fig. 6.5 in the sense that $\bar{t_1}$ was evaluated as a function of variation in the optical properties $\bar{\mu_s}$. Each point on Fig. 6.5 essentially represented a different medium (tissue type). Given the medium thickness L_z, the contrast C for any two tissue types is the difference in the time coordinates corresponding to a pair of points on Fig. 6.5. With reference to Fig. 6.5, as an example, for a fixed laser power of $10mW$, $L_z = 5.0cm$ and two media (tissue types) with $(\bar{\mu_s}, \mu_a) = (94.5, 0.1)$ and $(97.5, 0.2)cm^{-1}$, the corresponding $\bar{t_1}$s are 98 and $113ps$ respectively which results in a contrast of $C = 3.0ps\ cm^{-1}$.

For each value of the absorption coefficient, it is noted that the slope of the linear fit to the data of Fig. 6.5 increases with increased value of the absorption coefficient. This implies that better contrast is achieved for higher values of absorption coefficient. However, the limitations in the temporal resolution of the system should be considered when assessing the contrast. For example, for a fixed value of $\mu_a = 0.1cm^{-1}$ of Fig. 6.5, the slope of the fitted curve is $\sim 5.8ps\,cm$. Which means that for a temporal resolution of $1ps$ the minimum detectable differential in the mean scattering coefficient, $\bar{\mu_s}$, is $1.7cm^{-1}$ which closely corresponds to the same differential in μ_s.

7.2.2 Contrast and laser power

It was shown in Fig. 5.3 that $\bar{t_1}$, and hence differential in $\bar{t_1}$, decreases with increased laser power. Combined with Eqn. 7.2, it is therefore expected that contrast is also

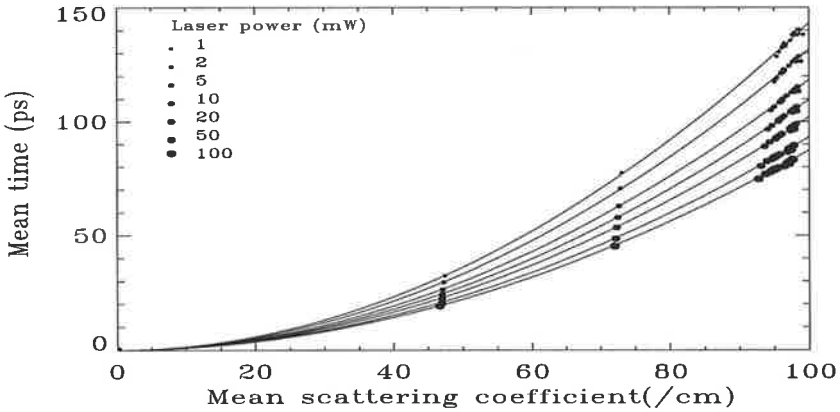

Figure 7.2: Variation in $\bar{t_1}$ with laser power for the results presented by Fig. 6.6.

affected by the laser power[1]

With a reference to Fig. 6.6, to study the effect of the laser power on the contrast, the number of photons per incident pulse, N_0 (laser power) was increased and the corresponding $f_1(t)$'s and the corresponding $\bar{t_1}$s of Fig. 6.6 were calculated. Figure 7.2 presents the results. This figure suggests that the system contrast degrades as the laser power is increased. This may be deduced from the decrease in the gradients of the fitted curve fits[2] corresponding to higher laser powers. A decrease in the gradient implies smaller time differential for a given pair of optical properties (e.g., $\bar{\mu_s}$).

7.3 Signal-noise ratio (SNR)

A comprehensive discussion of SNR has been given by Joblin [133] for a conventional integrating system where the calculations are based on the detection probability of

[1]In an extreme case, it is also intuitive that a very high laser power cannot differentiate between different tissues types as $f_1(t)$ approaches a δ-function near t=0. This would then imply that, regardless of the tissue type, no detectable variation in $f_1(t)$ and consequently $\bar{t_1}$ may be observed.

[2]Note that the quadratic curve fits of Fig. 7.2 do not obviously all have the same coefficient, c_1 and c_2 in the quadratic relation $\bar{t_1} = c_1\bar{\mu_s} + c_2{\bar{\mu_s}}^2$, as described in section 6.5. It was found empirically that, more generally, $c_1 = 0.01$ remains a constant whereas $c_2 = 0.00425 + 0.6(10^{10}p)^{-0.1779}$, with p measured in milliwatts. The factor $10^{10}p$ represents the number of photons N_0 in the incident pulse. The quadratic curves of Fig. 7.2 have been evaluated based on $\mu_a = 0.1cm^{-1}$.

a photon within the integration time of the detector. For FPD system this method does not apply, as the detector detects one and only one photon from each pulse. The FPD signal is an estimation of a mean value $\bar{t_1}$, calculated for the first arriving photon from a train of incident pulses. This mean value constitutes the signal, and the noise contributes to the error in the estimation of this mean. The SNR, being a function of the noise in the signal, would subsequently depend on the standard deviation of the mean, $\bar{\sigma_1}$ and is given by:

$$\text{SNR} = \bar{t_1}/\bar{\sigma_1}. \tag{7.3}$$

Let n, be the number of incident pulses per scan position or equivalently the number of detected first photons contributing to the signal. One then arrives at the following question: ***How large should n be to achieve a required SNR?***

From Eqn. 7.3, it becomes a question of reducing $\bar{\sigma_1}$ to a value which ensures a SNR greater than that required. For the purpose of producing a pixel value for a planar projection, the mean $\bar{t_1}$ (or $\bar{\sigma_1}$) is the sufficient moment to be estimated for $f_1(t)$. However, it may also be useful to derive other moments which characterise skewness and kurtosis (flatness). In this case the method of moments[3] can be used to estimate n. This involves continued sampling until the moments remain unchanged within a given tolerance limit.

Before a numerical estimate of the SNR is given, it is noted that no functional form is known for the normalised TPSF, $f(t)$, to make possible the analytic evaluation of $\bar{\sigma_1}$. The first arriving photon p.d.f., $f_1(t)$, is therefore approximated to a Gaussian p.d.f. with a mean $\bar{t_1} = 100ps$ and a standard deviation $\sigma = 20$. This is typically close to $f_1(t)$ for an homogeneous medium with $\mu_s = 100cm^{-1}$, $\mu_a = 0.1cm^{-1}$ and a laser power of $10mW$. For a Gaussian p.d.f., it is known [137] that the error in the mean, $\bar{\sigma_1} = \sigma/\sqrt{n}$, and hence:

$$\text{SNR} = \frac{\sqrt{n}\,\bar{t_1}}{\sigma}. \tag{7.4}$$

[3]Method of moments is based on the fact that two equivalent distributions produce equal moments. In practice the first four moments sufficiently specify a distribution.

$\log_{10}(n)$	$\bar{t}_1$	$\bar{\sigma}_1$	SNR	Skewness	Kurtosis
exact	100.00	0.00	∞	0.0	3.00
1.0	102.50	7.51	13.63	0.32	2.41
2.0	99.40	2.07	47.86	−0.24	2.90
3.0	99.64	0.62	159.18	0.02	3.19
4.0	99.51	0.19	501.26	0.01	3.09
5.0	99.41	0.06	1569.73	−0.01	3.01

Table 7.1: Comparison of various parameters associated with that of an exact Gaussian distribution (top row) as a function of n, the number of incident pulses per scan position.

Table 7.1 presents the results for the associated parameters corresponding to various values of n, the number of incident pulses per scan position. Requiring a temporal resolution of better than $1ps$, Table 7.1, suggests a value of $n = 10^3$-10^4. It is further noted that this range of n values guarantees obtaining the third moment (skewness) to within less than 1% and flatness[4] to within 5%.

Furthermore, it is also possible to estimate n without considering an approximate Gaussian p.d.f.. This is done by replacing the estimation of the noise, characterised by $\bar{\sigma}_1$, with some specified confidence interval (CI). The CI corresponds to a confidence level, CL (e.g., 95%), for the estimation of the population mean $\bar{t}_1$. Here, $f_1(t)$, σ and $\bar{t}_1$ are all unknown as in the case of a real scanning situation. However, a *sample* mean, here also noted as $\bar{t}_1$, and a *sample* standard deviation s for the flight times of the first arriving photons can be evaluated while the data is being collected at each scan position. The confidence interval boundaries would be [137]:

$$\bar{t}_1 \pm \Delta_{\bar{t}_1} = \bar{t}_1 \pm t_{\frac{1}{2}\alpha,n-1} s/\sqrt{n}, \tag{7.5}$$

for CL= $100(1-\alpha)$%. The statistic $t_{\frac{1}{2}\alpha,n-1}$ is the Student's *t-distribution* with $n-1$ degrees of freedom and parameter $\frac{1}{2}\alpha$. For a required SNR (or equivalently $\Delta_{\bar{t}_1}$), n may then be adjusted such that the confidence interval given by Eqn. 7.5 is contained within $\bar{t}_1 \pm \bar{\sigma}_1$ which ensures a SNR greater than that specified. For CL=95%, temporal resolution of better than $1ps$ ($\bar{\sigma}_1 \leqslant 0.5$ or SNR$\geqslant$200) and s=20, Eqn. 7.5 suggests[5] a

[4]Kurtosis, being a measure of flatness does not have as direct relevance to the estimation of the mean compared to the lower moments.

[5]For values of $n \geqslant 120$ and CL=95%, $t_{\frac{1}{2}\alpha,n-1} = 1.96$.

value of $n = 6400$ which is again in agreement with that suggested by the Gaussian approximation approach.

7.4 Conclusion

It has been shown that the system contrast improves with an increase in the medium absorption and degrades with an increase in the incident laser power. The SNR analysis suggests that in order to achieve a temporal resolution of better than $1ps$, 10^3-10^4 photons per incident pulse are required for each scan position. For a laser pulse repetition of 1MHz, this does not pose insurmountable time constraints on the clinical use of the FPD system.

Chapter 8

Conclusion

8.1 Milestones achieved

It has been demonstrated that a higher spatial resolution in time-resolved transillumination imaging (TI) may be achievable by employing time-of-flight (TOF) measurement of the first detected photon from each incident pulse. The initial step in a feasibility study of a first photon detection (FPD) system was to devise an indeterministic Monte Carlo (IMC) technique which was validated against published experimental results. The IMC enabled simulation of early arriving photons for source-medium-detector geometries similar in optical properties and dimensions to those of clinical interest. This allowed the full construction of the temporal point spread function (TPSF) from which the statistics of the single early arriving photons were derived analytically, with an emphasis on the first arriving photon. Finally, the FPD technique was applied to both homogeneous and heterogeneous media with, and without embedded spherical inhomogeneities.

8.2 Resolution, Contrast and SNR

It was shown that a spherical inhomogeneity, $3mm$ in diameter may be distinguished from the background medium (i.e., medium without the presence of the inhomogeneity). Figure 8.1 shows 2-D planar images obtained in the presence of inhomogeneities. These

images are based on the data presented in Fig. 6.3, assuming radial symmetry[1] and added normally distributed noise with a standard deviation of $1ps$[2] reflecting the error in determining $\bar{t}_1$ for a homogeneous medium. A preliminary observation based on these images confirms the distinguishability of a $3mm$ totally absorbing inhomogeneity. It should, however, be mentioned that this does not exactly reflect the spatial resolution of the system. In order to evaluate the system spatial resolution, one needs to follow the analysis presented in chapter 4.

Assume that it is possible to perform a continuous integration of the TPSF for time scales within the first photon arrival time, i.e., the time scale for which the c.d.f, $F_1(t)$, is less than unity. Then in order to derive the spatial resolution as a function of the "gating" time from the ERF (cf. Fig 4.3 and section 4.3.2), one needs to rescale the TPSF according to the first photon p.d.f., $f_1(t)$, and repeat the analysis as per chapter 4.

The above assumption is invalid as a sub-single photon integration is not possible for a single pulse. Although, measurements over a number of incident pulses may lead to an estimate, this approach was not pursued and needs further investigation.

The results of chapter 4 (fig. 4.4) suggested that a spatial resolution of $\sim 2mm$ is theoretically achievable when $\mu_s' = 8cm^{-1}$. However, in chapters 5 and 6 it was found that the mean arrival time of the first detected photon is $\sim 100ps$ with $\mu_s' = 5cm^{-1}$. This means that the theoretical $\sim 2mm$ spatial resolution may only be achieved if the acceptance time window of the FPD system is reduced to $\sim 10ps$ which implies no photon would be detected for a number of incident pulses at each scan position. This would then require significantly higher number of incident pulses per scan position to achieve a required SNR.

The contrast of the FPD system as evaluated based on a definition given by Eqn. 7.2 reflects the sensitivity in response to small changes in the optical characteristics of the

[1]Here, for simplicity a radial symmetry was assumed. It is however clear that, although this assumption is valid in the case of the spherical inhomogeneity, it is invalid for the surrounding (heterogeneous medium). In practice, a proper 2-D scan is therefore required to asses the image quality.

[2]The $1ps$ standard deviation reflects accuracy of the data in estimating $\bar{t}_1$ and also the sub-picosecond temporal resolution requirement of the FPD system.

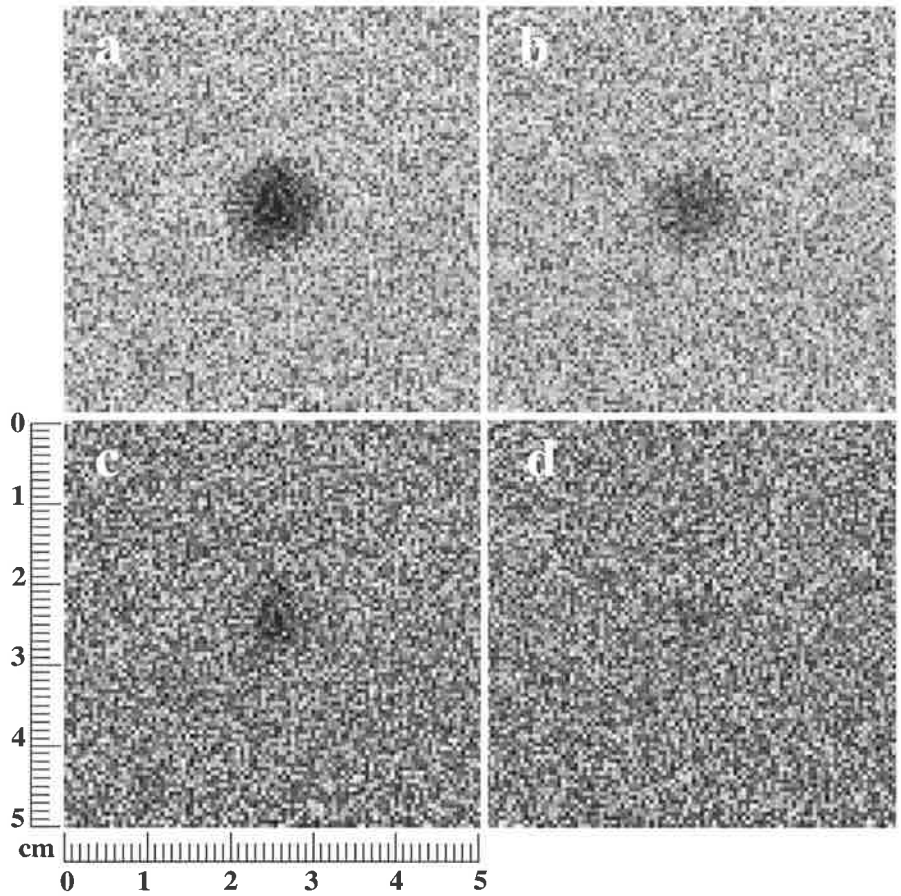

Figure 8.1: A 2-D planar projections of spherical inhomogeneities embedded in a heterogeneous medium constructed based on the data presented in Fig. 6.3. The images correspond to $4mm$ (top) and $3mm$ (bottom) in diameter, totally (right) and partially (left) absorbing inhomogeneities. The noise has been added at twice the spatial frequency.

medium close to the detector line-of-sight. Given an ideal detector and sub-picosecond temporal resolution, the results (cf. Fig 6.5) indicate that changes of the order of one scattering per centimetre in μ_s may be detected. The differential in the effective scattering coefficient is quite distinct at times $\leq 150ps$ achievable with FPD as compared to minimal time achievable with the conventional integrating system (cf. Fig. 6.7). For a conventional integrating system the variance in the detected optical characteristics is large due to the inclusion of long photon trajectories which do not accurately map the optical characteristics of the system along the detector line-of-sight.

The definition for the SNR was based on the accuracy in the estimation of the first photon mean arrival time. Based on the SNR analysis, it was possible to determine the number of pulses (per scan position) required to estimate the first photon mean arrival time to within an acceptable accuracy determined by a confidence level (95%).

8.3 Limitations

The system noise and its influence on the results presented was not studied and an ideal system was considered. Although, this was partially due to limitations in the scope of the study, it was important to assess a noise free system to enable evaluation of its full potentials and theoretical strength.

Deviations from an ideal system are broadly characterised by the noise. The noise may be due to either thermal (statistical) fluctuations or detector inefficiency. The thermal noise characterises the noise in the laser and the detector output, in the absence of the signal. While the thermal noise is general and typical of any TI system, the noise representing the detector inefficiency, in detecting only the first arriving photon, is specific of a FPD system. Therefore, here, this type of noise is referred to as FPD noise. Although, the efficiency of the FPD system (and hence the FPD noise) was characterised in the form of Eqn. 5.10, the characteristic efficiency response factors α_n are yet to be determined for a physical system.

The key issue in the assessment of a FPD system has been the dependence of the flight time of the detected single photons on the system performance. As such, due

to possible inclusion of the later arriving photons, the FPD noise would degrade the spatial resolution. The statistics of the second or later arriving photons involve complex order statistics which is out of the scope of the present script. The thermal noise, on the other hand, puts limitations on the upper limit for the SNR. This may lead to an optimisation of the number of incident pulses per scan position as per section 7.3.

Finally, the types of media and inhomogeneities studied in this report are not comprehensive. Other factors, such as variations in the medium geometrical shape, refractive index and the anisotropy may also impact on the performance of a FPD system.

8.4 Future direction

From the experimental point of view the FPD approach faces a few challenges. This system would require an ultrashort laser pulse and an ultrafast detector with high extinction coefficient which would only record the first arriving photon. Presently, lasers capable of producing pulses of the order of 10's of femtosecond are available. The $1ps$ ($\gg 10fs$) temporal resolution requirement relaxes the need for the modification of the derived theoretical results to accommodate deviations from δ-function temporal profile of the beam. The challenge therefore shifts towards the availability of a suitable detector. Research into developing a suitable detector is therefore suggested.

Given the technological constraints are removed, with a reference to Fig. 1.5 the specifications listed in Table 8.1 are recommended for a FPD system to be realised experimentally for clinical purposes[3].

For 10^4 pulses per scan position, the intrinsic scan time is expected to be about 1 second per cm^2 at 1MHz pulse repetition when a single beam is used. Although, multiple beam-detector geometry may be adopted, technical difficulties associated with

[3]The values listed in table have been calculated based on the maximum permissible exposure of the order of $10mW$ as required by the Australian and New Zealand standards [136]. This laser power is equivalent to about 10^{11} photons per incident pulse.

Pulse width	$< 100fs$
Repetition rate	$\sim$ 1MHz
No. pulses per scan position	$10^3 - 10^4$
Detector temporal resolution	$< 1ps$

Table 8.1: Temporal requirements for a FPD system.

system scan controls are to be taken into consideration which may increase the scan time.

The maximum permissible exposure (MPE) is about $10mW/mm^2$ [136]. This means that if the beam size is $1mm^2$ the maximum average laser power may be about $10mW$. For this laser power and a pulse repetition of 1MHz a pulse separation of $1000ns$ may be achieved which is sufficiently longer than 7-$10ns$, the typical duration of the TPSF. This allows sufficient delay in re-triggering which insures no cross talk between consecutive pulses at a scan position. The response time of the system should however be taken into account. For example, while 50MHz pulse repetition may also be considered, this allows the system only $20ns$ to reset for the next pulse. In case this is not a sufficient time and some pulses would be missed, it is not a useful exercise to increase the pulse repetition. More importantly, for a pulse repetition of 1MHz (at $10mW$) the first photon arrives within $150ps$. If the pulse repetition is increased (for a fixed laser power), this timescale shifts toward longer times, as is expected, because the number of photons per incident pulse would decrease (cf. section 5.4).

While there is more scope for continued theoretical examination of the FPD system as highlighted above (mainly the FPD noise quantification), the work of this study indicates it is worthwhile pursuing the experimental and clinical realisation of a FPD system.

Appendix A

Statistical tests on the RNG

A range of tests described by Sim and Nitschike [119] are performed on the pseudo-random number generator (RNG) *mzran*13 due to Marsaglia and Zaman [120]. These tests include application tests (cf., chapter 3) and statistical tests: uniformity (over $[0, 1]$), randomness and seriality w.r.t. both numbers and constituent digits.

Visual test (Number)

The visual test provides a subjective indication of any serial correlation between successive pairs of numbers. A sample size of 10^5 was divided in two successive pairs of numbers and used as the coordinate values of points on a 2-D plot.

The results are presented in Fig. A.1. Appearance of a line or considerable cluster(s) of dark or light regions would indicate serial correlation. Here, no obvious serial correlation is observed.

Frequency test (Number)

A χ^2 test [137] was carried as a measure of goodness of fit to test the null hypothesis of equivalency of the sample distribution and that of a uniform distribution. The unit interval $[0, 1]$ was divided into $n = 100$ equal bins. For a sequence of length[1] $N = 10^6$,

[1]Sample sizes chosen here are sufficient to produce the distribution with stable moments (up to

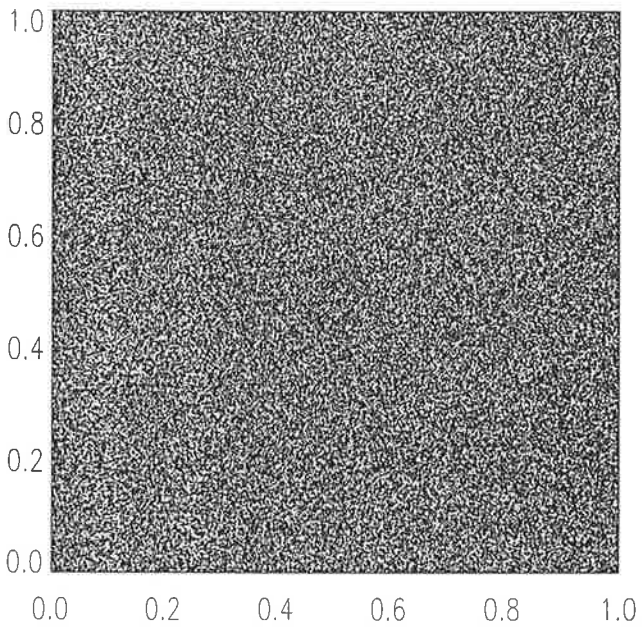

Figure A.1: The visual test on random numbers generated by *mzran13*. The coordinates of each point on the plot represent two consecutively generated random numbers.

	1st	2nd	3rd	4th	5th
Expectation	.50000	.33333	.25000	.20000	.16667
Observation	.50009	.33343	.25009	.20009	.16675

Table A.1: Moments test for the RNG, *mzran13*.

the statistics, f, given below is expected to be χ^2 with (n-1) degrees of freedom:

$$f = \sum_{i=1}^{n} \frac{(o_i - e_i)^2}{e_i},$$

where $e_i(= N/n)$ is the expected sample size per bin and o_i is the corresponding observed value. A χ^2 of 87.89 for 99 degrees of freedom suggest that result is not significant at the 5 per cent level and the null hypothesis is accepted with 95% or better confidence level.

Moments test (Number)

It is expected that moments of the distribution of the generated random numbers follow those of a uniform distribution over the interval [0,1] given by:

$$\mathrm{k}^{th}\mathrm{moment} = \frac{1}{N}\sum_{i}(X_i)^k = \frac{1}{1+k}$$

where N is the sample size, and X_i is the i^{th} sample element, and the last equality is due to the distribution being uniform. Table A.1 compares the expected and observed leading five moments with $N = 10^6$.

Frequency test (Digit)

From a sample size of $N = 5 \times 10^6$ generated random digits[2], each digit is expected to occur with a frequency of $0.1N$ or a 0.1 relative probability. The following probabilities were observed corresponding to digits from 0 to 9 respectively.

the fourth order). This means that the first four moments would not change significantly if larger samples were taken.

[2] 10^6 numbers were generated for each of which 5 digits were recorded.

Gap size	0	1	2	3	4	5	6	7	8	9	10	>10
Exp. Freq.	.1	.09	.081	.0792	.0656	.059	.0531	.0478	.0430	.0387	.0349	.3138
Obs. Freq.	.0992	.0898	.0810	.073	.0662	.059	.0528	.0481	.0430	.0387	.0346	.3136

Table A.2: Relative expected and observed frequency of a gap size between occurrence of any digit (0-9).

0.10007	0.10003	0.09995	0.10006	0.0997
0.09998	0.09991	0.10008	0.09994	0.1002

Serial test (Digit)

Similar to the visual (number) test a the seriality test is performed to check for (unbias) relative frequency of occurrence of specific pairs of digits. The probability of occurrence of any digit after a specific one is expected to be 0.1. The results presented below show the occurrence of each digit (0-9) following the occurrence of an arbitrarily chosen digit (in this case 2) respectively.

0.1005	0.0996	0.1003	0.1010	0.0997
0.1004	0.0991	0.0992	0.0998	0.0998

Gap test (Digit)

The relative expected and observed frequency of a gap size between occurrence of any digit (0-9) is presented in Table A.2. A gap size of 0 indicate successive occurrence.

Poker test (Digit)

Consecutive sets of five digits were considered to present a "poker hand" for a sample size of $N = 5 \times 10^6$ with the relative expected and observed frequencies as presented by Table A.3.

Hand	Expected Freq.	Observed Freq.
1 pair	0.5040	0.5029
2 pairs	0.1080	0.1084
3 of a kind	0.0720	0.0720
Full house(3 of a kind + 1 pair)	0.0090	0.0090
4 of a kind	0.0045	0.0045
5 of a kind	0.0001	0.0001
Bust(none of the above)	0.3024	0.3029

Table A.3: Expected and observed frequency of each set of 5 digits (poker hand).

The results of the above statistical tests along with the application tests outline in chapter 2 show that the observed distributions generated by *mzran13* are within 1% of the expected distributions and hence indicate that this RNG is sufficiently good for the purpose of MC simulation of light propagation in a turbid media.

Appendix B

Algorithm for the IMC simulation

The following is a simplified version of the C code for the IMC algorithm. The structure of the code was adopted from the code written by Wang and Jacques [72] but the routines were rewritten by the author. Here, only the parts which are specific to the source used to produce the results of this work are included. For clarity, those components common to a SMC simulation and other components such as those dealing with the extraction and allocation of filenames and input specifications have been omitted. Also the output parameters have been reduced to only those needed to perform the calculation outlined in section 3.2, i.e., the flight time, weight and the number of attempts. The various C structures used in the following subroutines are also included following the C algorithms.

Other parameters which the algorithms included below may output are: Number of photon interactions (`Photon.ints`), maximum and minimum radial distance from the propagation axis at the mid-plane (`Photon.rmidmax` and `Photon.rmidmax`), photon exit co-ordinates (`Photon.x, Photon.y and Photon.z`) and photon exit directions (`Photon.x_dir, Photon.y_dir and Photon.z_dir`).

```
/*************************************************************************/
/*** Photon (trajectory) structure ***/
typedef struct {
  long  photonID;                          /* number being simulated */
  double x,y,z,r;                          /* photon x,y,z position */
  double xinit,yinit,zinit;                /* initial (beam) x,y,z position */
  double xmax,ymax,zmax;                   /* max x,y,z position undergone */
  double rmax,rmidmin,rmidmax;             /* max & mid-plane radial distance */
  double x_dir,y_dir,z_dir;                /* x, y and z */
  double x_dirinit,y_dirinit,z_dirinit;    /* initial (beam) x, y and z */
  double w;                                /* weight. */
  Boolean dead,slow,detected;              /* status */
  int P_Medium,F_Medium;                   /* present and future host medium */
  double s;                                /* current step size */
  double sleft;                            /* remaining step size  */
  double FlightTime;                       /* current flight time */
  double TimeToDetector;                   /* ballistic time to detector */
  double TimeToAP;                         /* ballistic time to attr. point */
  double FlightDelay;                      /* delay time in stacks */
  double Tumour_FT;                        /* flight time in tumour */
  long ints,Tumour_ints;                   /* interactions in tissue & tumour */
  int part;                                /* stack allocation part */
  double WasHere;                          /* recorded (presence) at a stack */
} PhotonStruct;

/*************************************************************************/
/*** Photon package (stack) structure ***/

typedef struct {
  PhotonStruct * PhotonPackageSpecs;       /* photon */
  int PhotonPartPtr;                       /* photon at each stack */
  int DelayingStack;                       /* delaying stack */
} PhotonPackageStruct;

/*************************************************************************/
/*** Medium parameter structure ***/

typedef struct {
  double n;          /* refractive index of a Medium. */
  double mua;        /* absorption coefficient */
  double mus;        /* scattering coefficient */
  double g;          /* anisotropy */
  double x,y,z,r;    /* dimensision (position and radius if sherical) */
} MediumStruct;
```

```
/*************************************************************************/
/*** System (source, medium, detector) structure ***/

typedef struct {
  double R_source;                    /* beam radius */
  double P_source;                    /* beam position */
  double R_detector,xdet,ydet,zdet;   /* detector radius and position */
  double TimeLimit;                   /* detection time limit */
  double xap,yap,zap;                 /* x,y,z position of attractive point */
  char CNGfname[STRLEN];              /* filename: attr. fact. w correction */
  double CNGAtractfactor;             /* attractive factor*/
  char RandomMusfilename[STRLEN];     /* filename: mu_s (hetro. medium cells) */
  int NumStacks;                      /* number of stacks */
  long AttemptsLimit;                 /* limit on number of attempts */
  int num_Mediums;                    /* number of Media. */
  MediumStruct * Mediumspecs;         /* medium parameters. */
} SysStruct;

/*************************************************************************/
/*** Main subroutine ***/

void Simulate(InputStruct * In_Ptr, SysStruct * Sys_Ptr)
{
  PhotonStruct Photon, Refl_Photon;
  PhotonPackageStruct PhotonPackage, SpecialPhotonPackage;
  BdryStruct Bdry;
  double TimeLimit=Sys_Ptr->TimeLimit,TimeToDetector,
    R_detector=Sys_Ptr->R_detector,
    xdet,ydet,zdet,xinit,yinit,zinit;
  double InitRefl= Specular_Refl(Sys_Ptr->Mediumspecs);
  register long i_photon,Attempts=0,AttemptsLimit=2000;
  double x=Photon.x,y=Photon.y,z=Photon.z;
  double x_dir=Photon.x_dir,y_dir=Photon.y_dir,z_dir=Photon.z_dir;
  double Lx=Sys_Ptr->Mediumspecs[1].x,
    Ly=Sys_Ptr->Mediumspecs[1].y,
    Lz=Sys_Ptr->Mediumspecs[1].z;
  int Stack,NumStacks;
  double r,xap,yap,zap,AllFlightDelay=0.,ThisFlightDelay=0.;
  double norms[361],*normsptr,RandomMus[2000],*RandomMusptr;
  FILE *outfile, *normsfile,*tmpfile,*RandomMusfile;
  double old_x,old_y,old_z,midx,midy,midz,midr,tmpf;
  int tmpi=0,i;

  NumStacks=Sys_Ptr->NumStacks;
```

```
/*Source coordinates*/
xinit=Lx/2.0+Sys_Ptr->P_source;
yinit=Ly/2.0;
zinit=0.0;
/*Detector coordinates*/
Sys_Ptr->xdet=xdet=xinit;
Sys_Ptr->ydet=ydet=yinit;
Sys_Ptr->zdet=zdet=Lz;
/*Attractive point coordinates*/
Sys_Ptr->xap=xap=xinit;
Sys_Ptr->yap=yap=yinit;
Sys_Ptr->zap=zap=Lz+R_detector;

normsfile=fopen(Sys_Ptr->CNGfname, "r");
for (i=0; i<361; i++) {
  norms[i]=0.0; fscanf(normsfile,"%lf", &norms[i]);
}fclose(normsfile); normsptr=norms;

RandomMusfile=fopen(Sys_Ptr->RandomMusfilename, "r");
for (i=0; i<2000; i++) {
  RandomMus[i]=0.0; fscanf(RandomMusfile,"%lf", &RandomMus[i]);
}fclose(RandomMusfile); RandomMusptr=RandomMus;

outfile= fopen(In_Ptr->out_fname, "w");
fclose(outfile);

InitRefl = Specular_Refl(Sys_Ptr->Mediumspecs);
InitRefl =0.0;

Photon.photonID=In_Ptr->num_photons;
do{   /*for all photons*/

  if (Photon.photonID==-1) goto AllDone;
  LaunchPhoton(InitRefl,Sys_Ptr->Mediumspecs,&Photon,Sys_Ptr,&PhotonPackage);

  tmpi=0;
  TimeLimit=(Sys_Ptr->TimeLimit !=0.0)*Sys_Ptr->TimeLimit;
  Attempts =0;
  AllFlightDelay=(Sys_Ptr->TimeLimit !=0.0)*Sys_Ptr->TimeLimit+
    (Sys_Ptr->TimeLimit == 0.0)*2.*Lz;
SamePhoton:
  if (NumStacks !=0) {
    PhotonPackage.PhotonPackageSpecs[0].WasHere=1;
    Attempts +=1;
  }
```

```
do{   /*for one photon*/
  old_x=Photon.x; old_y=Photon.y; old_z=Photon.z;
  Refl_Photon=Photon;
  Propagate(&Photon,&Refl_Photon,&Bdry,normsptr,RandomMusptr,Sys_Ptr);

  Photon.r=(r=sqrt((Photon.x-xinit)*(Photon.x-xinit)+
                   (Photon.y-yinit)*(Photon.y-yinit)));
  if (TimeLimit!=0.0){
    if (r < R_detector)
      Photon.TimeToDetector=fabs(Lz-Photon.z);
    else if (r >= R_detector)
      Photon.TimeToDetector=
        sqrt((r-R_detector)*(r-R_detector)+
             fabs(Lz-Photon.z)*fabs(Lz-Photon.z));
    if ((Photon.FlightTime+Photon.TimeToDetector) > TimeLimit){
      Photon.slow=1; Photon.dead=1;
    }
  }

  if ((Photon.z >= Lz/2. && old_z < Lz/2.) ||
      (Photon.z <= Lz/2. && old_z > Lz/2.))
    {
      tmpf=(Lz/2.-old_z)/(Photon.s*Photon.z_dir);
      midx=old_x+Photon.s*tmpf*Photon.x_dir;
      midy=old_y+Photon.s*tmpf*Photon.y_dir;
      midz=Lz/2.;
      midr=sqrt((midx-xinit)*(midx-xinit)+(midy-yinit)*(midy-yinit));
      if (midr <  Photon.rmidmin) Photon.rmidmin=midr;
      if (midr >= Photon.rmidmax) Photon.rmidmax=midr;
    }

  if (r > Photon.rmax) {
    Photon.rmax=r;
    Photon.zmax=Photon.z;
  }

  Photon.ints +=1;
  if (NumStacks !=0){
    i=(Photon.z*NumStacks/(Lz) > PhotonPackage.PhotonPartPtr) ?
      Photon.z*NumStacks/(Lz) : PhotonPackage.PhotonPartPtr;
    if (PhotonPackage.PhotonPartPtr <i && !Photon.dead && !Photon.slow){
          ThisFlightDelay=(Photon.FlightTime+Photon.TimeToDetector-
          (PhotonPackage.PhotonPackageSpecs[PhotonPackage.PhotonPartPtr].
                                                    FlightTime+
          PhotonPackage.PhotonPackageSpecs[PhotonPackage.PhotonPartPtr].
```

```
                                                        TimeToDetector))/
            (i-PhotonPackage.PhotonPartPtr);
        if (ThisFlightDelay >= AllFlightDelay && Attempts < AttemptsLimit){
          Photon=
            PhotonPackage.PhotonPackageSpecs[PhotonPackage.PhotonPartPtr];
            goto SamePhoton;
        }
        else {
          PhotonPackage.PhotonPackageSpecs[i]=Photon;
          PhotonPackage.PhotonPackageSpecs[i].WasHere=1.;
          PhotonPackage.PhotonPackageSpecs[PhotonPackage.PhotonPartPtr].
                                              FlightDelay=ThisFlightDelay;
          PhotonPackage.PhotonPartPtr=i;
        }
      }
  }
  if (Photon.w < CRITICALWEIGHT) Photon.dead =1;
}while (!Photon.dead);

/*** DETECTION ***/
if ((r <= R_detector || R_detector==0.0)
    && Photon.slow==0
    && Photon.P_Medium ==0
    && Photon.z_dir > 0.0
    && Bdry.bdryNo==6
    )
  {
    outfile= fopen(In_Ptr->out_fname, "a");
    fprintf(outfile,"%5.3f%5.2e%d\n",Photon.FlightTime,Photon.w,Attempts);
    fclose(outfile);
    Photon.detected=1;
  }
else Photon=Refl_Photon;

if ((NumStacks !=0) && (Attempts < AttemptsLimit)){
  if (Photon.detected){
     SpecialPhotonPackage=PhotonPackage;
    TimeLimit=Photon.FlightTime;
    PhotonPackage.DelayingStack=0;
    AllFlightDelay=0.0;
    tmpi=PhotonPackage.PhotonPartPtr;
    for (i=PhotonPackage.DelayingStack; i<tmpi; i++){
      if (PhotonPackage.PhotonPackageSpecs[i].WasHere >0 &&
          PhotonPackage.PhotonPackageSpecs[i].FlightDelay >
          AllFlightDelay){
```

```
            AllFlightDelay=PhotonPackage.PhotonPackageSpecs[i].FlightDelay;
            PhotonPackage.PhotonPartPtr=(SpecialPhotonPackage.DelayingStack=i);
          }
        }
      }
      else if (Attempts > 1 ) {
        PhotonPackage=SpecialPhotonPackage;
        PhotonPackage.PhotonPartPtr=PhotonPackage.DelayingStack;
      }
      else goto Hopeless;
      Photon=PhotonPackage.PhotonPackageSpecs[PhotonPackage.PhotonPartPtr];
      for(i=PhotonPackage.PhotonPartPtr+1; i <= NumStacks; i++){
        PhotonPackage.PhotonPackageSpecs[i].WasHere=0.0;
        PhotonPackage.PhotonPackageSpecs[i].FlightDelay=0.0;
      }
      goto SamePhoton;
    }
  Hopeless:
    Attempts=0;
    free(PhotonPackage.PhotonPackageSpecs);
    --Photon.photonID;
  } while(Photon.photonID);
 AllDone:
  FreeData(Sys_Ptr);
  fclose(outfile);
}

/*************************************************************************/
/*** This routine specifies the initial parameters for a new photon ***/
void LaunchPhoton(double Specular_Refl,
                  MediumStruct  * Mediumspecs_Ptr,
                  PhotonStruct * Photon_Ptr,
                  SysStruct  * Sys_Ptr,
                  PhotonPackageStruct * PhotonPackage)
{
  double x=Photon_Ptr->x, y=Photon_Ptr->y, z=Photon_Ptr->z;
  double x_dir=Photon_Ptr->x_dir=0.0,
    y_dir=Photon_Ptr->y_dir=0.0,
    z_dir=Photon_Ptr->z_dir=1.0;
  double Lx=Sys_Ptr->Mediumspecs[1].x,
    Ly=Sys_Ptr->Mediumspecs[1].y,
    Lz=Sys_Ptr->Mediumspecs[1].z;
  double R_source=Sys_Ptr->R_source;
  double mua = Sys_Ptr->Mediumspecs[1].mua;
  double mus = Sys_Ptr->Mediumspecs[1].mus;
```

```
  Photon_Ptr->w= 1.0 - Specular_Refl;
  Photon_Ptr->xmax=0.0; Photon_Ptr->ymax=0.0; Photon_Ptr->zmax=0.0;
  Photon_Ptr->rmax=0.0; Photon_Ptr->rmidmin=Lx+Ly; Photon_Ptr->rmidmax=0.0;
  Photon_Ptr->Tumour_ints = 0;
  Photon_Ptr->Tumour_FT = 0.0;
  Photon_Ptr->slow=0; Photon_Ptr->dead=0; Photon_Ptr->detected=0;
  Photon_Ptr->P_Medium= 1; Photon_Ptr->F_Medium=0;
  Photon_Ptr->s=0.0;  Photon_Ptr->sleft=0.0;
  Photon_Ptr->FlightTime = 0.0;
  Photon_Ptr->r=0.;
  Photon_Ptr->TimeToAP = Lz;
  Photon_Ptr->TimeToDetector= Lz;
  Photon_Ptr->FlightDelay    =0.0;
  Photon_Ptr->ints=0;
  Photon_Ptr->WasHere  = 0.;
  Photon_Ptr->x=x=Photon_Ptr->xinit=(Lx/2.0);
  Photon_Ptr->y=y=Photon_Ptr->yinit=(Ly/2.0+Sys_Ptr->P_source);
  Photon_Ptr->zinit=z=Photon_Ptr->z=1./(mus+mua);
  Photon_Ptr->P_Medium=whichregion(Sys_Ptr,x,y,z);
  if (x>Lx || y>Ly || z>Lz || x<0.0 || y<0.0 || z<0.0)
    nrerror("Wrong beam position");
  InitPhotonPackage(Sys_Ptr,Photon_Ptr,&PhotonPackage->PhotonPackageSpecs,
                &PhotonPackage->PhotonPartPtr,&PhotonPackage->DelayingStack);
}

/*****************************************************************************/
/*** This routine initialises the stacks ***/
void InitPhotonPackage(SysStruct  * Sys_Ptr,
                       PhotonStruct * Photon_Ptr,
                       PhotonStruct ** PhotonPackageSpecs,
                       int * PhotonPartPtr,
                       int * DelayingStack)
{
  char msg[STRLEN];
  int i=0;
  double z = 0.0;        /* z coordinate of the current Medium. */
  int * PhotonPart;
  int NumStacks=Sys_Ptr->NumStacks;
     *PhotonPackageSpecs = (PhotonStruct *)
          malloc((unsigned) (NumStacks+1)*sizeof(PhotonStruct));
  if (!(*PhotonPackageSpecs))
  nrerror("allocation failure in InitPhotonPackage()");

  for(i=0; i<=NumStacks; i++){
    (*PhotonPackageSpecs)[i]=*Photon_Ptr;
```

```
    (*PhotonPackageSpecs)[i].part=i;
  }
  *PhotonPartPtr=Photon_Ptr->zinit*NumStacks/(Sys_Ptr->Mediumspecs[1].z);
  *DelayingStack=Photon_Ptr->zinit*NumStacks/(Sys_Ptr->Mediumspecs[1].z);
}

/*************************************************************************/
/*** This routine propagates the photon ***/
void Propagate(   PhotonStruct *  Photon_Ptr,
                  PhotonStruct *  Refl_Photon_Ptr,
                  BdryStruct   *  Bdry_Ptr,
                  double *norms,
                  double *RandomMus,
                  SysStruct * Sys_Ptr)
{
  int prnt=0;
  int i,j,k;
  double x_dir=Photon_Ptr->x_dir,
    y_dir=Photon_Ptr->y_dir,
    z_dir=Photon_Ptr->z_dir;
  double x=Photon_Ptr->x, y=Photon_Ptr->y, z=Photon_Ptr->z;
  double Lx=Sys_Ptr->Mediumspecs[1].x,
    Ly=Sys_Ptr->Mediumspecs[1].y,
    Lz=Sys_Ptr->Mediumspecs[1].z;
  int  ix,iz;

  DeterminDirection(Photon_Ptr,Sys_Ptr->Mediumspecs[Photon_Ptr->P_Medium].g,
                    norms,Sys_Ptr);
  DeterminStepsize(Photon_Ptr,Sys_Ptr,RandomMus);
  if (HitBoundary(Photon_Ptr,Sys_Ptr,Bdry_Ptr,RandomMus)) {
    CrossOrNot( Photon_Ptr, Sys_Ptr,Bdry_Ptr);
  }
  else {
    Bdry_Ptr->xBdry=0;Bdry_Ptr->zBdry=0;
  }
}
/*************************************************************************/
/*** This routine calculates the new direction using        ***/
/*** Chen & Bai's method and recalculates the photon weight ***/

void DeterminDirection(PhotonStruct * Photon_Ptr,
                       double g,
                       double *norms,
                       SysStruct * Sys_Ptr)
```

```
    /* dtap: distance to attractive point */
    /* DiffLength: distance withing which attractive point is not used */
    /* ox(,y,z)_dir: original x(,y,z) direction */
    /* x(,y,z)ap: x(,y,z) coordinates of the attractive factor */
    /* cost and sint: cosine and sine of the zenith angle */
    /* cosp: cosine of the azimuthal angle */
    /* theia and thefa: initial & final direction of attractive factor */

{
  int i,BdryAway=1;
  double cost, sint, cosp, sinp, psi;
  double DiffLength;
  double ox_dir=0.,oy_dir=0.,oz_dir=1.;
  double x_dir=(ox_dir=Photon_Ptr->x_dir), y_dir=(oy_dir=Photon_Ptr->y_dir),
    z_dir=(oz_dir=Photon_Ptr->z_dir);
  double x=Photon_Ptr->x, y=Photon_Ptr->y, z=Photon_Ptr->z;
  double Lx=Sys_Ptr->Mediumspecs[1].x, Ly=Sys_Ptr->Mediumspecs[1].y,
    Lz=Sys_Ptr->Mediumspecs[1].z;
  int  P_Medium=Photon_Ptr->P_Medium;
  double mua = Sys_Ptr->Mediumspecs[P_Medium].mua;
  double mus = Sys_Ptr->Mediumspecs[P_Medium].mus;
  double dtap,xap=Sys_Ptr->xap,yap=Sys_Ptr->yap,zap=Sys_Ptr->zap,
    AtractFactor=Sys_Ptr->CNGAtractfactor,Pe=1.,theia,thefa,cia,cfa;
  double rand_pe=0.0,tmp;

  /*Don't use attractive point within a DiffLength form the boundaries*/
  DiffLength=1.0/(mus*(1.0-g));
  if ((x > Lx-DiffLength) || (x < DiffLength) ||
      (y > Ly-DiffLength) || (y < DiffLength) ||
      (z > Lz-DiffLength) || (z < DiffLength)) BdryAway=0;
  Photon_Ptr->TimeToAP=(dtap=sqrt((zap-z)*(zap-z)+
                                  (xap-x)*(xap-x)+(yap-y)*(yap-y)));
  if (AtractFactor > 0 && BdryAway) {
    cia=((xap-x)*ox_dir+(yap-y)*oy_dir+(zap-z)*oz_dir)/dtap;
    theia=acos(cia);
  }
  do{
    tmp = (1.0-g*g)/(1.0-g+2.0*g*RandomNum());
    cost = (1.0+g*g - tmp*tmp)/(2.0*g); if (cost == -1.0) cost +=COS90D;
    sint = sqrt(1.0 - cost*cost);
    psi = 2.0*PI*RandomNum();
    cosp=cos(psi);
    if (psi< PI) sinp=sqrt(1.0 - cosp*cosp);
    else sinp=-sqrt(1.0 - cosp*cosp);
    if (fabs(oz_dir) > COSZERO){
```

```
      x_dir=sint*cosp; y_dir=sint*sinp; z_dir=cost*SIGN(oz_dir);
    }
    else{
      tmp=sqrt(1.0-oz_dir*oz_dir);
      x_dir =sint*(ox_dir*oz_dir*cosp-oy_dir*sinp)/tmp+ox_dir*cost;
      y_dir =sint*(oy_dir*oz_dir*cosp+ox_dir*sinp)/tmp+oy_dir*cost;
      z_dir =-sint*cosp*tmp+oz_dir*cost;
    }
    if (AtractFactor > 0 && BdryAway) {
      cfa=((xap-x)*x_dir+(yap-y)*y_dir+(zap-z)*z_dir)/dtap;
      Pe=(1.0+cfa)/2.;
      if (Pe < COS90D) Pe=COS90D;
      Pe=pow(Pe,AtractFactor);
      rand_pe=RandomNum();
    }
  }while(fabs(x_dir)>1.0||fabs(y_dir)>1.0||fabs(z_dir)>1.0 || rand_pe>Pe);
  Photon_Ptr->x_dir=x_dir; Photon_Ptr->y_dir=y_dir; Photon_Ptr->z_dir=z_dir;
  if (AtractFactor > 0 && BdryAway) {
    i=(2.0*theia*180./PI+0.5)/1;
    Photon_Ptr->w *=(*(norms+i))/Pe;
  }
}
/*************************************************************************/
```

Bibliography

[1] M. Cutler, "Transillumination as an aid in the diagnosis of breast lesions, with special reference to its value in case of bleeding nipples," Surg. Gynecol. Obstet. **48,** 721-729 (1929).

[2] F. F. Jöbsis, "Noninvasive infrared monitoring of cerebral and myocardial oxygen sufficiency and circulatory parameters," Science **198,** 1264-1267 (1977).

[3] F. M. Hall, J. M. Storella, D. Z. Silverstone and G. Wyshak, "Nonpalpable breast lesions: recommendations for biopsy based on suspicion of carcinoma at mammography," Radiology **167,** 353-358 (1988).

[4] L. W. Bassett and C. Kimme-smith, "Breast sonography," Am. J. Roentgenol **156,** 449-450 (1991).

[5] E. B. de Haller, "time-resolved transillumination and optical tomography," J. Biomed. Opt. **1,** 7-17 (1996).

[6] B. J. Tromberg, N. Shah, R. Lanning, A. Cerussi, J. Espinoza, T. Pham, L. Svaasand and J. Butler, "Non-Invasive In Vivo Characterization of Breast Tumours Using Photon Migration Spectroscopy," Neoplasia **2,** 26-40 (2000).

[7] K. Suzuki, Y. Yamashita, K. Ohta and B. Chance, "Quantitative measurement of optical parameters in normal breast using time-resolved spectroscopy: *in vivo* results of 30 Japanese women," J. Biom. Opt. **1,** 330-334 (1996).

[8] B. J. Tromberg, O. Coquoz, J. B. Fishkin, T. Pham, E. R. Anderson, J. Butler, M. Chan, J. D. Gross, V. Venugopalan and D. Pham, "Non-invasive measurements of

breast tissue optical properties using frequency-domain photon-migration," Phyl. Trans. R. Soc. Lond. B **352,** 661-668 (1997).

[9] H. Key, E. R. Davies, P. C. jackson and P. N. T. Wells, "Optical attenuation characteristics of breast tissue at visible and near-infrared wavelengths," Phys. Med. Biol. **36,** 579-590 (1991).

[10] F. J. Lamarsh, *Introduction to nuclear reactor theory,* (Addison-Wesley Reading: MA 1972).

[11] A. N. Yaroslavsky, I. V. Yaroslavsky, T. Goldbach and H. Schwarzmaier, "Influence of the scattering phase function approximation on the optical properties of blood determined from the integrating sphere measurements," J. Biomed. Opt. **4,** 47-53, (1999).

[12] A. Ishimaru, *Wave propagation and scattering in Random media,* (Academic Press: New York, 1978).

[13] R. Graaff, J. G. Aarnoudse, F. F. M. de Mul and H. W. Jentink, "light propagation parameters for anisotropically scattering media based on a rigorous solution of the transport equation," Appl. Opt. **28,** 2273-2279 (1989).

[14] E. P. Zege, A. P. Ivanov and I. L. Katsev, *Image transfer through a scattering medium,* (Springer-Verlag: Berlin, 1991).

[15] V. Ntziachristosa and B. Chance, "Accuracy limits in the determination of absolute optical properties using time-resolved NIR spectroscopy," Med. Phys. **28,** 1115-1124 (2001).

[16] J. F. Beek, P. Blockland, P. Posthumus, M. Aalders, J. W. Pickering, H. J. C. M. Serenborg and M. J. C. van Germert, "*In vitro* double-integrating-sphere optical properties of tissues between 630 and 1064 nm," Phys. Med. Biol. **42,** 2255-2261 (1997).

[17] G. Zaccanti, F. Martelli and S. Del Bianco, "Method to measure the optical properties of small volumes of diffusive media," Appl. Opt. **41,** 7317-7324 (2002).

[18] R. A. J. Groenhuis, H. A. Ferwerda and J. J. Ten Bosh, "Scattering and absorption of turbid materials determined from reflection measurements: 1. Theory," Appl. Opt. **22,** 2456-2461 (1983).

[19] D. Grosenick, H. Wabnitz, H. H. Rinneberg, Moesta K. T. and P. M. Schlag, "Development of a time-domain optical mammograph and first *in vivo* application," Appl. Opt. **38,** 2927-2943 (1999).

[20] C. R. Simpson, M. Kohl, M. Essenpreis and M. Cope, "Near-infrared optical properties of *ex vivo* human skin and subcutaneous tissue measured using the Monte Carlo inversion technique," Phys. Med. Biol. **43,** 2465-2478 (1998).

[21] R. J. Mourant, T. Fuselier, J. Boyer, T. M. Johnson and I. J. Bigio, "Predictions and measurements of scattering and absorption over broad wavelength range in tissue phantom," Appl. Opt. **36,** 949-957, (1997).

[22] J. M. Schmitt and G. Kumar, "Optical scattering properties of soft tissue: a discrete particle model," Appl. Opt. **37,** 2788-2797 (1998).

[23] S. Ertefai and A. E. Profio, "Spectral transmittance and contrast in breast diaphanography," Med. Phys. **12,** 393-400 (1985).

[24] C. Wai-Fung, S. A. Prahl and A. J. Welch, "A review of the optical properties of biological tissue," IEEE J. Quant. Elec. **26**, 2166-2185 (1990).

[25] T. L. Troy, D. L. Page and E. M. Sevick-Muraca, "Optical properties of normal and diseased breast tissues: prognosis for optical mammography," J. Biomed. Opt. **1,** 342-355, (1996).

[26] S. L. Jacques, C. A. Alter and S. A. Prahl, "Angular dependence of HeNe laser light scattering by human dermis," Laser Life Sci. **1,** 309-333 (1987).

[27] V. G. Peters, D. R. Wyman, M. S. Patterson and G. L. Frank, "Optical properties of normal and diseased human breast tissues in the visible and near infrared," Phys. Med. Biol. **35,** 1317-1334 (1990).

[28] G. Zacharakis, A. Zolindaki, V. Sakkalis, G. Filippids, T. G. Papazoglou, D. D. Tsiftsis and E. Koumantakis, "*In vitro* optical characterization and discrimination of female breast tissue during hear infrared femtosecond laser pulses propagation," J. Biom. Opt. **6,** 446-449 (2001).

[29] R. Splinter, *Future directions laser in surg. Med. Eng. Fundat.* Poster Presentation (1989).

[30] H. J. C. M. Sterenborg, M. J. C. van Gemert, W. Kamphorst, J. G. Wolberst and W. Hogelvorst, "The spectral dependence of the optical properties of the human brain," Lasers Med. Sci. **4** 221-227 (1989).

[31] L. O. Reynolds, C. C. Johnson and A. Ishimaru, "Diffuse reflectance from a finite blood medium: applications to the modeling of fiber optic catheters," Appl. Opt. **15,** 2059-2067 (1976).

[32] S. T. Flock, B. C. Wilson and M. S. Patterson, "Total attenuation coefficient and scattering phase function of tissues and phantom material at 633 nm," Med. Phys. **14,** 835-841 (1987).

[33] G. Yoon, "Absorption and scattering of laser light in biological media-Mathematical modeling and methods for determining optical properties," Ph.D. dissertation, Univ. Texas at Austin (1988).

[34] T. L. Troy and S. N. Thennadil, " Optical properties of human skin in the near infrared wavelength range of 1000 to 2200nm," J. Biomed. Opt. **6,** 167-176 (2000).

[35] C. F. Bohren and D. R. Hoffman, *absorption and scattering of light by small particles,* (Wiley: New York 1983).

[36] J. T. Bruulsema, J. E. Hayward, T. J. Farrell, M. S. Patterson, L. Heinemann, M. Berger, J. Sandahl-Christiansen, H. Orskov, M. Essenpries, Schmelzeisen-Redeker and D. Böcker, "Correlation between blood glucose concentration in diabetics and noninvasively measured tissue optical scattering coefficient," Opt. Lett. **22,** 190-192, (1997).

[37] A. Torricelli, A. Pifferi, P. Taroni, E. Giambattistelli and R. Cubeddu, "*In vivo* optical characterization of human tissue from 610 to 1010 nm by time-resolved reflectance spectroscopy," Phys. Med. Biol. **46,** 2227-2237 (2001).

[38] A. H. Bennet, H. Osterburg, H. Jupintz and O. Richards, *Phase miscroscopy,* (Wiley: New York 1951).

[39] F. P. Bolin, L. E. Preuss, R. C. Taylor and R. J. Ference, "Refractive index of some mammalian tissues using a fiber optic cladding method," Appl. Opt. **28,** 2297-2303 (1989).

[40] R. C. West *ed.*, *CRC Handbook of Chemistry and Physics,* pp. D-221, (CRC Press: Boca Rota, Fla., 1984).

[41] B. Chance, S. Nioka, J. Kent, K. McCully, M. Fountain, R. Greenfeld and G. Holtom, "Time-resolved spectroscopy of haemoglobin and myoglobin in resting and ischemic muscle," Anal. Biochem. **174,** 698-707 (1988).

[42] G. D. Pedersen, N. J. McCormick and L. O. Reynolds, "Transport calculations for light scattering in blood," Biophy. J. **16,** 199-207 (1976).

[43] R. Chandrasekhar, *Radiation transfer,* (Oxford: Clarendon 1950).

[44] J. J. Duderstadt and W. R. Martin, *Transport Theory,* (John Wiley & Sons: New York 1979).

[45] S. R. Arridge and J. C. Hebden, "Optical imaging in medicine: II. Modelling and reconstruction," Phys. Med. Biol. **42**, 841-853 (1997).

[46] H. W. Lweis, "Multiple scattering in an infinite medium," Phys. Rev. **78,** 526-529 (1950).

[47] H. Bremmer, "Random volume scattering," Radiat. Sci. J. Res. **680,** 967-981 (1964).

[48] W. Cai, M. Lax and R. R. Alfano, "Cumulant solution of the elastic Boltzmann transport equation in an infinite uniform medium," Phys. Rev. E **61,** 3871-3876 (2000).

[49] W. Cai, M. Lax and R. R. Alfano, "Analytical solution of the elastic Boltzmann transport equation in an infinite uniform medium using cumulant expansion," J. Phys. Chem. B **104,** 3996-4000 (2000).

[50] S. R. Arridge, M. Cope and D. T. Delpy, "The theoretical basis for the determination of optical pathlengths in tissue: temporal and frequency analysis," Phys. Med. Biol. **37,** 1531-1560 (1992).

[51] J. A. Moon, R. Mahon, M. D. Duncan and J. Reintjes, "Resolution limits for imaging through turbid media with diffuse light," Opt. Lett. **18,** 1591-1593, (1993).

[52] A. Joblin, "Method of calculating the image resolution of a near-infrared time-of-flight tissue imaging system". Appl. Opt. **35,** 752-757 (1996).

[53] J. M. Kaltenbach and M. Kaschke, "Frequency and time-domain modelling of light transport in random media," Medical optical tomography: Functional imaging and Monitoring ed G Muller (Bellingham, WA: SPIE) 65-86 (1993).

[54] J. J. Duderstadt and L. J. Hamilton, *Nuclear reactor analysis,* (Wiley: New York 1976).

[55] M. S. Patterson, B. Chance and B. C. Wilson, "Time resolved reflectance and transmittance for the non-invasive measurement of tissue optical properties," Appl. Opt. **28,** 2331-2336 (1989).

[56] G. Eason, A. Vetich, R. Nisbet and F. Turnbull, "The theory of the backscattering of light by blood," J. Phys. D **11,** 1463-1479 (1978).

[57] P. N. den Outer, T. M. Nieuwenhuizen and A. Langendijk, "Location of objects in multiple-scattering media," J. Opt. Soc. Am. A **10,** 1209-1218 (1993).

[58] D. A. Boas, M. A. O'Leary, B. Chance and A. G. Yodh, "Detection and characterization of optical inhomogeneities with diffuse photon density waves: a signal-to-noise analysis," Appl. Opt. **36,** 75-92 (1997).

[59] S. Feng, F. A. Zeng and B. Chance, "Photon migration in the presence of a single detect: a perturbation analysis," Appl. Opt. **34,** 3826-3837 (1995).

[60] K. Furutsu and Y. Yamada, "Diffusion approximation for a dissipative random medium and the applications," Phys. Rev. E **50,** 3634-3640 (1994).

[61] Y. Tsuchiya, K. Ohta and T. Urakami, "Isotropic photon injection for noninvasive tissue spectroscopy," Jpn. J. Appl. Phys. **34,** 2495-2501 (1995).

[62] K. M. Yoo, F. Liu and R. R. Alfano, "When does the diffusion approximation fail to describe photon transport in random media?" Phys. Rev. Lett. **64,** 2647-2650 (1990).

[63] W. Hackbush, *Multigrid methods and applications,* (Springer: Berlin 1980).

[64] B. W. Pogue, M. S. Patterson, H. Jiang and K. D. Paulsen, "Initial assessment of a simple system for frequency domain diffuse optical tomography," Phys. Med. Biol. **40,** 1709-1729 (1995).

[65] W. F. Ames, *Numerical methods for partial differential equations,* 2nd ed. (Academic Press: New York 1977).

[66] F. Natterer, *The mathematics of computerized tomography,* (Wiley-Teunbner: Stattgart 1986).

[67] W. Sun, N. G. Loeb and Q. Fu, "Finite-Difference time-domain solution of light scattering and absorption by particles in an absorbing media," Appl. Opt. **41,** 5728-5743 (2002).

[68] M. Schweinger, S. R. Arridge, M. Hiraoka and D. T. Delpy, "The finite element method for the propagation of light in scattering media: boundary and source conditions" Med. Phys. **22,** 1779-1792 (1995).

[69] C. R. E. de Oliveira, "An arbitrary geometry finite element for multigroup neutron transport with anisotropic scattering," Prog. Nucl. Energy **18,** 227-236 (1986).

[70] M. Schweinger, S. R. Arridge, M. Hiraoka, M. Fibank and D. T. Delpy, "Comparison of a finite element forward model with experimental phantom results: application to image reconstruction" Proc. SPIE **1888,** 179-190 (1993).

[71] S. R. Arridge, "Photon measurement density functions part I: Analytical forms," Appl. Opt. **34,** 7395-7409 (1995).

[72] L. Wang and S. L. Jacques, "Monte Carlo Modeling of Light Transport in Multilayer Tissues in Standard C," Optical Imaging Laboratory, Texas A&M Univ. (1998).

[73] I. M. Sobol, "A primer for the monte Carlo method" (CRC Press: Boca Raton 1994).

[74] N. G. Chen and J. Bai, "Estimation of quasi-straightforward propagating light in tissues," Phys. Med. Biol. **44**, 1669-1676 (1999).

[75] E. Tinet, S. Avrillier and J. M. Tualle, "Fast semianalytical Monte Carlo Simulation for time-resolve light propagation in turbid media," J. Opt. Soc. Am. A. **13,** 1903-1915 (1996).

[76] R. Graaff, M. H. Koelink, F. F. M. de Mul, W. G. Zijlstra, A. C. M. Dassel and J. G. Aarnoudse, "Condensed Monte Carlo simulations for the description of light transport," Appl. Opt. **32,** 426-434 (1993).

[77] R. F. Bonner, R. Nossal, S. Havlin and G. H. Weiss, "Model for photon migration in turbid biological media," J. Opt. Soc. Am. A **4,** 423-432 (1987).

[78] A. H. Gandjbakhche, G. H. Weiss, F. Bonner and R. Nossal, "Photon path-length distribution for transmission through optically turbid slabs," Phys. Rev. E **48,** 810-818 (1993).

[79] A. H. Gandjbakhche, R. Nossal and F. Bonner, "Resolution limits for optical transillumination of abnormalities deeply embedded in tissue," Med. Phys. **21,** 185-191 (1994).

[80] R. P. Feynman and A. R. Hibbs, *Quantum Mechanics and Path Integrals,* (McGraw-Hill: New Yord 1965.)

[81] L. T. Perelman, J. Winn, J. Wu, R. R. Dasari and M. S. Fled, "Photon migration of near-diffusive photons in turbid media: a Lagrangian-based approach," J. Opt. Soc. Am., A **14,** 224-229 (1997).

[82] J. N. Winn, L. T. Perelman, K. Chen, J. Wu, R. R. Dasari and S. M. Feld, "Distribution of the paths of early arriving photons traversing a turbid medium," Appl. Opt. **37,** 8085-8091, (1998).

[83] F. A. Grünbaum and J. P. Zubelli, "Diffuse tomography: computational aspects of the isotropic case," Inverse Problems **8,** 421-433 (1992).

[84] S. K. Patch, "recursive recovery of Markov transition probabilities from boundary value data," Ph.D. thesis, Univ. of California at Berkeley (1994).

[85] J. C. Hebden, S. R. Arridge and D. T. Delpy, "Optical imaging in medicine: I. Experimental techniques," Phys. Med. Biol. **42,** 825-840 (1997).

[86] J. R. Lakowicz and K. Brendt, "Frequency domain measurements of photon migration in soft tissues," Chem. Phys. Lett. **166,** 246-252 (1990).

[87] F. A. Zeng, G. Zhang, F. Liu and R. R. Alfano, "Diffuse optical tomography based on a WKB approximation," J. Biomed. Opt. **2** 426-436 (1997).

[88] T. O. McBride, B. W. Pogue, S. Jiang, U. L. Österberg and K. D. Paulsen, "A parallel-detection frequency-domain near-infrared tomography system for haemoglobin imaging of the breast *in vivo*," Rev. Sci. Instrum. **72,** 1817-1824 (2001).

[89] D. G. Papaioannou, S. B. Colak and 't Hooft G W, "Resolution and sensitivity of optical imaging in highly scattering media" Proc. SPIE **2626,** (1995).

[90] J. Lee and E. M. Sevick-Muraca, "Fluorescence-enhanced absorption imaging using frequency-domain photon migration: tolerance to measurement error," J. Biomed. Opt. **6** 58-67 (2001).

[91] E. M. Sevick, B. Chance, J. Leigh, S. Nioka and M. Maris, "Quantification of time- and frequency-resolved optical spectra fro the determination of tissue oxygenation," Annal. Biochem. **195,** 330-351 (1991).

[92] B. W. Pogue, K. D. Paulsen, C. Abele and H. Kaufman, "Calibration of near-infrared frequency-domain tissue spectroscopy for absolute absorption coefficient quantitation in neonatal head-simulating phantoms," J. Biomed. Opt. **5** 185-193 (2000).

[93] B. Ebert, U. Sukowski, D. Grosenick, H. Wabnitz, K. T. Moesta, K. Licha, W. Semmler, P. M. Schlag and H. H. Rinneberg, "Near-infrared fluorescent dyes for enhanced contrast in optical mammography: phantom experiments," J. Biomed. Opt. **6,** 134-140 (2001).

[94] K. T. Moesta, S. Fantini, H. Jess, M. A. Franceschini and M. Kaschke, "Contrast features of breast cancer in frequency-domain laser scanning mammography," J. Biomed. Opt. **3,** 129-136 (1998).

[95] M. Fabiani, G. Gratton and P. M. Corballis,"Noninvasive near infrared optical imaging of human brain function with subsecond temporal resolution," J. Biomed. Opt. **1,** 387-398 (1996).

[96] L. Nicolaides and A. Mandelis, "Novel dental dynamic depth profilometric imaging using simultaneous frequency-domain infrared photothermal radiometry and laser luminescence," J. Biomed. Opt. **5,** 31-39 (2000).

[97] J. B. Fishkin and E. Gordon, "Propagation of photon-density waves in strongly scattering media containing an absorbing semi-infinite plane bounded by straight edge" J. Opt. Soc. Am. A **10,** 127-140 (1993).

[98] R. R. Alfano, "Semiconductors Probed by Ultrafast Laser Spectroscopy. Volume II," Academic Press, 1984.

[99] J. L. Martin, Y. Lecarpentier, A. Antonetti and G. Grillon, "Picosecond laser stereometry light scattering measurements of biological material," Med. Biol. Eng. Comput. **18,** 250-252 (1980).

[100] M. A. Duguay and A. T. Mattick, "Ultrahigh speed photography of picosecond light pulses and echoes," Appl. Opt. **10,** 2162-2170 (1971).

[101] X. Liang, L. Wang, P. P. Ho and R. R. Alfano, "Two-dimensional KerrFourier imaging of translucent phantoms in thick turbid media," Appl. Opt. **34,** 34633467 (1995).

[102] D. J. Hall, J. C. Hebden and D. T. Delpy, "Evaluation of spatial resolution as a function of thickness for time-resolved optical imaging of highly scattered media," Med. Phys. **24,** 361-368 (1997).

[103] D. T. Delpy, M. Cope, P. van der Zee, S. Arridge, S. wary and J. Wyatt, "Estimation of optical path length through tissue from direct time-of-flight measurements," Phys. Med. Biol. **33,** 1433-1442 (1988).

[104] G. Mitic, J. Kölzer, J. Otto, E. Plies, G. Sölkner and W. Zinth, "Time gated transillumination of biological tissues and tissue-like phantoms," Appl. Opt. **33,** 6699-6709 (1994).

[105] D. R. Kirkby and D. T. Delpy, "Measurement of tissue Temporal Point Spread Function (TPSF) by use of a cross-correlation technique with an avalanche photodiod detector," SPIE **2389,** 190-197, (1995).

[106] K. M. Yoo, Q. Xing and R. R. Alfano, "Imaging objects hidden in highly scattering media using femtosecond second-harmonic-generation cross-correlation time gating," Opt. Soc. Am. **16,** 1019-1021 (1991).

[107] E. B. de Haller, C. Depeursinge and C. Y. Genton, "Resolution of time-resolved breast transillumination: in *vitro* measurements compared with theoretical predictions," Opt. Eng. **34,** 2084-2090 (1995).

[108] J. Watson, P. Georges, T. Lepine, B. Alonzi and A. Brun, "Imaging in diffuse media with ultrafast degenerate optical parametric amplification," Opt. Lett. **20,** 231233 (1995).

[109] C. Yan and J. C. Diels, "Imaging with femtosecond pulses," Appl. Opt. **32,** 68696873 (1992).

[110] J. Reintjes, M. Bashkansky, M. D. Duncan, R. Mahon, L. L. Tankersley, J. A. Moon, C. L. Alder and J. M. S. Prewitt, "time-gated imaging with nonlinear optical Raman interactions," Opt. Phot. News **4,** 28-32 (1993).

[111] J. C. Hebden, F. M. Gonzalez, A. Gibson, E. M. C. Hillman, R. Md. Yusof, N. Everdell and D. T. Delpy, "Assessment of an in situ temporal calibration method for time-resolved optical tomography," J. Biomed. Opt. **8,** 87-92 (2003).

[112] H. Xu, H. Dehghani, B. W. Pogue, R. Springett, K. D. Paulsen, J. F. Dunn, "Near-infrared imaging in the small animal brain: optimization of fiber positions," J. Biomed. Opt. **8,** 102-110 (2003).

[113] S. Fantini, M. A. Franceschini, E. Gratton, D. Hueber, W. Rosenfeld, D. Maulik, P. G. Stubblefiled and M. R. Stankovic, "Non-invasive optical mapping of the piglet in real time," Opt. Express **4,** 308-314 (1999).

[114] V. Ntziachristosa, X. H. Ma and B. Chance, "Time-correlated single photon counting imager for simultaneous magnetic resonance and near-infrared mammography," Rev. Sci. Instrum., **69,** 4221-4233 (1998).

[115] H. Eda, I. Oda, Y. Ito, Y. Wada, Y. Oykawa, Y. Tsunazawa, M. Takada, Y. Tsuchiya, Y. Yamashita, M. Oda, A. Sassaroli, Y. Yamada, and M. Tamura, "Multichannel time-resolved optical tomographic imaging system," Rev.

[116] P. Bruscaglioni and G. Zaccanti, "Multiple scattering in dense media" in *scattering in volumes and surfaces,*, Eds: M. Nieto Vesperinas and J. C. Dainty, pp 53-71, (Elsevier: New York 1990).

[117] M. R. Hee, J. A. Izatt, J. M. Jacobson and J. G. Fujimoto, "Femtosecond transillumination optical coherence tomography," Opt. Lett. **18,** 950-952 (1993).

[118] J. C. Hebden and A. H. Gandjbakhche, "Experimental validation of an elementary formula for estimating spatial resolution of optical transillumination imaging," Med. Phys. **22,** 1271-1273 (1995).

[119] L. H. Sim and K. N. Nitschke, "Testing random number generators for Monte Carlo applications," Aust. Phys. & Eng. Soc. in Med. **16,** 22-32 (1993).

[120] G. Marsaglia and A. Zaman, "Some portable very-long-period random number generators," Computers in Physics **8,** 117-121 (1994).

[121] I. Vattulainen, T. Ala-Nissila, and K. Kankaala, "Physcal models as tests of randomness," Phys. Rev. E **52,** 3205-3214 (1995).

[122] J. C. Hebden, D. J. Hall and D. T. Delpy, "The spatial resolution performance of a time-resolved optical imaging system using temporal extrapolation," Med. Phys. **22,** 201-208 (1995).

[123] J. C. Hebden, "Evaluating the spatial resolution performance of a time-resolved optical imaging system," Med. Phys. **19,** 1081-1087 (1992).

[124] J. C. Dainty and R. Shaw, *Image Science,* (Academic Press: London 1974.)

[125] T. S. Curry, J. E. Dowdey and R. C. Murry, *Christensen's Physic of Diagnostic Radiology,* 4th ed. (Lea and Febiger: Philadelphia 1990).

[126] Bentzen S. M., "Evaluation of spatial resolution of a CT scanner by direct analysis of the edge response function," Med. Phys. **10,** 579-581 (1983).

[127] J. C. Hebden and R. A. Kruger, "Transillumination imaging performance: spatial resolution simulation studies," Med. Phys. **17,** 41-47 (1990).

[128] M. D. Duncan, R. Mahon, L. L. Tankersley and J. Reintjes, "Time-gated imaging through scattering media using stimulated Raman amplification," Opt. Lett. **16,** 1868-1870 (1991).

[129] V. Chernomordik, R. Nossal and A. H. Gandjbakhche, "Point spread function of photons in time-resolved transillumination experiments using simple scaling arguments," Med. Phys. **23,** 1857-1861 (1996).

[130] D. Contini, F. Marteli and G. Zaccanti, "Photon migration through a turbid slab described by a model based on diffusion approximation: I. Theory," Appl. Opt. **36,** 4587-4599 (1997).

[131] *Interactive Data Language (IDL): Reference Guide,* version 4, (Research Systems Inc.: 1995).

[132] V. Chernomordik, A. Gandjbakhche, M. Lepore, R. Esposito and I. Delfino, "Depth dependence of the analytical expression for the width of the point spread function (spatial resolution) in time-resolved transillumination," J. Biom. Opt. **6,** 441-445 (2001).

[133] A. Joblin, "Resolution and contrast of time domain transillumination breast imaging system," PhD thesis, Queensland University of Technology (1998).

[134] G. R. Grimmett and D. R. Stirzaker, *Probability and random processes,* (Oxford University Press: New York 1992.)

[135] A. M. Arthurs, *Probability theory,* (Routledge & Kegan Paul Ltd: London 1974).

[136] AS/NZS 2211.1:1997. Australian/New Zealand Standards, Laser safety, Part 1': Equipment classification, requirements and user's guide (1997).

[137] Christopher Chatfield, *Statistics for technology, A course in Applied statistics,* (Chapman and Hall: New York 1983).